Novel Methods for Estimating Above Ground Biomass

by

Xiao Dai

Bachelor of Science in Forestry, Nanjing Forestry University, 2018

A Thesis Submitted in Partial Fulfillment
of the Requirements for the Degree of

Master of Science in Forestry

in the Graduate Academic Unit of Faculty of Forestry and Environment Management

Supervisor: John A. Kershaw Jr., PhD, FOREM, University of New Brunswick

Examining Board: Mark Ducey, PhD, Adjunct FOREM, University of New Hampshire

Lloyd Waugh, PhD, Civil Engineering, University of New Brunswick

This thesis is accepted by the
Dean of Graduate Studies

THE UNIVERSITY OF NEW BRUNSWICK

February, 2021

ABSTRACT

Forest biomass is increasingly important for calibrating worldwide carbon changes and ensuring sustainable forest management. However, there are no consistent standards for aboveground biomass (AGB) estimation methods. Direct field estimation is costly and destructive. We explored alternative methods for estimating AGB based on different sources of ground-based remote sensing data. We compared allometric equations derived from metrics extracted from terrestrial laser scanning (TLS) to equations derived from metrics extracted from spherical images. Spherical image metrics consistently performed better than TLS metrics. Alternatively, we developed sector subsample selection methods that utilized only measurements from spherical photos with a smaller subsample of angle sample counts to correct for tree occlusion. The sector subsampling methods were comparable to widely used big BAF subsampling and were much more efficient for estimating AGB than the allometric equations. Sector subsampling has great potential to reduce costs for AGB estimation and enabling access to monetized carbon markets.

ACKNOWLEDGEMENTS

Many thanks to my supervisor Professor John A. Kershaw, who is very creative with new ideas and concepts and always gives me inspiration. He has been helping me all the journey since I came to Canada. My thesis could not finish without his patient and very kind guidance. I would like to thank Mark Ducey as a member of my committee, he provided many insightful comments and advice about sampling design. I would like to thank Jae Ogilvie as the other committee member for his professional technical skills and deep thoughts about spherical images. I would like to thank the summer field crew, Shawn Donovan and Michael Hutchinson, for their hard work in field data collection. I really appreciated Ting-Ru Yang as a member, a leader and a kind helper of our lab, who introduced Light Detection and Ranging scanning to me and gave me guidance and inspiration of my project and R data processing. Ting-Ru Yang and Yung-Han Hsu helped collect spherical images in NL as well as in NB with Yingbing Chen and Xu Ma. I am very grateful to Haozhou Wang for his photo BA software development. Finally, I would like to thank my parents and friends for their support. Support for this research and data from the spacing trials were provided by the Province of Newfoundland and Labrador. Additional support is from the New Brunswick Innovation Foundation and the Canadian Natural Sciences and Engineering Research Council.

Table of Contents

List of Tables

List of Figures

Chapter 1 General Introduction

1.1 Importance of Estimating Biomass

Biomass is important in understanding and tracking change in the global carbon cycle (Houghton 2005; Le Toan et al. 2011). Forest biomass, which is related to global climate change, carbon content and forest management, has been recognized as an important input to Earth system models (Herold et al. 2019) and is also an important component of a healthy sustainable environment (Bartuska 2006). Due to the increasing attention on mitigating climate change and growing monetized carbon markets (Brown 2002), quickly quantifying forest biomass is extremely important for forest and business management decision-making (Brown 1999; Pearson et al. 2007; Chen et al. 2019). Because estimating below ground biomass is difficult, most research has focused on above ground biomass (AGB, (Lu et al. 2016). And the aboveground biomass production validation should be consistent across the world (Duncanson et al. 2019).

Although field measurement of forest biomass provides the most accurate estimates (Lu et al. 2016), traditional biomass measurement in the field and post validation is costly, destructive, labor intensive and time-consuming. To estimate biomass, the destructive harvest is required to dry and weight all parts of individual tree biomass, then sum up the biomass for a single tree and expand the single tree biomass to plot, stand or strata level estimates, which wastes lot of money and time (Kershaw et al. 2016) . New approaches have been developed to estimate AGB more efficiently such as application of allometric equations, biomass expansion/conversion factors, models based on remote sensing data to estimate aboveground biomass (Wang et al. 2009; Lu et al. 2016; Yang et al. 2017).

Spherical images also showed potential to estimate forest attributes of interest (Wang 2019). Nowadays, variables based on forest inventory data such as DBH, height, LiDAR point clouds or volume data can be applied into allometric equations to establish models for biomass estimation (Somogyi et al. 2007), which is much more efficient than traditional biomass measurement.

1.2 Objectives of this Thesis

The overall objectives of this thesis were to develop new methods for estimating per unit area aboveground biomass using spherical photos and to compare these methods. Model-assisted estimation based of spherical photos and terrestrial LiDAR will be developed and compared with sample-assisted methods developed for implementation with spherical photos.

1.3 Structure of Thesis

This thesis is composed of an introductory chapter, 3 paper chapters and a conclusions chapter.

Chapter 2 “Comparison of Biomass Estimation using Spherical Images versus Terrestrial LiDAR Scanning in Atlantic Canada”, model-based biomass estimation methods were applied using two sources of ground-based remote sensing: terrestrial LiDAR and spherical images. The two methods were compared to determine which approach performed best. This was the first study to compare TLS and spherical-camera-based metrics and their ability to predict above ground biomass. The two sources of ground-based remote sensing were compared on the basis of how well different metrics extracted for the data sources

were able to predict above ground biomass in western Newfoundland Island. Authorship on this chapter was: Dai, Xiao; Yang, Ting-Ru; and Kershaw, John A.

Chapter 3 developed the concept of sector subsampling as an alternative subsample selection method to big BAF subsampling. The subsampling methods selected measure-trees for biomass estimation and the estimation of the biomass to basal area ratio (BBAR). This chapter is the first study to apply sector sampling as a subsampling protocol similar to big BAF sampling. Two different methods of sector tree selection are compared to big BAF sampling. Both mean and standard errors of BBAR and biomass per ha are compared. This chapter has been submitted to the Canadian Journal of Forest Research and the authors were: Dai, Xiao; Ducey, Mark; Kershaw, John; and Wang, Haozhou.

In Chapter 4 we applied sector subsampling to spherical image analysis for biomass estimation. We showed that sector sampling can be effectively applied using spherical images even though only visible portions of the sectors were measurable. Errors were comparable to those obtained in Chapter 2 with only a fraction of the measure-trees selected. A hierarchical sampling design was developed to correct for tree occlusion and Bruce's formula was generalized for more the two means and their associated errors. The methods developed in this chapter do require any field measurements of trees, since all tree measurements can be obtained directly from the spherical images. This chapter has been submitted to Forestry: An International Journal of Forest Research, and the authorship of this chapter was: Dai, Xiao; Ducey, Mark; Wang, Haozhou; Yang, Ting-Ru; Hsu, Yang-Han; and Kershaw, John A.

In Chapter 5, the methods presented in Chapters 2, 3, and 4 were compared in terms of levels of effort required to implement and costs of equipment and processing time. Suggestions for future developments and future research were made.

References

Bartuska, A. 2006. Why biomass is important: The role of the USDA forest service in managing and using biomass for energy and other uses. Research & Development, USDA Forest Service. 1–16 p.

Brown, S. 1999. Guidelines for inventorying and monitoring carbon offsets in forest-based projects. Winrock International for the World Bank. Arlington, VA, USA.

Brown, S. 2002. Measuring, monitoring, and verification of carbon benefits for forest–based projects Swingland, I.R., E.C. Bettelheim, J. Grace, G.T. Prance, and L.S. Saunders (eds.). Philosophical Transactions of the Royal Society of London. Series A: Mathematical, Physical and Engineering Sciences. 360(1797):1669–1683.

Chen, Y., T.-R. Yang, Y.-H. Hsu, J. A. Kershaw, and D. Prest. 2019. Application of big BAF sampling for estimating carbon on small woodlots. For. Ecosyst. 6(1):13.

Duncanson, L., J. Armston, M. Disney, V. Avitabile, N. Barbier, K. Calders, S. Carter, J. Chave, M. Herold, and T. W. Crowther. 2019. The importance of consistent global forest aboveground biomass product validation. Surveys in geophysics. 40(4):979–999.

Herold, M., S. Carter, V. Avitabile, A. B. Espejo, I. Jonckheere, R. Lucas, R. E. McRoberts, et al. 2019. The Role and Need for Space-Based Forest Biomass-

Related Measurements in Environmental Management and Policy. Surv Geophys. 40(4):757–778.

Houghton, R. A. 2005. Aboveground Forest Biomass and the Global Carbon Balance. Global Change Biol. 11(6):945–958.

Kershaw, J. A., M. J. Ducey, T. W. Beers, and Bertram. Husch. 2016. Forest mensuration. Fifth edition. John Wiley & Sons.

Le Toan, T., S. Quegan, M. W. J. Davidson, H. Balzter, P. Paillou, K. Papathanassiou, S. Plummer, et al. 2011. The BIOMASS mission: Mapping global forest biomass to better understand the terrestrial carbon cycle. Remote Sensing of Environment. 115(11):2850–2860.

Lu, D., Q. Chen, G. Wang, L. Liu, G. Li, and E. Moran. 2016. A survey of remote sensing-based aboveground biomass estimation methods in forest ecosystems. International Journal of Digital Earth. 9(1):63–105.

Pearson, T. R. H., S. L. Brown, and R. A. Birdsey. 2007. Measurement guidelines for the sequestration of forest carbon. U.S. Department of Agriculture, Forest Service, Northern Research Station, Newtown Square, PA. Available online at: https://www.fs.usda.gov/treesearch/pubs/13292; last accessed January 16, 2020.

Somogyi, Z., E. Cienciala, R. Mäkipää, P. Muukkonen, A. Lehtonen, and P. Weiss. 2007. Indirect methods of large-scale forest biomass estimation. Eur J Forest Res. 126(2):197–207.

Wang, G., T. Oyana, M. Zhang, S. Adu-Prah, S. Zeng, H. Lin, and J. Se. 2009. Mapping and spatial uncertainty analysis of forest vegetation carbon by combining national

forest inventory data and satellite images. Forest Ecology and Management. 258(7):1275–1283.

Wang, H. 2019. Estimating forest attributes from spherical images. MSc Forestry Thesis, University of New Brunswick, Fredericton, NB, Canada. Available online at: https://unbscholar.lib.unb.ca/islandora/object/unbscholar%3A10158.

Yang, T.-R., Y.-H. Hsu, J. A. Kershaw, E. McGarrigle, and Dan Kilham. 2017. Big BAF sampling in mixed species forest structures of northeastern North America: influence of count and measure BAF under cost constraints. Forestry: An International Journal of Forest Research. 90(5):649–660.

Chapter 2 Comparison of Biomass Estimation using Spherical Images versus Terrestrial LiDAR Scanning in Atlantic Canada

Abstract

Biomass is an important ecosystem measure. Measurement of biomass from destructive samples is labor intensive and difficult to update quickly. The use of allometric equations requires extensive field data, which is also expensive to acquire and equally difficult to update. Remote sensing is a means of estimating biomass quickly through model-assisted techniques. In this study, two terrestrial remote sensing sources, a terrestrial LiDAR scanner (TLS) and a 360° spherical camera, were evaluated based on model-assisted approaches. Several TLS metrics based on height quantiles and density measure were extracted from TLS scans. Photo basal area (PBA) was extracted from spherical photos at different heights above ground. Nonlinear regression models were developed using the different metrics from each remote sensing technique. Models based on TLS metrics explained between 3% and 23% of the variation in stand-level biomass, while models based on PBA explained 19% to 74% of the variation. In this study, 360° spherical camera consistently provided model estimates that had lower rMSE than the models developed from TLS. Averages of estimates of PBA from multiple sample locations within a sample plot or averages across multiple heights produced better models than PBA estimates from single sample locations within a plot. Stand structural diversity and species composition negatively impacted model prediction ability for both TLS and spherical images. Given the cost differences, field acquisitions times, and post-processing times, the estimates from a

360° spherical camera provide an accurate and affordable alternative method for rapidly estimating biomass in Atlantic Canada.

Introduction

Biomass at global, regional or local scales is an important ecosystem measure of the Earth's carbon cycle (Le Toan et al. 2011). Forest biomass, which is closely related to carbon content within the forest, is also an important component of a healthy sustainable environment (Bartuska 2006). Due to the increasing attention on mitigating climate change and growing monetized carbon markets (Brown 2002), quickly quantifying forest biomass is extremely important for forest and business management decision-making (Brown 1999; Pearson et al. 2007; Chen et al. 2019). Collecting inventory parameters (e.g., diameter at breast height, DBH; and height) and sufficient destructive samples across a range of tree sizes to develop allometric equations for biomass estimation is time-consuming, subject to measurement error, and difficult to implement across large areas (Lu 2006). Development of such allometric equations are usually limited to research projects rather than implemented in operational inventories (Kershaw et al. 2016). Even collecting the data necessary to use allometric equations is costly and requires careful planning to produce cost efficient, low error estimates (Husch 1980; Lynch 2017; Yang et al. 2017). Developing efficient approaches to estimate biomass using advanced methods is required to reduce field inventory costs.

Light Detection and Ranging (LiDAR), which can provide high-resolution three-dimensional (3D) point clouds, has emerged as one of the promising sources of remote sensing data to estimate area-based forest attributes (Næsset 2002; Bouvier et al. 2015), or

individual tree analyses (Belton et al. 2013; Greaves et al. 2015). Generally, there are two broad types of LiDAR: airborne LiDAR scanning (ALS); and terrestrial LiDAR scanning (TLS). ALS has been widely used to characterize forest structural attributes (e.g., canopy height profiles and some individual tree attributes); however, because of tree occlusion, difficulties in characterizing structural diversity and vertical distribution by vegetation component (e.g., foliage distributions, branch identification, crown transparency and size distribution) still exist (Hilker et al. 2012; White et al. 2016). In comparison, TLS has shown promise to enhance airborne LiDAR by providing high-resolution scans of forest structure from the ground up (Ducey and Astrup 2013; Astrup et al. 2014).

Various approaches of biomass estimation using LiDAR data have been proposed. One common approach is model generation by combining field measurements and LiDAR attributes to build predictive models for area-based biomass estimation (Kankare et al. 2013). A variety of LiDAR attributes are extracted from point clouds. These attributes generally fall into one of four categories: 1) height- or canopy-based; 2) horizontal density-based; 3) horizontal and vertical variability; and 4) individual tree segmentation (Ayrey et al. 2019). Although various estimation approaches are advocated, which approach is the most efficient for biomass estimation has not been systematically explored. With high equipment expense, long field scanning times, extensive point cloud processing. and problems associated with detecting canopy surfaces and occluded trees, the efficiency of area-based biomass estimation via TLS remains an unknown (Lin et al. 2018), especially in terms of operational inventory.

Using high-resolution panoramic photography is an alternate, cost-effective way to improve forest inventory efficiency (Dick et al. 2010; Lu et al. 2019) and perhaps biomass estimation. Hemispherical panoramas are obtained by taking a series of photographs with a normal camera and a specialized device to precisely move the camera through the 360°/180° space, then stitching the multiple photographs together. The resulting hemispherical panoramas have a 360° horizontal and 180° vertical field of view and can be used to estimate tree attributes (Dick et al. 2010; Fastie 2010; Perng et al. 2018; Lu et al. 2019). Several close-range terrestrial photogrammetric approaches are used to obtain forest inventory attributes from hemispherical panoramic photographs. For example, Lu et al. (2019) recently applied a pinhole camera model and showed the potential for estimating volume of individual trees. However, one disadvantage of their approach was that a target of known size and the horizontal distance between the camera and sample tree were required to scale DBH. In another approach, Perng et al. (2018) used stereoscopic techniques to triangulate trees, obtain photo scale, and subsequent tree measurements. These approaches are time-consuming and labor intensive to implement on each tree in the field.

An alternative approach is to use the hemispherical panoramas as photo-based basal area plots and apply horizontal point sampling (HPS) principles as originally proposed by DeCourt (1956), and later revived by Stewart (2004), Dick (2012), and Fastie (2010). For photo-based HPS, an angle gauge, defined in terms of photo pixels, is used to select tally trees. Basal area per unit area is then calculated from the number of tally trees without any tree measurements required in the field (Bitterlich 1984; Iles 2003; Kershaw et al. 2016).

Compared with traditional field work, using high-resolution panoramic photography saves time and costs (Fastie 2010; Perng et al. 2018). While there are several advantages to using hemispherical panoramas, they have limitations similar to TLS. For example, the specialized devices to precisely move the camera through the 360°/180° space are costly and bulky to carry through the woods; acquisition times in the field can be lengthy; the multiple images require special software to stitch the images together; stitching potentially leads to errors; the stitched photographs then have to be processed to obtain the required measurements; and the issue of occluded trees is still problematic. In many respects, both hemispherical panoramas and TLS are exchanging high field labor costs for high equipment costs and office labor costs associated with post-field processing.

Recently, introduced consumer-grade 360° spherical cameras have the potential to address several of the current shortcomings of both TLS and hemispherical panoramas. These new cameras use two fixed hemispherical lenses to obtain a full 360°/360° spherical photograph. The two hemispherical photos are stitched together using the onboard camera software and the camera is controlled by a smartphone. Image acquisitions takes seconds and multiple images per sample location are obtained very rapidly. Wang (2019) and Wang et al. (2020) demonstrated how these images are used as photo-based HPS plots and applied spherical stereography to obtain estimates of tree DBH and total height. Mulverhill et al. (2019) used spherical images and structure from motion to develop 3D point clouds from which tree measurements were then extracted. The low cost, quick acquisition time, and small, compact size make these spherical cameras a more attractive alternative to both TLS and hemispherical panoramas.

Building upon the work of Wang et al. (2019) and Wang (2020), we propose to compare area-based estimates of biomass based on TLS attributes to estimates based on attributes extracted from spherical photos. To evaluate the performance of the two tools under different degrees of forest structural complexity, data collected from western Newfoundland (lower forest structural complexity) and Noonan Research Forest (higher forest structural complexity) in central New Brunswick are used in this study. Advantages and disadvantages of the two approaches are discussed.

Materials and Methods

Study sites

Data from two different research projects were used in this study. The first set of data came from three early spacing trials in western Newfoundland, Canada (Figure 2. 1). The second data set came from the Noonan Research Forest located in central New Brunswick, Canada (Figure 2. 1).

Early Spacing Trials in western Newfoundland

In the early 1980s, the government of Newfoundland, in cooperation with the Canadian Forest Service, established a series of early spacing trials in balsam fir (*Abies balsamea* L.) and black spruce (*Picea mariana*, (Mill.) Britton, Sterns & Poggenb.) dominated stands across Newfoundland island (Donnelly et al. 1986). In this study, 3 balsam fir trials located in western Newfoundland (NL) were used: Pasadena, Cormack, and Roddickton (south to north in Figure 2. 1). The spacing trial plots were arranged using a randomized complete block design with 3 replicates per site. There were 5 spacing treatments: Control or no

spacing (S00), 1.2m spacing (S12), 1.8m spacing (S18), 2.4m spacing (S24) and 3.0m spacing (S30). Each treatment was applied to a 0.25 ha block (50m x 50m), and a circular permanent sample plot (PSP) was established near the center of each block. There was a total of 45 PSPs from the NL spacing trials used in this study.

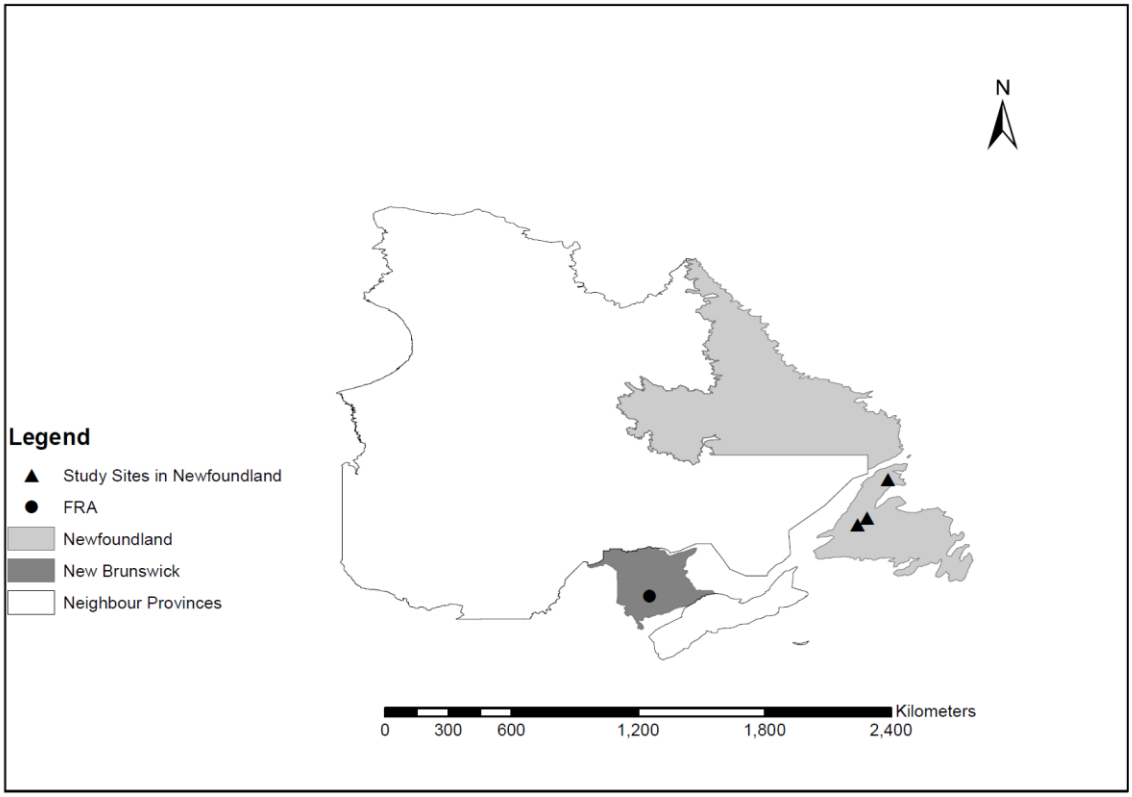

Figure 2. 1 Study site locations in Newfoundland and New Brunswick.

Because of the large differences in densities among the 5 treatments, the PSP radii varied by spacing treatment such that approximately 100 trees were measured on each PSP. The PSP radii by spacing treatment were: S00 = 5.2m; S12 = 7.2m; S18 = 10.4m; S24 = 15.0m; and S30 = 18.0m.

Trees taller than breast height (1.3m) were tagged with a unique tree number, identified by species, and diameter at breast height (DBH; nearest 0.1cm) and total height (HT; nearest 0.1m) were measured using a diameter tape and a telescoping height pole, respectively. Measurements were made immediately following spacing treatment and at intervals of 3 to 5 years with the last measurements being 2017 for Roddickton, 2013 for Pasadena, and 2013 for Cormack. A summary of field measurements is shown in Table 2. 1.

Noonan Research Forest (NRF)

The Permanent Sample Plots (PSPs) located on the Femelschlag Research Area within the Noonan Research Forest (NRF, Figure 2. 1) comprised the second data set used in this study. The Noonan Research Forest is managed by the University of New Brunswick's Faculty of Forestry and Environmental Management and is located approximately 30 km northeast of Fredericton, NB, Canada. The NRF is 1532 ha and the Femelschlag Research Area is approximately 80 ha.

Table 2. 1 Mean, standard deviation (in parentheses) and range (in bracket) for diameter at breast height (DBH, cm), total height (HT, m), stem density (Density, stems·ha-1), basal area (BA, m2ha-1), and biomass (tonnes·ha-1) by spacing treatments for the 45 Newfoundland (NL) spacing trials and overall for the 83 Noonan Research Forest (NRF) plots.

Study	Spacing	Parameter				
Site	Treatment	DBH (cm)	HT (m)	Density (stems·ha^{-1})	BA (m^{2}ha^{-1})	Biomass (tonnes·ha^{-1})
NL	Control	8.5 (1.51)	8.4 (1.34)	11000 (3400)	69 (7.8)	200 (19)
		{6.9, 11.1}	{6.2, 10.3}	{4800,16000}	{55, 83}	{170, 230}
	1.2m	11.9 (2.97)	9.4 (1.90)	5100 (1400)	58 (10.6)	180 (42)
		{8.5, 16.8}	{7.3, 12.4}	{3000,6800}	{44, 75}	{130, 250}
	1.8m	13.3 (2.09)	9.1 (1.54)	2900 (350)	43 (11.0)	130 (39)
		{9.9, 16.0}	{7.3, 11.3}	{2400, 3300}	{28, 63}	{80, 200}
	2.4m	16.2 (1.33)	10.1 (1.18)	1800 (450)	40 (9.6)	130 (32)
		{14.2, 18.7}	{8.1, 11.4}	{1300,2500}	{29, 59}	{90, 190}
	3.0m	17.7 (1.87)	10.0 (1.15)	1100 (150)	30 (7.0)	100 (25)
		{15.2, 20.3}	{8.7, 11.8}	{900,1300}	{21, 40}	{70, 140}
NRF	-	15.5 (3.10)	12.4 (1.76)	1900 (800)	41 (6.7)	180 (41)
		{9.7, 24.5}	{8.7, 17.4}	{600, 4450}	{21, 55}	{80, 310}

Species composition was typical of the Acadian Forest region (Loo and Ives, 2003; Rowe, 1972) with stand composition ranging from relatively pure conifer species to mixed intolerant hardwood stands and mixed hardwood–conifer stands. Balsam fir was abundant and found in almost every PSP. The NRF was predominantly composed of mature stands (>70 years old). Compared to the NL spacing trials, the PSPs from the NRF provided a dataset with more complex stand structures. Eighty-three 0.04 ha fixed area PSPs were established on a 100 m by 100 m sample grid for monitoring long-term response to silvicultural treatments. The PSPs were circular plots and all trees within 11.28m of plot center were tagged with unique tree numbers within each plot. All live trees ≥ 6.0 cm DBH were identified by species, and both DBH (nearest 0.1cm) and HT (nearest 0.1m) were measured in 2014. DBH was measured with a diameter tape and HT using a TruPulse laser hypsometer. A summary of observed field data for NRF is shown in Table 2. 1.

Biomass Estimation

The species-specific Canadian National Biomass equations developed by Lambert et al. (2005) were used to estimate individual tree biomass. The equations containing both DBH and HT (Eq. 3, Table 2. 4 in Lambert et al. 2005) were used in this study. The individual biomass components (wood, bark, branches, and foliage) were separately estimated, and total tree biomass was obtained by summing these components for each tree. Biomass per ha was obtained by multiplying each tree's biomass by its associated expansion factor (EF) and summing across all trees on each plot (Kershaw et al. 2016):

$$EF = \frac{10,000}{\text{plot size}(\text{m}^2)} \tag{1}$$

With the NL data, EF varied by spacing treatments, while it was fixed (i.e., EF = 25) for the NRF data. Field biomass estimates for both data sources are shown in Table 2. 1.

Terrestrial LiDAR Scanning and Processing

TLS scans were obtained using a Faro X330 phase-shift scanner (horizontal from 0° to 360° and vertical from 90° to -60°) with a shortwave infrared wavelength of 1550 nm. To balance the needs of scan quality and scan duration, 3 scans at 1/4 resolution (point spacing of 6.14 mm at a 10 m range) and 4X quality with the in-built GPS were completed for each scan (FARO Technologies Ltd, 2016). It required around 12 minutes per scan. Multiple scans on each plot were used to minimize tree occlusion. Scans were made at half the plot radius along azimuths of 120°, 240°, and 360°. TLS scans were obtained in August of 2017 in NL and in July of 2018 in the NRF.

The 3 scans obtained at each PSP were post-processed and stitched together using the FARO® SCENE software (FARO Technologies Ltd, 2016). The automatic matching algorithms often failed to produce an acceptable coregistered point cloud, so manual registration of scans using spherical reference targets placed within the PSPs was required. The filtering of individual point clouds to remove points outside the plot area was carried out after registration.

LiDAR Metrics

Area-based estimates built from LiDAR metrics using statistical techniques is a common method used for LiDAR analysis and was used in this study. Many studies show strong relationships between biomass and LiDAR metrics (Hilker et al. 2010; Greaves et al. 2015;

Palace et al. 2016). There are four major types of LiDAR metrics, including height-based metrics, density-based metrics, structure variability and individual tree segmentation. In this study, we focused on height-based metrics and point cloud densities at 4 different heights above ground (1.6m, 2.6m, 3.6m, 4.6m). These heights were chosen to correspond to the heights at which spherical image were obtained (Section 2.3). There were 12 metrics extracted from the LiDAR point clouds (Table 2. 2).

Spherical Image Acquisition and Processing

Spherical images were obtained using a Ricoh Theta S 360° camera (Ricoh Imaging Company, LTD 2016). For the PSPs in NL, spherical images were obtained at the same 3 locations used for TLS. However, in the NRF, spherical images were only obtained at the plot center (these images were originally obtained for a different analysis, thus the different protocols). At each spherical image acquisition location, spherical images were obtained at heights of 1.6m, 2.6m, 3.6m, and 4.6m using a tripod-stabilized height pole.

Table 2. 2 LiDAR metrics and associated descriptive statistics (mean ± stand deviation) for Newfoundland (NL) and the Noonan Research Forest (NRF).

Metric	Definition	Study Site	
		NL	NRF
MaxHT	Maximum height (m)	13.31 ± 2.98	23.25 ± 3.10
MeanHT	Mean height (m)	2.41 ± 0.52	2.82 ± 0.66
HTmaxDens	Height of the maximum density of LiDAR returns (m)	2.28 ± 1.01	1.89 ± 0.97
DensA16	Density of LiDAR returns (number per m³) above 1.6m height	0.35 ± 0.15	0.37 ± 0.07
DensA26	Density of LiDAR returns (number per m³) above 2.6m height	0.33 ± 0.15	0.35 ± 0.07
DensA36	Density of LiDAR returns (number per m³) above 3.6m height	0.29 ± 0.15	0.32 ± 0.08
DensA46	Density of LiDAR returns (number per m³) above 4.6m height	0.23 ± 0.15	0.29 ± 0.08
DensH16	Density of LiDAR returns (number per m³) at 1.6m ± 0.05m	0.35 ± 0.15	0.37 ± 0.07
DensH26	Density of LiDAR returns (number per m³) at 2.6m ± 0.05m	0.33 ± 0.15	0.35 ± 0.07
DensH36	Density of LiDAR returns (number per m³) at 3.6m ± 0.05m	0.29 ± 0.15	0.32 ± 0.08
DensH46	Density of LiDAR returns (number per m³) at 4.6m ± 0.05m	0.23 ± 0.15	0.29 ± 0.08
Kurtosis	Kurtosis of return heights	3.21 ± 0.83	6.04 ± 3.16

The primary variable extracted from the spherical images was photo basal area per unit area (PBA) at image height. For each spherical image, the PBA at the camera center was extracted using a custom software package (Pano2BA) developed by Wang (2019) and Wang et al. (2020). The Pano2BA software implements a photo-based HPS protocol (DeCourt 1956; Stewart 2004; Fastie 2010; Wang 2019). Spherical images were read into the software and displayed on the screen. With the use of the target marking option, a horizontal line was superimposed on the image at the vertical center. The target was scaled to represent a specified basal area factor (BAF). Then, the target was moved along the image center line and trees appearing larger than the target were marked using a mouse click. PBA was then the number of marked trees multiplied by the BAF.

As mentioned above, a common issue for any fixed ground-based remote sensing device is occluded trees. Occluded trees result in PBA underestimating field BA because trees that should be counted are missed because they are hidden by closer trees (Dick 2012; Wang et al. 2020). To minimize tree occlusion with the TLS scanner, we used multiple TLS scans and co-registration. Similarly, multiple PBA estimates and averaging was used to reduce the impact of occluded trees on the spherical images (Wang et al. 2020). Thus, there were 3 potential PBA variable combinations: 1) single PBA estimates at a single location and image height (PBA(S)); 2) averages of multiple PBA from different image locations, but single image heights (PBA(A)); and 3) averages of PBA across different image heights at either a single image sample point or multiple sample points (PBA(*)).

Table 2. 3 Photo metrics (photo basal area, PBA) and associated statistics (mean ± standard deviation) in Newfoundland (NL) and the Noonan Research Forest (NRF).

Metric	Definition[1]	Study Site	
		NL	NRF
PBA(S)1.6	PBA extracted from a single location (S) at1.6m above ground	35 ± 14.1	29 ± 7.8
PBA(S)2.6	PBA extracted from a single location (S) at 2.6m above ground	31 ± 13.4	27 ± 8.0
PBA(S)3.6	PBA extracted from a single location (S) at 3.6m above ground	27 ± 12.8	26 ± 7.4
PBA(S)4.6	PBA extracted from a single location (S) at 4.6m above ground	22 ± 11.4	24 ± 7.6
PBA(A)1.6	Average PBA extracted from 3 locations at 1.6m above ground	34 ± 12.3	-
PBA(A)2.6	Average PBA extracted from 3 locations at 2.6m above ground	31 ± 11.9	-
PBA(A)3.6	Average PBA extracted from 3 locations at 3.6m above ground	26 ± 11.4	-
PBA(A)4.6	Average PBA extracted from 3 locations at 4.6m above ground	21 ± 10.6	-
PBA(*)1.6,2.6	Average of PBA extracted from 1.6m and 2.6m above ground	32 ± 12.0	28 ± 7.6
PBA(*)1.6,3.6	Average of PBA extracted from 1.6m and 3.6m above ground	30 ± 11.7	28 ± 7.3
PBA(*)1.6,4.6	Average of PBA extracted from 1.6m and 4.6m above ground	28 ± 11.1	27 ± 7.3
PBA(*)1.6,2.6,3.6,4.6	Average of PBA extracted from all heights	28 ± 11.3	27 ± 7.2

[1]3 locations for NL center location for NRF

Biomass Estimation using TLS and PBA metrics

After exploring a number of linear and nonlinear functions, the power function proved to provide the best estimates of biomass for a majority of the TLS and PBA metrics. The single variable form of the power function was:

$$\widehat{\mathrm{BMASS}}_i = \mathrm{b}_0 X_i^{\,b_1} \tag{2}$$

where $\widehat{\mathrm{BMASS}}_i$ is the model estimated biomass in the ith PSP, X_i = a LiDAR (Table 2. 2) or photo (Table 2. 3) metric for the ith PSP, and b_j are nonlinear regression parameters. Models were evaluated based on root mean square error (rMSE) and the nonlinear pseudo-R^2:

$$\mathrm{rMSE} = \sqrt{\frac{\sum_{\mathrm{i}=1}^{\mathrm{n}}\left(BMASS_i\text{-}\widehat{\mathrm{BMASS}}_i\right)^2}{n}} \tag{3}$$

where BMASS_i = the field measured estimate of biomass in the ith PSP, $\widehat{\mathrm{BMASS}}_i$ is the model estimated biomass in the ith PSP, and n is the number of PSPs. To facilitate comparisons across spacing treatments and study locations, rMSEs were expressed as percentages of mean of field biomass (BMASS). The Kolmorgorov-Smirnov two-sample distribution test (K-S test; Zar 2009) was used to assess statistical differences between field and predicted biomass distributions. In addition, the two one-sided t-test for equivalence (TOST test, Robinson and Froese 2004) was used to compare predictions to field measures and predictions across models based on different LiDAR and photo metrics. The K-S tests were conducted using the ks.test() function in the base contributions (Arnold et al. 2013; R Development Core Team 2019) and the TOSTs were conducted using the tost() function from the equivalence package (Lakens 2017) in R.

Finally, we explore the impacts of stand structure on the resulting model errors. For the NL data, the best fitting TLS model and the best fitting PBA model (based on the lowest %rMSE) by spacing treatment were compared. For the NRF data, we calculated a basal area weighted Shannon's species diversity index (Staudhammer and LeMay 2001; McElhinny 2005) and Staudhammer and LeMay's (2001) diameter-height bivariate structural diversity index for each plot and then examined residuals from the best fitting TLS and PBA models graphically. All analyses were conducted in the R statistical language (R Development Core Team 2019).

Results

Models derived from TLS Metrics

Table 2. 4 shows %rMSEs and pseudo-R^2s for single variable power functions by LiDAR metrics and study sites. The ranges in %rMSE and pseudo-R^2 values for NL were larger than what were obtained for NRF across the different LiDAR metrics (Table 2. 4). The %rMSE of 12 TLS models ranged from 19.22 to 33.15 for NL, and 19.82 to 22.42 for NRF. While %rMSEs were generally smaller for NRF (less error) compared to NL, the pseudo-R^2s were also smaller (indicating less variation explained). For NL, density-based metrics generally performed better than height-based metrics (Table 2. 4). Metrics representing densities above specified heights (DensA##) performed better than density-based metrics at given height slices (DensH##; Table 2. 4). This was similar for the NRF; however, the differences were smaller. DensA46 was the best performing LiDAR metric for the NL data (best model was TLS07), while MeanHT was the best for the NRF data (best model was TLS02) with DensA46 just slightly larger (Table 2. 4). In no case did any

combination of multiple TLS metrics result in models with significant improvements in fit (results not shown). The estimated coefficients and their associated standard errors for all models on both study sites are shown in supplemental table S1.

Models derived from Spherical Images

For the NL data, %rMSEs were substantially smaller for biomass estimates derived from PBA (Table 2. 5) compared to those derived from LiDAR metrics (Table 2. 4). Likewise, the associated pseudo-R^2 values were much larger (Table 2. 5). For the NRF data, both the %rMSEs and pseudo-R^2 for the PBA models (Table 2. 5) were comparable to those obtained for the TLS models (Table 2. 4). As with the TLS models, all the pseudo-R^2 values for the PBA models in NRF were smaller than the ones in NL. The %rMSE of 12 PBA models ranged from 17.17 to 22.95 for NL, and 19.83 to 20.38 for NRF. The estimated coefficients and their associated standard errors for all PBA models for both study sites are shown in supplemental table S1.

Table 2. 4 Percent root mean square error (%rMSE) and nonlinear pseudo-R^2 for biomass estimation models built using individual LiDAR metrics for the Newfoundland (NL) and the Noonan Research Forest (NRF). Bold italic represents models that had no significant ($p > .05$) relationships.

Model Number	LiDAR Metric[1]	NL		NRF	
		%rMSE	Pseudo-R^2	%rMSE	Pseudo-R^2
TLS01	MaxHT	30.50	0.18	21.28	0.11
TLS02	MeanHT	***33.15***	***0.03***	19.82	0.23
TLS03	HTmaxDens	28.07	0.30	***22.20***	***0.03***
TLS04	DensA16	25.59	0.42	20.81	0.15
TLS05	DensA26	24.38	0.47	20.41	0.18
TLS06	DensA36	22.03	0.57	20.11	0.21
TLS07	DensA46	19.22	0.67	19.92	0.22
TLS08	DensH16	***32.95***	***0.04***	21.87	0.06
TLS09	DensH26	***32.78***	***0.05***	***21.92***	***0.06***
TLS10	DensH36	***32.81***	***0.05***	***22.33***	***0.02***
TLS11	DensH46	30.85	0.16	***22.42***	***0.01***
TLS12	Kurtosis	***32.83***	***0.05***	21.85	0.06

[1]see Table 2. 2 for definitions of each LiDAR metric

For the NL data, models derived from the averages of PBA from 3 photo sample locations performed better than models derived from PBA based on a single photo sample location (compare PBA(S)## to PBA(A)## in Table 2. 5). Averaging across multiple photo heights

was better than using a PBA estimate from a single height (compare PBA(*)## to PBA(S)## in Table 2. 5). For the NRF data, using a single average across different photo heights was statistically more significant than using each height as an independent variable, though the model improvements were small (compare PBA(*)## to PBA(S)## in Table 2. 5). However, it should be noted that for the NL data, PBA(*)## represents averages that are based on averages of three photo samples taken at each height, then averaged across different heights (i.e., averages of 6 or 12 PBAs), while for the NRF there was only 1 photo sample location with 4 different sample heights (i.e., averages of 2 or 4 PBAs). In no case did we find a model with multiple independent PBAs that resulted in significant ($p > .05$) improvements in fits (results not shown). For both NL and NRF data, the averages of PBAs at 1.6m and 4.6m produced the best fits to the biomass data (best model was PBA11).

Table 2. 5 Percent root mean square error (%rMSE) and nonlinear pseudo-R^2 for biomass estimation models built using various PBAs for Newfoundland spacing trials (NL) and Noonan Research Forest (NRF). (all equations were significant ($p \leq .05$))

Model Numbers	Photo Metric[1]	NL		NRF	
		%rMSE	Pseudo-R^2	%rMSE	Pseudo-R^2
PBA01	PBA(S)1.6	20.27	0.64	20.24	0.20
PBA02	PBA(S)2.6	20.96	0.61	20.11	0.21
PBA03	PBA(S)3.6	22.95	0.53	20.38	0.19
PBA04	PBA(S)4.6	21.69	0.58	20.01	0.21
PBA05	PBA(A)1.6	17.36	0.73	-	-
PBA06	PBA(A)2.6	18.34	0.70	-	-
PBA07	PBA(A)3.6	19.75	0.66	-	-
PBA08	PBA(A)4.6	19.62	0.66	-	-
PBA09	PBA(*)1.6,2.6	17.59	0.73	19.95	0.22
PBA10	PBA(*)1.6,3.6	17.88	0.72	20.07	0.21
PBA11	PBA(*)1.6,4.6	17.17	0.74	19.83	0.23
PBA12	PBA(*)1.6,2.6,3.6,4.6	17.83	0.72	19.84	0.23

[1] see Table 2. 3 for definitions of each photo metric

Model Comparisons

Figure 2. 2 shows the relationship between field biomass and the predicted biomasses from the best fitting TLS and PBA models for NL (TLS07 and PBA11) and NRF (TLS02 and PBA11). For both TLS and PBA models, NL predictions had a broader range and were

more closely related to field biomass than what was obtained for the NRF (Compare Figure 2. 2-A, C to Figure 2. 2-B, D). Across the range of field biomass, NL predictions had lower bias and less scatter about the 1:1 line (Figure 2. 2-A, C), while for the NRF there was substantial overprediction in the lower range of field biomass and substantial underprediction in the upper range (Figure 2. 2-B, D). Comparing the two sets of predictions (Figure 2. 2-E, F), again, the NL predictions appeared to be more similar than the NRF predictions; however, this was more a function of the range of predictions rather than actual differences (Figure 2. 2-E, F). In terms of statistical differences (K-S test) and statistical equivalences (TOST test), compared to the field biomass estimates, biomass predictions from the best models of TLS and PBA for both NL and NRF data were not significantly different and were statistically equivalent (based on a minimum detectable non-negligible difference of 10%) to the field measurements (Figure 2. 3). Similarly, the comparisons between the two predictions from the best models of TLS or PBA were not significantly different and were statistically equivalent for both NL and the NRF (Figure 2. 3).

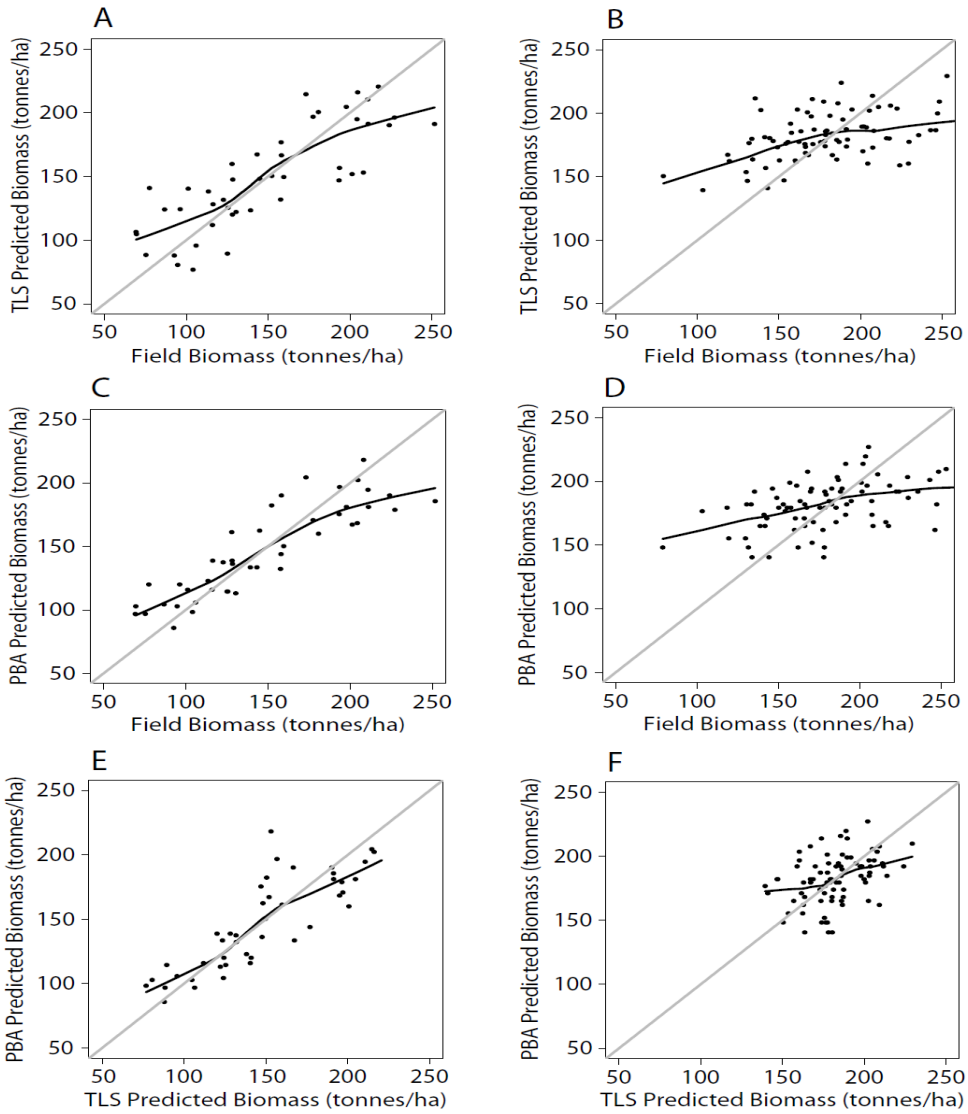

Figure 2. 2 Comparisons of best model predictions with field biomass and comparisons of best model predictions (PBA versus TLS metrics) for Newfoundland (NL) and Noonan Research Forest (NRF): A) Predictions from model TLS07 versus field biomass for NL; B) Predictions from model TLS02 versus field biomass for NRF; C) Predictions from model PBA11 versus field biomass for NL; D) Predictions from model PBA11 versus field biomass for NL; E) Predictions from model PBA11 versus TLS01 for NL; and F) Predictions from model PBA11 versus TLS02 for NRF.

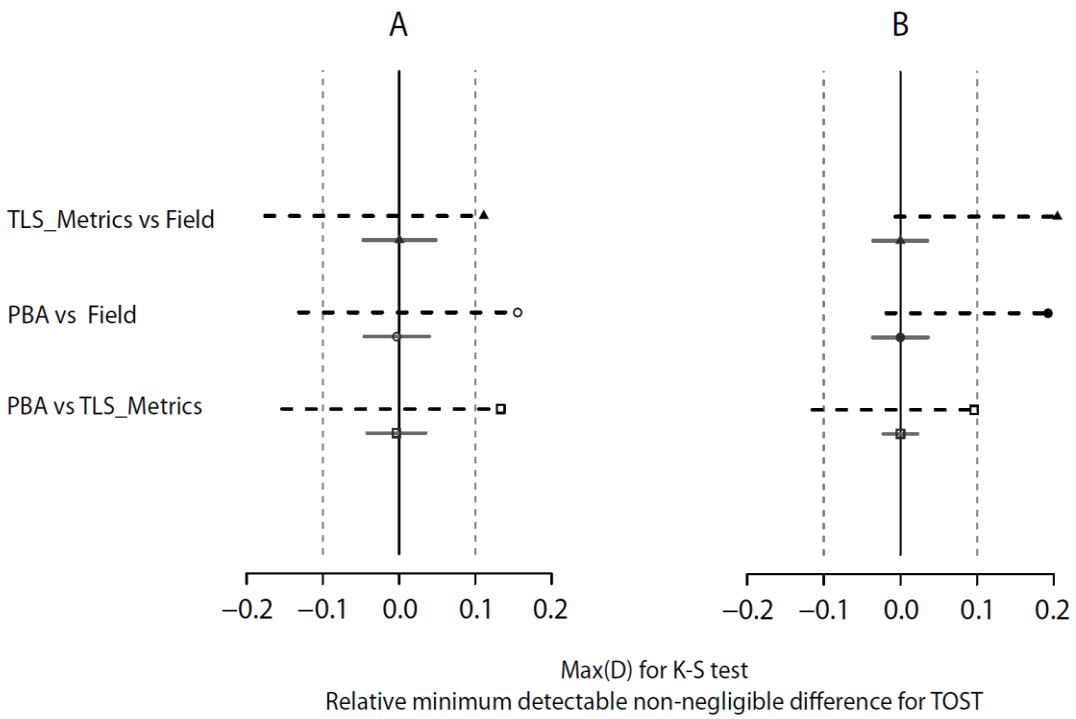

Figure 2. 3 Kolmogorov-Smirnov test (KS test, dashed lines) and Equivalence test (TOST test, solid lines) between best model predictions (models TLS02, TLS 07 and PBA11) and field biomass and between predictions for A) Newfoundland (NL) and B) Noonan Research Forest (NRF). (The horizontal bars for the KS test represent the critical ($\alpha = .05$) maximum difference and the horizontal bars for the TOST test represent the bounds of the zone of minimum detectable negligible differences of 10% of the mean value.)

Influence of Structural Diversity on Model Performance

Based on both the best TLS model and the best PBA model for the NL data, as management intensity increased (increasing spacing treatment), the %rMSE associated with each treatment (spacing) decreased (less error; Table 2. 6). Except for S00, %rMSEs for the best

PBA model were smaller than those for best TLS model across all spacing treatments (Table 2. 6). For both TLS and PBA models, biomass estimates for S00 were very poorly predicted and prediction error exceeded observed variation (Table 2. 6). For the NRF data, increasing species diversity did not result in any noticeable increase in bias for both the best TLS model and the best PBA model (Figure 2. 4-A, B) based on the lowess trend lines; however, both models showed a trend of increasing variability in residuals as species diversity increased. For the bivariate structural variance index (STVIdh) there was a slight trend of increasing negative bias with increasing structural diversity as well as increasing residual variation (Figure 2. 4-C, D).

Table 2. 6 Partial rMSEs (%) and nonlinear pseudo-R^2 under two biomass estimation models across five spacing treatments for Newfoundland (NL).

Spacing/m	TLS		PBA	
	%rMSE	Pseudo-R^2	%rMSE	Pseudo-R^2
0.0	15.46	---[1]	21.38	---[1]
1.2	23.02	0.32	19.67	0.51
1.8	20.92	0.37	16.88	0.59
2.4	18.83	0.24	11.22	0.73
3.0	14.25	0.29	12.38	0.46
Overall	19.82	0.67	17.17	0.74

[1] Model error exceeds variation

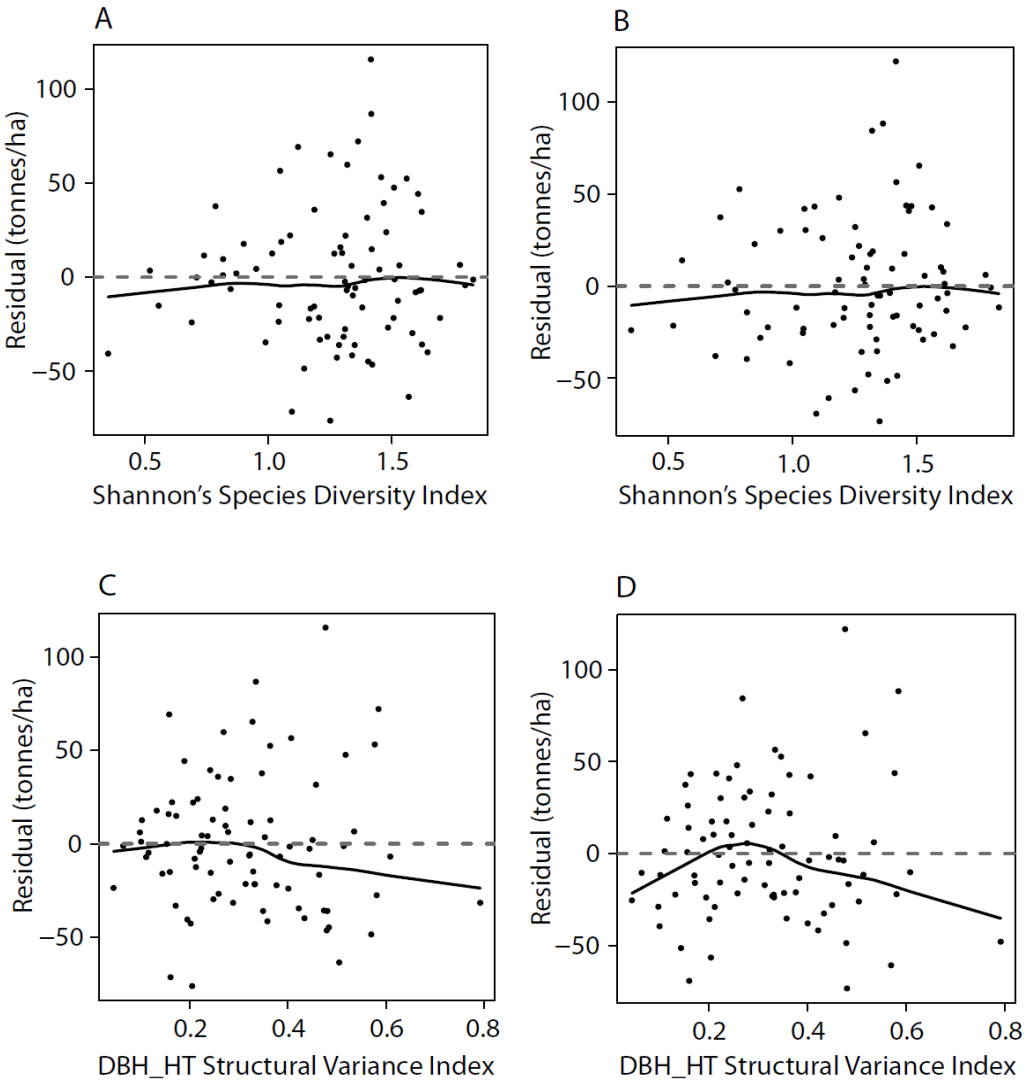

Figure 2. 4 Comparisons of residuals derived from TLS and PBA metrics with the bivariate structural variance index for Noonan Research Forest (NRF): A) Residuals from TLS02 model for NRF versus Shannon's index; B) Residuals from PBA11 model for NRF versus Shannon's index; C) Residuals from TLS02 model for NRF versus the index of structural diversity; and D) Residuals from PBA11 model for NRF versus the index of structural diversity.

Discussion

Forests represent a key component in the terrestrial carbon cycle (Le Toan et al. 2011; Pan et al. 2011; Jucker et al. 2017) and, as such, accurate inventory estimates are required to monitor and manage forest carbon stocks (Brown 1999, 2002). Biomass is an important precursor to the estimation of carbon stocks (Brown 1999, 2002; Chen et al. 2019). Therefore, efficient methods to estimate biomass are required (Bartuska 2006; Chen et al. 2019). One solution to this need is the development of biomass estimation models such as the ones developed in this project based on remote sensing.

In this study we compared biomass models derived from terrestrial LiDAR scans and spherical images obtained with a consumer-grade 360° spherical camera. Our errors associated with models derived from LiDAR metrics were generally larger than errors associated with models derived from spherical-image-derived PBA (Tables 2. 4 and 2. 5). The differences were greater for the NL data than for the NRF data. Percent rMSE (%rMSE) ranged from about 20% - 33% for the NL data and from 20% - 23% for NRF (Table 2. 4). Our errors were comparable to what others have found using TLS. For example, Clark et al.(2011) presented biomass models derived from height-based metrics in complex tropical forests with rMSEs of 38.3 Mg/ha. Moskal and Zheng (2011) found that single location TLS scans only explained about 18% of the variation in total sample tree volume. Astrup et al. (2014) reported errors of approximately 10% , Vaglio Laurin et al. (2014) reported errors of 39% with LiDAR height metrics, while Li et al. (2015) reported errors of 35% when estimating sagebrush biomass. Our best models developed from photo metrics explained over 50% of the variation in aboveground biomass in NL,

but only a little over 20% for the NRF (Table 2. 4). The use of a single photo-based sample location on the NRF may partially explain the lack of differences between TLS and PBA models as observed in the NL data with three photo sample locations.

Several studies have recently examined the use of hemispherical panoramas and spherical photography to extract stand and individual tree attributes (Stewart 2004; Dick et al. 2010; Berveglieri et al. 2017; Mulverhill et al. 2019; Wang et al. 2020). Stewart et al (2004), Dick et al. (2010), and Fastie (2010) all attempted to estimate basal area from single photos and/or panoramas stitched from multiple photographs based on the photo angle count concept originally proposed by DeCourt (1956). All of these studies identified tree occlusion as a major problem associated with photo-based angle count sampling. Wang et al. (2020) demonstrated that the photo angle count concept could be extended to spherical images and demonstrated that multiple photo sample points minimized the issue of occluded trees. Our results for estimating biomass support this conclusion as well. Using three sample points per plot reduced the %rMSE from about 20% to 17% for the NL spacing trail data (Table 2. 5). Using averages across multiple sample heights from multiple sample locations provided the best estimates but only marginally improved model performance (%rMSE was reduced from 17.36 to 17.17; Table 2. 5).

Stand structure significantly influenced model performance (Table 6, Figure 2. 4) and complex stand structure increased the difficulty in estimation of forest biomass (Table 6, Figure 2. 4). While increased species diversity did impact prediction bias, it did result in increasing variation in predictions errors (Figure 2. 4). Li et al. (2015) found that study-area size and point cloud density impacted model performance because differences in

sample sizes and spatial distributions can augment errors from allometric equations (Levia 2008). Zhao et al. (2012) also found that selection of allometric equations impacted the resulting LiDAR-based forest biomass estimates, especially in plots with high biomass. Substantial biases, in the form of underpredictions, are often present in the predictions for higher-density, higher-biomass stands (Li et al. 2019; Chen et al. 2020). Increasing stand complexity resulted in increased variance in residuals in this study (Figure 2. 4).

It is interesting to note that the best PBA models were the averages of PBA estimates at two different heights (Table 2. 4). Like biomass estimation is a precursor to carbon estimation (Brown 1999, 2002; Chen et al. 2019), volume can be considered a precursor to biomass estimation (Kershaw et al. 2016; Chen et al. 2019): Biomass = (Specific Gravity)(Volume). At the stem-level, volume of a stem section can be estimated using Smalian's formula (Kershaw et al. 2016 p. 141): Volume = 0.5(Area of Base + Area of Top)(Length). The areas are the cross-sectional areas estimated from the diameters at each end point. Cross-sectional area is a stem's equivalent to stand basal area. Our averages of PBA estimates at two different heights is really a stand-level expression of Smalian's formula. Coupling this estimate with some measure of stand height would most likely improve the models developed here. This is likely another contributing factor to the lack of improved model performance with the NRF versus NL data. The 4.6m sampling height is about 1/3rd the average plot height in NL, but only about 1/5th the average plot height on the NRF. The average PBA between 1.6m and 4.6m possibly better captures the basal area "taper" for the NL sites than it does for the NRF plots, thus producing models with substantially improved %rMSEs and pseudo-R^2s. The limits of our field equipment made

it impossible to obtain photos from higher points. A height pole with greater extension or mounting the spherical camera on a drone could easily solve this problem.

LiDAR scanning has gained recognition (White et al. 2013) as a standard tool in forest resource inventories (Reutebuch et al. 2005; Dassot et al. 2011). Wall-to-wall estimation of biomass is a common product from many airborne LiDAR-assisted forest inventory studies (Lefsky et al. 2002; Pflugmacher et al. 2008; Hawbaker et al. 2009; Meyer et al. 2013; Hayashi et al. 2015). The high spatial resolution of wall-to-wall LiDAR-assisted inventory maps makes LiDAR a seductive tool conveying a sense of accuracy that is not supported by the underlying models or field calibration data (Yang et al. 2019; Chen et al. 2020). Local calibration of LiDAR predictions may be required to make LiDAR-assisted predictions useful for local management decisions (Hsu 2019). The models developed here could be a useful approach to extend these plot-level estimates to wall-to-wall estimates using a hierarchical variable probability sampling design (Hsu 2019; Chen et al. 2020).

Conclusions

When we compare our TLS results to our PBA results, we find very little differences in model predictions (Figs. 2 and 3). PBA models generally account for a higher percentage of variation and produce lower %rMSEs than the TLS models. Given the field time differences and the cost differences, the spherical photos seem to be an effective way to estimate area-based above ground biomass relative to TLS. The Ricoh Theta S (Ricoh Imaging Company, LTD 2016) used in this study costs around $400 Canadian while the FARO Scanner costs over $100,000 Canadian. To obtain three mid-resolution scans per plot took upwards of one hour, while the 12 spherical photographs can be obtained in under

10 minutes. Multiple TLS scans must be postprocessed, including coregistering multiple scans, determining ground layers, and extraction of TLS metrics. This process can require up to 30 minutes of office processing time. The spherical photos also require post processing of images to obtain PBA estimates. Using the Pano2BA software (Wang et al. (2020)) requires about 2 minutes per photo. In this study we used up to 6 photos per plot for a total office time of approximately 12 minutes. Overall, we believe the spherical photo approach for estimating above ground biomass is more effective and efficient than TLS.

References

Arnold, T. B., J. W. Emerson, and R Core Team and contributors. 2013. Discrete Goodness-of-Fit Tests.

Astrup, R., M. J. Ducey, A. Granhus, T. Ritter, and N. von Lüpke. 2014. Approaches for estimating stand-level volume using terrestrial laser scanning in a single-scan mode. Can. J. For. Res. 44(6):666–676.

Ayrey, E., D. J. Hayes, S. Fraver, J. A. Kershaw, and A. R. Weiskittel. 2019. Ecologically-Based Metrics for Assessing Structure in Developing Area-Based, Enhanced Forest Inventories from LiDAR. Canadian Journal of Remote Sensing. 45(1):88–112.

Bartuska, A. 2006. Why biomass is important: The role of the USDA forest service in managing and using biomass for energy and other uses. Research & Development, USDA Forest Service. 1–16 p.

Belton, D., S. Moncrieff, and J. Chapman. 2013. Processing tree point clouds using Gaussian Mixture Models. ISPRS Annals of Photogrammetry, Remote Sensing and Spatial Information Sciences. II-5/W2:43–48.

Berveglieri, A., A. Tommaselli, X. Liang, and E. Honkavaara. 2017. Vertical Optical Scanning with Panoramic Vision for Tree Trunk Reconstruction. Sensors. 17(12):2791.

Bitterlich, W. 1984. The relascope idea. Relative measurements in forestry. Commonwealth Agricultural Bureaux.

Bouvier, M., S. Durrieu, R. A. Fournier, and J.-P. Renaud. 2015. Generalizing predictive models of forest inventory attributes using an area-based approach with airborne LiDAR data. Remote Sensing of Environment. 156:322–334.

Brown, S. 1999. Guidelines for inventorying and monitoring carbon offsets in forest-based projects. Winrock International for the World Bank. Arlington, VA, USA.

Brown, S. 2002. Measuring, monitoring, and verification of carbon benefits for forest–based projects Swingland, I.R., E.C. Bettelheim, J. Grace, G.T. Prance, and L.S. Saunders (eds.). Philosophical Transactions of the Royal Society of London. Series A: Mathematical, Physical and Engineering Sciences. 360(1797):1669–1683.

Chen, Y., J. A. Kershaw, Y.-H. Hsu, and T.-R. Yang. 2020. Carbon estimation using sampling to correct LiDAR-assisted enhanced forest inventory estimates. The Forestry Chronicle. 96(01):9–19.

Chen, Y., T.-R. Yang, Y.-H. Hsu, J. A. Kershaw, and D. Prest. 2019. Application of big BAF sampling for estimating carbon on small woodlots. For. Ecosyst. 6(1):13.

Clark, M. L., D. A. Roberts, J. J. Ewel, and D. B. Clark. 2011. Estimation of tropical rain forest aboveground biomass with small-footprint lidar and hyperspectral sensors. Remote Sensing of Environment. 115(11):2931–2942.

Dassot, M., T. Constant, and M. Fournier. 2011. The use of terrestrial LiDAR technology in forest science: application fields, benefits and challenges. Annals of Forest Science. 68(5):959–974.

DeCourt, N. 1956. Utilisation de la photographie pour mesurer les surfaces terrières (The use of photography for measuring basal area). Rev. For. Fr. 8(7):505–507. 7th ed. Rev. For. Fr. 505–507 p.

Dick, A. R. 2012. Forest inventory using a camera: Concept, field implementation and instrument development.

Dick, A. R., J. A. Kershaw, and D. A. MacLean. 2010. Spatial Tree Mapping Using Photography. Northern Journal of Applied Forestry. 27(2):68–74.

Donnelly, J. G., M. B. Lavigne, and R. S. van Nostrand. 1986. Precommercial Thinning Spacing Trials Established Between 1979 and 1985. Newfoundland Forestry Centre, St. John's, Newfoundland.

Ducey, M. J., and R. Astrup. 2013. Adjusting for nondetection in forest inventories derived from terrestrial laser scanning. Canadian Journal of Remote Sensing. 39(5):410–425.

Fastie, C. L. 2010. Estimating stand basal area from forest panoramas. In Proceedings of the Fine International Conference on Gigapixel Imaging for Science. :1.

Greaves, H. E., L. A. Vierling, J. U. H. Eitel, N. T. Boelman, T. S. Magney, C. M. Prager, and K. L. Griffin. 2015. Estimating aboveground biomass and leaf area of

low-stature Arctic shrubs with terrestrial LiDAR. Remote Sensing of Environment. 164:26–35.

Hawbaker, T. J., N. S. Keuler, A. A. Lesak, T. Gobakken, K. Contrucci, and V. C. Radeloff. 2009. Improved estimates of forest vegetation structure and biomass with a LiDAR-optimized sampling design: LIDAR-OPTIMIZED SAMPLING. J. Geophys. Res. 114(G2):n/a-n/a.

Hayashi, R., J. A. Kershaw, and A. Weiskittel. 2015. Evaluation of alternative methods for using LiDAR to predict aboveground biomass in mixed species and structurally complex forests in northeastern North America. MCFNS. 7(2):49–65.

Hilker, T., N. C. Coops, G. J. Newnham, M. van Leeuwen, M. A. Wulder, J. Stewart, and D. S. Culvenor. 2012. Comparison of Terrestrial and Airborne LiDAR in Describing Stand Structure of a Thinned Lodgepole Pine Forest. Journal of Forestry. 110(2):97–104.

Hilker, T., M. van Leeuwen, N. C. Coops, M. A. Wulder, G. J. Newnham, D. L. B. Jupp, and D. S. Culvenor. 2010. Comparing canopy metrics derived from terrestrial and airborne laser scanning in a Douglas-fir dominated forest stand. Trees. 24(5):819–832.

Hsu, Y.-H. 2019. Applications of variable probability sampling using remotely sensed covariates. MSc Forestry Thesis, University of New Brunswick, Fredericton, NB, Canada. Available online at: https://unbscholar.lib.unb.ca/islandora/object/unbscholar%3A9861.

Husch, B. 1980. How to determine what you can afford to spend for inventories. US Forest Service, Washington Office, General Technical Report. (WO-28).

Iles, K. 2003. A sampler of inventory topics. Kim Isles & Associates Ltd., Nanimo. British Columbia, Canada.

Jucker, T., J. Caspersen, J. Chave, C. Antin, N. Barbier, F. Bongers, M. Dalponte, et al. 2017. Allometric equations for integrating remote sensing imagery into forest monitoring programmes. Glob Change Biol. 23(1):177–190.

Kankare, V., M. Holopainen, M. Vastaranta, E. Puttonen, X. Yu, J. Hyyppä, M. Vaaja, H. Hyyppä, and P. Alho. 2013. Individual tree biomass estimation using terrestrial laser scanning. ISPRS Journal of Photogrammetry and Remote Sensing. 75:64–75.

Kershaw, J. A., M. J. Ducey, T. W. Beers, and Bertram. Husch. 2016. Forest mensuration. Fifth edition. John Wiley & Sons.

Lakens, D. 2017. Equivalence tests: A practical primer for t-tests, correlations, and meta-analyses. Social Psychological and Personality Science. 1:1--8.

Lambert, M.-C., C.-H. Ung, and F. Raulier. 2005. Canadian national tree aboveground biomass equations. Canadian Journal of Forest Research. 35(8):1996–2018.

Le Toan, T., S. Quegan, M. W. J. Davidson, H. Balzter, P. Paillou, K. Papathanassiou, S. Plummer, et al. 2011. The BIOMASS mission: Mapping global forest biomass to better understand the terrestrial carbon cycle. Remote Sensing of Environment. 115(11):2850–2860.

Lefsky, M. A., W. B. Cohen, G. G. Parker, and D. J. Harding. 2002. Lidar Remote Sensing for Ecosystem Studies. BioScience. 52(1):19.

Levia, D. F. 2008. A generalized allometric equation to predict foliar dry weight on the basis of trunk diameter for eastern white pine (Pinus strobus L.). Forest Ecology and Management. 255(5–6):1789–1792.

Li, A., N. F. Glenn, P. J. Olsoy, J. J. Mitchell, and R. Shrestha. 2015. Aboveground biomass estimates of sagebrush using terrestrial and airborne LiDAR data in a dryland ecosystem. Agricultural and Forest Meteorology. 213:138–147.

Li, S., L. J. Quackenbush, and J. Im. 2019. Airborne Lidar Sampling Strategies to Enhance Forest Aboveground Biomass Estimation from Landsat Imagery. Remote Sensing. 11(16):1906.

Lin, J., M. Wang, M. Ma, and Y. Lin. 2018. Aboveground Tree Biomass Estimation of Sparse Subalpine Coniferous Forest with UAV Oblique Photography. Remote Sensing. 10(11):1849.

Lu, D. 2006. The potential and challenge of remote sensing-based biomass estimation. International Journal of Remote Sensing. 27(7):1297–1328.

Lu, M.-K., T. Y. Lam, B.-H. Perng, and H.-T. Lin. 2019. Close-range photogrammetry with spherical panoramas for mapping spatial location and measuring diameters of trees under forest canopies. Can. J. For. Res. 49(8):865–874.

Lynch, T. B. 2017. Optimal plot size or point sample factor for a fixed total cost using the Fairfield Smith relation of plot size to variance. Forestry. :foresj;cpw038v1.

McElhinny, C. 2005. Quantifying stand structural complexity in woodland and dry sclerophyll forest, South-Eastern Australia. Available online at: https://openresearch-repository.anu.edu.au/handle/1885/47854; last accessed January 31, 2020.

Meyer, V., S. S. Saatchi, J. Chave, J. W. Dalling, S. Bohlman, G. A. Fricker, C. Robinson, M. Neumann, and S. Hubbell. 2013. Detecting tropical forest biomass dynamics from repeated airborne lidar measurements. Biogeosciences. 10(8):5421–5438.

Moskal, L. M., and G. Zheng. 2011. Retrieving Forest Inventory Variables with Terrestrial Laser Scanning (TLS) in Urban Heterogeneous Forest. Remote Sensing. 4(1):1–20.

Mulverhill, C., N. C. Coops, P. Tompalski, C. W. Bater, and A. R. Dick. 2019. The utility of terrestrial photogrammetry for assessment of tree volume and taper in boreal mixedwood forests. Annals of Forest Science. 76(3):83.

Næsset, E. 2002. Predicting forest stand characteristics with airborne scanning laser using a practical two-stage procedure and field data. Remote Sensing of Environment. 80(1):88–99.

Palace, M., F. B. Sullivan, M. Ducey, and C. Herrick. 2016. Estimating Tropical Forest Structure Using a Terrestrial Lidar Zang, R. (ed.). PLoS ONE. 11(4):e0154115.

Pan, Y., R. A. Birdsey, J. Fang, R. Houghton, P. E. Kauppi, W. A. Kurz, O. L. Phillips, et al. 2011. A Large and Persistent Carbon Sink in the World's Forests. Science. 333(6045):988–993.

Pearson, T. R. H., S. L. Brown, and R. A. Birdsey. 2007. Measurement guidelines for the sequestration of forest carbon. U.S. Department of Agriculture, Forest Service, Northern Research Station, Newtown Square, PA. Available online at: https://www.fs.usda.gov/treesearch/pubs/13292; last accessed January 16, 2020.

Perng, B.-H., T. Y. Lam, and M.-K. Lu. 2018. Stereoscopic imaging with spherical panoramas for measuring tree distance and diameter under forest canopies. Forestry: An International Journal of Forest Research. 91(5):662–673.

Pflugmacher, D., W. Cohen, R. Kennedy, and M. Lefsky. 2008. Regional Applicability of Forest Height and Aboveground Biomass Models for the Geoscience Laser Altimeter System. Forest Science. 54(6):647–657.

R Development Core Team. 2019. R: A Language and Environment for Statistical Computing. The R Foundation for Statistical Computing, c/o Institute for Statistics and Mathematics, 1020 Vienna, Austria. Available online at: https://www.r-project.org/.

Reutebuch, S. E., H.-E. Andersen, and R. J. McGaughey. 2005. Light Detection and Ranging (LIDAR): An Emerging Tool for Multiple Resource Inventory. Journal of Forestry. 103(6):286–292.

Ricoh Imaging Company, LTD. 2016. Rioch Theta S 360 video camera. Available online at: http://www.ricoh-imaging.co.jp/english/products/theta_s/; last accessed November 29, 2018.

Robinson, A. P., and R. E. Froese. 2004. Model validation using equivalence tests. Ecological Modelling. 176(3–4):349–358.

Staudhammer, C. L., and V. M. LeMay. 2001. Introduction and evaluation of possible indices of stand structural diversity. Can. J. For. Res. 31(7):1105–1115.

Stewart, B. 2004. Using a camera as an angle gauge in angle-count sampling.

Vaglio Laurin, G., Q. Chen, J. A. Lindsell, D. A. Coomes, F. D. Frate, L. Guerriero, F. Pirotti, and R. Valentini. 2014. Above ground biomass estimation in an African

tropical forest with lidar and hyperspectral data. ISPRS Journal of Photogrammetry and Remote Sensing. 89:49–58.

Wang, H. 2019. Estimating forest attributes from spherical images. MSc Forestry Thesis, University of New Brunswick, Fredericton, NB, Canada. Available online at: https://unbscholar.lib.unb.ca/islandora/object/unbscholar%3A10158.

Wang, H., J. A. Kershaw, T.-R. Yang, Y.-H. Hsu, X. Ma, and Y. Chen. 2020. An Integrated System for Estimating Forest Basal Area from Spherical Images. Mathematical and Computational Forestry and Natural-Resource Sciences. 12.

White, J. C., N. C. Coops, M. A. Wulder, M. Vastaranta, T. Hilker, and P. Tompalski. 2016. Remote Sensing Technologies for Enhancing Forest Inventories: A Review. Canadian Journal of Remote Sensing. 42(5):619–641.

White, J. C., M. A. Wulder, A. Varhola, M. Vastaranta, N. C. Coops, B. D. Cook, D. Pitt, and M. Woods. 2013. A best practices guide for generating forest inventory attributes from airborne laser scanning data using an area-based approach. The Forestry Chronicle. 89(06):722–723.

Yang, T.-R., Y.-H. Hsu, J. A. Kershaw, E. McGarrigle, and Dan Kilham. 2017. Big BAF sampling in mixed species forest structures of northeastern North America: influence of count and measure BAF under cost constraints. Forestry: An International Journal of Forest Research. 90(5):649–660.

Yang, T.-R., J. A. Kershaw, A. R. Weiskittel, T. Y. Lam, and E. McGarrigle. 2019. Influence of sample selection method and estimation technique on sample size requirements for wall-to-wall estimation of volume using airborne LiDAR. Forestry: An International Journal of Forest Research. 92(3):311–323.

Zar, J. H. 2009. Biostatistical analysis. 5th ed. Pearson Prentice-Hall, Upper Saddle River, New York. NJ. 944 p.

Zhao, F., Q. Guo, and M. Kelly. 2012. Allometric equation choice impacts lidar-based forest biomass estimates: A case study from the Sierra National Forest, CA. Agricultural and Forest Meteorology. 165:64–72.

Chapter 3 Sector Subsampling for Basal Area Ratio Estimation: An Alternative to Big BAF Sampling

Abstract

Big Basal Area Factor (big BAF) sampling is a widely used subsampling method to select measure–trees. Several studies have shown big BAF sampling to be an efficient sampling scheme. In this study we use sector sampling (Smith et al. 2008, For. Sci. 54, 67–76) as an alternative subsample selection method. Based on some simulated mapped stands derived from three balsam fir (*Abies balsamae*) spacing trials in western Newfoundland, we show that sector subsampling is comparable to big BAF sampling in terms of estimated mean basal area ratios and their associated standard errors. Differences between big BAF sampling and sector sampling methods showed less than 1% difference across the three sites. As with big BAF sampling, changes in sample intensity had no significant ($p < 0.05$) effects on the accuracy of estimating mean biomass to basal area ratios and the resulting estimated mean biomasses per unit area.

Key Words: sector sampling, subsampling, basal area ratio estimation, sample efficiency, big BAF sampling, biomass estimation

Introduction

Many forest-level attributes, such as volume, biomass, and carbon, rely on individual tree measurements and allometric models (Kershaw et al. 2016). Direct measurement of these attributes is often impractical, expensive, destructive, and, therefore limited to research efforts to develop allometric relationships (Ketterings et al. 2001; Jenkins et al. 2003). For

volume and biomass estimation, allometric models that include both diameter at breast height (DBH) and total height (HT) are often more accurate and applicable to a wider range of stand conditions and ages than models that only use DBH (Honer 1967; Lambert et al. 2005; Ung et al. 2008; Kershaw et al. 2016). However, measurement of height is costly relative to counting sample trees and measuring DBHs (Iles 2003; Lynch 2017; Yang et al. 2017).

Subsampling of plot trees has long been used in forest inventory (Iles 2003; Marshall et al. 2004). Unfortunately, many selection methods were ad hoc or haphazard at best (Iles 2003) with the potential of introducing selection bias at the subsampling stage. An easily implemented solution to this is big Basal Area Factor sampling (BAF). Big BAF sampling is a form of horizontal point sampling (HPS) that utilizes two angle gauges: a small one to count "in" trees; and a larger one to select trees to measure (Iles 2003; Marshall et al. 2004; Yang et al. 2017). The "measure–trees" are used to estimate the ratio of the tree attribute of interest (volume, biomass, carbon content, and so on) to tree basal area ($XBAR_i = X_i/BA_i$; where XBAR is the tree attribute to tree basal area ratio of the ith tree, X_i is the attribute of interest for the ith tree and BA_i is the basal area (cross-sectional area) of the ith tree). The estimated mean XBAR across all measure–trees is multiplied by the estimated mean basal area per unit area determined from the count trees to obtain the estimated mean per unit area estimate of the attribute(s) of interest.

Because plot to plot variability in tree counts is often much greater than variability in XBAR between measure–trees, sampling effort is concentrated on sampling more count plots (Iles 2003; Marshall et al. 2004). Yang et al. (2019) developed methods for optimizing small and large BAF choice for volume estimation and Chen et al. (2019) generalized those

results for volume, biomass, and carbon content. Chen et al. (2020) further applied big BAF sampling on a forest-level scale to correct LiDAR-derived enhanced forest inventory estimates to develop base-line carbon estimates for a carbon offset project. The ability to estimate biomass, and subsequently carbon, in a statistical accurate, and cost-effective manner, is important for developing improved forest management projects for monetized carbon offset projects (Chen et al. 2019, 2020).

While big BAF sampling is very efficient (in terms of its cost-variance tradeoff) and logistically easy to implement in the field, it is just one of many potential subsampling schemes that could be applied to the problem of efficiently selecting trees to measure (Iles 2003 pp. 562-567). Selection based on probability proportional to prediction and systematic list sampling are other potential methods commonly used (Iles 2003). Sector sampling (Iles and Smith 2006; Smith and Iles 2012) is another potential subsampling scheme based on randomly selected sectors radiating from plot centers. Originally developed to sample small or irregular-shaped forest areas (Iles and Smith 2006), sector sampling, though not widely applied, has the potential to be a very efficient sampling scheme in certain situations. The sector orientation is randomly selected and all trees within the sector radiating from plot center to the boundary of the area of interest are measured (Iles and Smith 2006; Smith and Iles 2012). The angle of the sector is usually predetermined and all trees within a sector will be sampled with equal probability.

Sector sampling is commonly applied to small/fixed–areas regardless of boundary shapes or vegetation types (Iles and Smith 2006; Smith and Iles 2012). This approach is an unbiased sampling design when appropriate randomization procedures and estimating procedures are used, because all trees within each sector are sampled from vertex point to

the edge of the angle border (Lynch 2006) and can be scaled to forest-level parameters. If sector azimuths are chosen at random, tract totals and mean tree attributes can be estimated using a simple expansion factor approach (Iles and Smith 2006). Per unit area estimates require a ratio of means approach to account for different sector sizes (Smith et al. 2008; Smith and Iles 2012). The simplicity of implementing sector sampling in small areas makes it a potentially ideal alternative to big BAF sampling in some sampling situations. To our knowledge, no one has explored the potential of sector sampling as an alternative subsampling scheme similar to big BAF sampling.

The specific objectives of this study were: 1) Estimate the efficiency of sector sample selection in comparison with big BAF selection for estimating aboveground biomass; and 2) Determine the effects of sample intensity across the three different subsampling selection methods used in this study.

Materials and Methods

Study sites

Data from three early spacing trials located on western Newfoundland Island (NL), Canada were used in this study (Figure 3. 1). The spacing trials were established in the early 1980s by the government of Newfoundland in cooperation with the Canadian Forest Service (Donnelly et al. 1986). The sites were dominated by balsam fir (*Abies balsamea* L.) with minor components of black spruce (*Picea mariana* (Mill.) Britton, Sterns & Poggenb.) and white birch (*Betula papyrifera* Marshall). There were five spacing treatments: Control, or no spacing, (S00), 1.2m spacing (S12), 1.8m spacing (S18), 2.4m spacing (S24) and 3.0m spacing (S30). The treatments were arranged in a randomized complete block design with

3 replicates per site (3×3×5 = 45 permanent sample plots were used in this study). Each treatment was applied to a 0.25 ha block (50m x 50m), and a circular permanent sample plot (PSP) was established near the center of each block. The PSP size varied such that there were approximately 100 trees per plot at the time of establishment.

Simulation of subsampling protocols

Each NL plot was expanded to a 1 ha "mapped" plot using simulation of spatial locations and random sampling of individual trees from each PSP's tree list (Figure 3. 2A). For Control plots (S00), locations were randomly assigned by generating random {x,y} coordinates. For thinned plots, the 1 ha area was divided into cells based on average spacing. For example, when applied to the 2.4m spacing in simulations, the 1ha area was divided into 2.4m x 2.4m cells. Within each cell, a tree was randomly located by generating a random {x,y} coordinate within the bounds of the cell and a tree was randomly drawn from the tree list for that PSP with replacement.

A 2-M count BAF (i.e., each treed tallied = $2m^2ha^{-1}$ basal area) was simulated to select count ("IN") trees for basal area estimation (Figure 3. 2B). Three different subsample selection methods were used to select trees for height measurement (Figure 3. 2B). The first used a big BAF approach. Measure–trees were selected using a large BAF. We tested five different big BAFs: 20; 30; 40; 50; and 60 M. The second method used sector sampling to subsample count trees (SectorIN). Five different sector intensities, expressed as a percentage of the full compass (360˚) were used is this study: 10%, 7%, 5%, 4%, and 3%. The midpoint azimuth of the sector was randomly oriented and all count ("IN") trees within the sector were selected for measurement (DBH and height (HT)). The third method used

sectors to select trees, but independent of whether they were count trees or not. All trees within the sector and within a specified distance from plot center (11.28m was used in these simulations) were selected for measurement (DBH and HT). Again, we used five different sector intensities: 1.2%, 1.0%, 0.7%, 0.5%, and 0.4%. The big BAF and two different sets of sector intensities were selected to give approximately the same number of measure–trees across the samples (Table 3. 1). Three points were randomly selected within each 1 ha simulated plot. At each sample point, the count trees and measure–trees were determined. The simulations were repeated 100 times. The walk-through method (Ducey et al. 2004) was used to account for any boundary overlap.

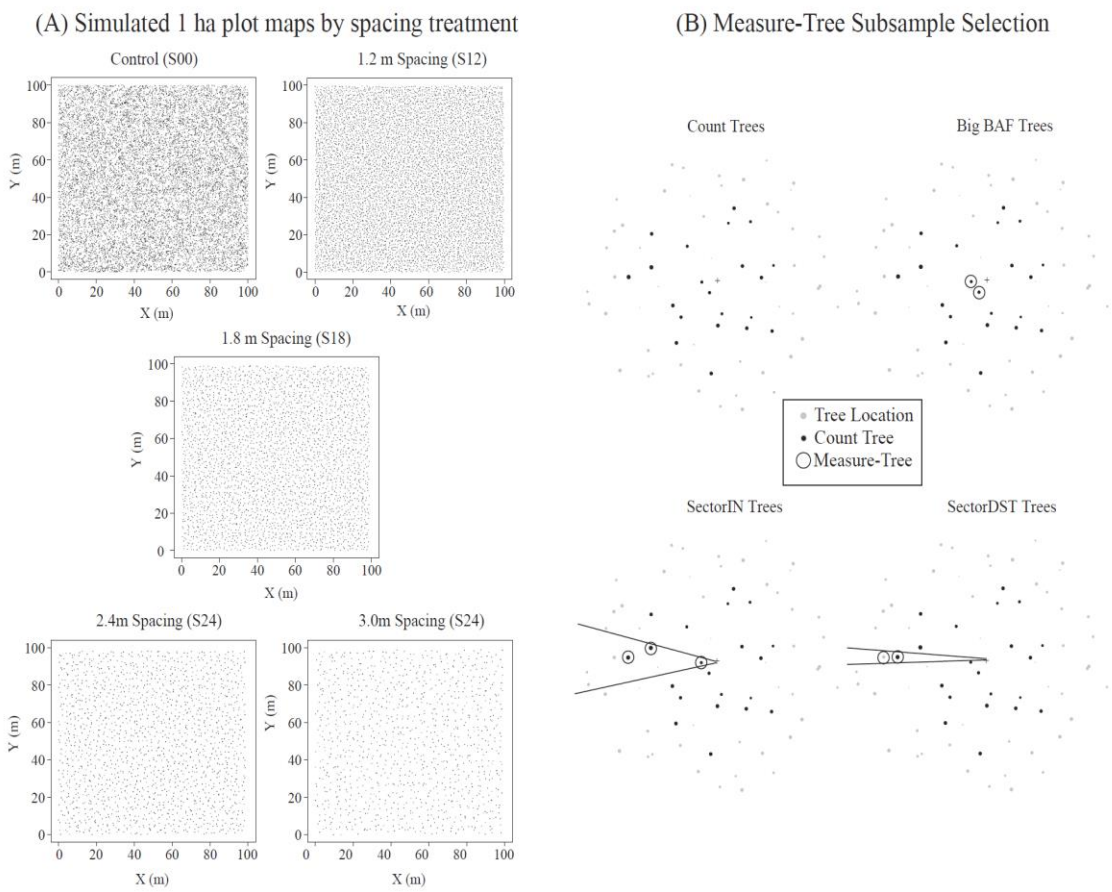

Figure 3. 1 Simulation of (A) 1 ha spacing plots, and (B) count tree selection and the three measure-tree subsample selection methods.

Biomass Estimation

Individual tree biomass was estimated for each tree in the simulated plots using the Canadian National Biomass models (Lambert et al. 2005). We used Eq. 3 from Table 3. 4 in Lambert et al. (2005) which utilized both DBH and HT. Total tree biomass (BM_i) was estimated by summing the separate component biomass estimates (wood, bark, branches, and foliage). For the simulated 1ha plots, "true" field biomass per ha (FBM; tonnes·ha^{-1})

was obtained by summing the biomass estimates across all trees and dividing by 1000 kg·tonne^{-1}:

(1) $$\overline{FBM} = \frac{\sum_{i=1}^{n} BM_i}{1000}$$

The estimated mean biomass to basal area ratio ($\overline{BBAR}$; kg·m^{-2}) was estimated from the measure–trees and used to estimate mean BM for the simulated subsampling methods ($\overline{SBM}$) using estimated $\overline{BA}$:

(2) $$\overline{SBM} = \frac{\overline{BBAR} \cdot \times \overline{BA}}{1000}$$

where,

(3) $$\overline{BA} = \frac{\sum_{j=1}^{p} BA_j}{p} = \frac{\sum_{j=1}^{p} BAF \times Count_j}{p}$$

and p = number of count plots; BA_j = the BA per ha on the jth plot; and $Coun_j$ = the number of "in" trees on the jth plot. The estimation of $\overline{BBAR}$ depended on which subsampling method was employed. Big BAF selection and SectorIN selection were both variable probability methods and the mean ratio approach (Kershaw et al. 2016) was used:

(4a) $$\overline{BBAR} = \frac{\sum_{i=1}^{m} BBAR_i}{m} = \frac{\sum_{i=1}^{m} \left(\frac{BM_i}{BA_i}\right)}{m}$$

For the SectorDST method, measure–trees were selected with equal probability, therefore, we used a ratio of means approach (Kershaw et al. 2016):

(4b) $$\overline{BBAR} = \frac{\sum_{i=1}^{m} BM_i}{\sum_{i=1}^{m} BA_i} = \frac{\sum_{i=1}^{m} BM_i}{\sum_{i=1}^{m} 0.00007854 \times (DBH_i)^2}$$

Percent standard error for $\overline{SBM}$ was estimated from two independent variables based on Bruce's formula (Iles 2003; Marshall et al. 2004; Yang et al. 2017; Chen et al. 2020; Hsu et al. 2020):

(5) $\%se(\overline{SBM}) = \sqrt{\%se(\overline{BA})^2 + \%se(\overline{BBAR})^2}$

where %se() is the estimated standard error as a percent of the estimated mean. Gove et al. (2020) showed the relationship between Bruce's formula and the Delta method. While Bruce's formula does involve an assumption of independence between BA and BBAR, Gove et al. (2020) found in simulations that the impact of non-independence was negligible. For $\%se(\overline{BA})$, and $\%se(\overline{BBAR})$ for bigBAF and sectorIN selection, we used the estimator derived from simple random sampling to estimate standard error (se):

(6a) $se(\bar{x}) = \frac{s}{\sqrt{n}} = \sqrt{\frac{\sum x^2 - (\sum x)^2/n}{n(n-1)}}$

where x is either BA for the sample point or BBAR for the individual measure–tree, s is the estimated standard deviation, and n is sample size (number of sample points or number of measure–trees). For sectorDST selection we used (Kershaw et al. 2016):

(6b) $se(\overline{BBAR}) = \sqrt{\left(\frac{\overline{BBAR}^2}{n(n-1)}\right)\left(\frac{\sum SBM^2}{\overline{SBM}^2} + \frac{\sum BA^2}{\overline{BA}^2} - \frac{2\sum SBM \cdot BA}{\overline{SBM} \cdot \overline{BA}}\right)}$

where, SBM and $\overline{SBM}$ are the biomass estimates for individual sample plots and the estimated mean biomass estimate for the measure–trees; BA and $\overline{BA}$ are the basal areas (cross-section areas) and estimated mean basal area (cross-section area of the measure–trees; and $\overline{BBAR}$ is the estimated mean biomass to basal area ratio from eq. 4b.

The three different measure–tree selection methods were compared on the basis of $\overline{BBAR}$, %se($\overline{BBAR}$), mean biomass estimates and their distributions, equivalence tests and rank correlations by study site and sample intensity. All simulations and analyses were conduction in the R Statistical Language (R Development Core Team 2019).

Results

Estimated BBARs

Estimated $\overline{BBAR}$s (kg·m^{-2}) from the 100 sample simulations using the simulated 1 ha plots did not vary substantially by study site, measure–tree selection method, or sample intensity (Table 3. 2, Figure 3. 3). Overall estimated $\overline{BBAR}$ (mean of the 100 simulated sample means) ranged from about 3000 kg·m^{-2} on Roddickton to 3200 kg·m^{-2} on Cormack and Pasadena (Table 3. 2). Cormack had greater variability in estimated $\overline{BBAR}$ than the other two sites (Figures 3. 3 & 3. 4). Comparisons within study sites but across both measure–tree subsample selection method and measure–tree sample intensity were much closer, with differences consistently well below 1% of the estimated $\overline{BBAR}$s (Table 3. 2).

While overall estimated $\overline{BBAR}$ did not change across the range of sample intensities, the range of estimated $\overline{BBAR}$s (Figure 3. 3) and their associated standard errors (Figure 3. 4) of estimated $\overline{BBAR}$s increased with decreasing sample intensity (Table 3. 2). There were slight biases observed between the overall estimated $\overline{BBAR}$s and the "true" population $\overline{BBAR}$s (Figure 3. 3) as calculated using all trees across the 1 ha simulated plots on each study site. Here, bias is assessed relative to the mean computed from a large number of repeated simulations, which stands in for the unknown population mean. The bias for Roddickton was about twice that observed on the other two sites (≈6% on Roddickton and ≈3% on Cormack and Pasadena); however, this was the result of a single tree measurement with a potential error in measured height (almost double all other trees). When this tree was eliminated from both the population estimate and the measure–tree estimates, the bias was reduced to just under 3%, as observed on the other two sites.

Table 3. 1 Mean number of measure trees, standard errors (in parentheses) and range {in brackets} sample selection methods for the 3 sites (Cormack, Pasadena, Roddickton) by study site, and sample intensity. (Factor levels represent metric BAFs for big BAF sampling and sector width as a percent of a circle for sector sampling)

Study Site	Sample Intensity	Sample Selection Method					
		big BAF		SectorIN		SectorDST	
		Level	Size	Level	Size	Level	Size
Cormack	1	20	100 (7.9) {79, 119}	10	101 (8.2) {76, 122}	1.2	107 (9.6) {87, 137}
	2	30	67 (7.1) {46, 82}	7	71 (7.5) {56, 91}	1.0	90 (9.3) {71, 117}
	3	40	50 (5.8) {38, 63}	5	50 (6.0) {36, 66}	0.7	61 (7.3) {41, 79}
	4	50	40 (5.9) {26, 53}	4	41 (6.0) {27, 57}	0.5	45 (6.8) {29, 61}
	5	60	34 (4.7) {22, 43}	3	30 (4.6) {21, 41}	0.4	36 (6.1) {25, 53}
Pasadena	1	20	154 (8.4) {137,	10	152 (9.8) {130, 184}	1.2	87 (7.7) {68, 108}
	2	30	102 (7.5) {83, 118}	7	107 (8.5) {82, 127}	1.0	72 (7.8) {55, 95}
	3	40	77 (6.7) {63, 92}	5	77 (6.8) {62, 94}	0.7	50 (6.7) {32, 65}
	4	50	62 (6.6) {50, 78}	4	61 (6.8) {45, 77}	0.5	35 (6.19) {22, 52}
	5	60	51 (5.0) {39, 67}	3	46 (5.8) {33, 59}	0.4	29 (4.9) {20, 41}
Roddickton	1	20	116 (8.9) {88, 134}	10	114 (9.2) {93, 145}	1.2	115 (9.9) {94, 134}
	2	30	77 (7.8) {59, 96}	7	80 (7.9) {61, 99}	1.0	95 (9.4) {74, 123}
	3	40	58 (6.2) {44, 79}	5	57 (6.4) {35, 73}	0.7	68 (6.8) {50, 84}
	4	50	46 (5.7) {32, 59}	4	46 (5.5) {34, 61}	0.5	46 (6.5) {30, 63}
	5	60	39 (5.6) {25, 52}	3	34 (5.7) {21, 53}	0.4	38 (6.3) {26, 56}

Biomass estimates

Overall estimated mean biomass (tonnes·ha^{-1}) varied by site, reflecting inherent differences in site productivity across the three sites (Table 3. 2, Figure 3. S1) with Pasadena > Roddickton > Cormack. While overall mean biomass varied across the three sites, estimated mean biomasses, like estimated mean BBARs, did not vary substantially by measure–tree selection method nor sample intensity (Table 3. 2). Similar to estimated BBAR, the range of estimates and the associated standard errors for biomass increased with decreasing sample intensity (Table 2, Figures 3. S1 & 3. S2). However, while measure–tree sample sizes typically decreased by 70% (Table 3. 1), standard errors only increased by 15% or less (Table 3. 2).

For the 100 sample simulations conducted on each site, the nominal 95% confidence intervals included the "true" population means for all replicate samples across all sites × measure–tree selection methods × measure–tree sample intensities (Supplementary Figures 3. S3 – 3. S5). The "true" population mean was calculated as the sum of the individual trees on each simulated 1-ha plot and averaged across the 15 plots within each spacing trial. At the largest measure–tree sample intensities, the correspondences between estimated mean biomass among the three measure–tree subsample selection methods were quite good (Supplementary Figures 3. S6 – 3. S8; Table 3. 3). As sample intensity decreased, the relationships became increasingly noisy (Supplementary Figures 3. S6 – 3. S8), especially for Cormack (Supplementary Figure 3. S6). Spearman's rank correlation decreased with decreasing sample intensity, while the minimum detectable negligible differences increased (Table 3. 3). Even though MDNDs increased with decreasing sample intensity, when expressed as a percentage of standard deviation (Table 3. 3), most were less than

25%, which is generally considered sufficient to conclude the two samples are statistically equivalent (Robinson and Froese 2004).

Discussion

Big BAF sampling is a well-established and increasingly used method for selecting a subsample of measure–trees in a variety of forest inventory applications (Corrin 1998; Desmarais 2002; Iles 2003; Marshall et al. 2004; Yang et al. 2017; Chen et al. 2019). Because variability in counts of "in" trees between sample points is generally greater than the variability in the volume to basal ratio (Marshall et al. 2004; Yang et al. 2017), or biomass to basal area ratio (Chen et al. 2019), big BAF sampling places inventory effort on establishing more count plots than measuring sample trees (Iles 2003; Marshall et al. 2004). The alternative selection methods proposed in this study using sector sampling were comparable to big BAF measure–tree selection in terms of both average BBAR (Table 3. 2, Figure 3. 3) and percent standard error of mean BBAR (Figure 3. 4). Differences in mean BBARs across the three measure–tree selection methods averaged less than 0.2% across the three spacing trials and five sample intensities (Table 3. 3). Because estimated biomass per ha is simply BBAR multiplied by average BA (which was constant for all three sample selection methods and measure–tree sample intensities), biomass per ha did not vary substantially among the measure–tree selection methods as well (Tables 3. 2 & 3. 3).

Table 3. 2 Mean, standard error (in parentheses) and range (in brackets) for estimated BBARs (kg·m^{-2}) and biomass (tonnes·ha^{-1}) by study site, measure-tree selection method and sample intensity for the western Newfoundland (NL) spacing trials. (measure-tree sample intensities are defined in Table 3. 1)

Selection method	Sample intensity	big BAF		SectorIN		SectorDST	
		BBAR	Biomass	BBAR	Biomass	BBAR	Biomass
Cormack	1	3162 (43.0)	140.8 (4.0)	3157 (45.2)	140.6 (4.4)	3164 (55.0)	140.9 (4.4)
		{3066, 3268}	{131.9, 150.9}	{3004, 3305}	{129.9, 152.7}	{2957, 3328}	{129.3, 150.9}
	2	3151 (56.0)	140.3 (4.4)	3162 (48.3)	140.7 (3.6)	3156 (66.4)	140.5 (4.5)
		{3010, 3286}	{128.3, 150.0}	{3008, 3262}	{131.8, 149.5}	{2962, 3322}	{128.5, 151.4}
	3	3153 (58.1)	140.4 (4.3)	3155 (65.9)	140.5 (4.6)	3147 (81.6)	140.1 (5.1)
		{2975, 3285}	{127.3, 151.8}	{2998, 3324}	{130.3, 151.2}	{2917, 3304}	{125.2, 153.0}
	4	3155 (68.9)	140.8 (4.5)	3147 (69.6)	140.5 (4.5)	3146 (83.3)	140.4 (5.3)
		{2934, 3282}	{128.1, 154.3}	{2956, 3285}	{127.4, 151.8}	{2904, 3381}	{128.9, 162.1}
	5	3154 (71.2)	140.4 (4.3)	3151 (89.7)	140.3 (5.3)	3143 (103.7)	139.9 (5.0)
		{2983, 3310}	{128.2, 152.2}	{2899, 3405}	{128.2, 155.5}	{2773, 3353}	{127.4, 153.4}
Pasadena	1	3205 (17.5)	218.7 (3.8)	3205 (20.0)	218.7 (3.9)	3201 (28.7)	218.5 (4.2)
		{3164, 3256}	{209.3, 226.9}	{3149, 3261}	{208.4, 225.9}	{3127, 3268}	{207.5, 227.3}
	2	3204 (25.5)	218.3 (3.8)	3204 (24.5)	218.4 (4.1)	3199 (32.0)	218.0 (4.44)
		{3148, 3272}	{209.0, 226.7}	{3138, 3252}	{208.3, 227.3}	{3120, 3314}	{207.6, 230.3}
	3	3205 (28.1)	219.0 (3.9)	3205 (27.9)	219.1 (3.7)	3198 (43.1)	218.5 (4.6)
		{3132, 3258}	{208.6, 229.9}	{3117, 3272}	{208.8, 227.3}	{3098, 3307}	{207.1, 231.6}
	4	3207 (28.7)	218.8 (3.4)	3209 (32.2)	218.9 (3.8)	3195 (49.7)	217.9 (4.4)
		{3141, 3270}	{210.3, 227.1}	{3136, 3282}	{208.0, 230.2}	{3083, 3365}	{208.2, 232.8}
	5	3208 (35.3)	218.5 (3.9)	3209 (33.1)	218.5 (3.7)	3207 (55.6)	218.4 (5.0)
		{3123, 3297}	{210.2, 230.4}	{3118, 3286}	{209.7, 231.2}	{3052, 3339}	{205.5, 228.7}
Roddickton	1	2924 (26.3)	150.2 (3.7)	2926 (24.7)	150.3 (3.5)	2924 (37.9)	150.1 (3.9)
		{2860, 3003}	{141.4, 160.0}	{2876, 3015}	{140.7, 159.9}	{2835, 3021}	{141.7, 160.3}
	2	2930 (32.5)	150.7 (3.5)	2928 (35.8)	150.6 (3.5)	2933 (45.6)	150.9 (3.8)
		{2848, 3000}	{142.9, 159.5}	{2852, 3022}	{142.4, 159.7}	{2834, 3059}	{143.5, 160.7}
	3	2928 (41.9)	150.0 (3.6)	2921 (42.1)	149.6 (3.7)	2917 (52.0)	149.4 (4.1)
		{2816, 3043}	{139.5, 159.4}	{2785, 3037}	{138.4, 157.4}	{2747, 3069}	{138.7, 160.1}
	4	2927 (42.3)	150.1 (3.7)	2926 (51.7)	150.0 (3.9)	2929 (68.3)	150.2 (4.9)
		{2802, 3013}	{141.9, 162.5}	{2767, 3027}	{139.3, 157.5}	{2773, 3078}	{137.8, 164.4}
	5	2918 (50.2)	149.8 (4.0)	2923 (60.0)	150.1 (4.4)	2919 (67.8)	149.9 (4.8)
		{2784, 3033}	{140.8, 159.5}	{2784, 3084}	{141.1, 160.9}	{2709, 3059}	{137.0, 160.4}

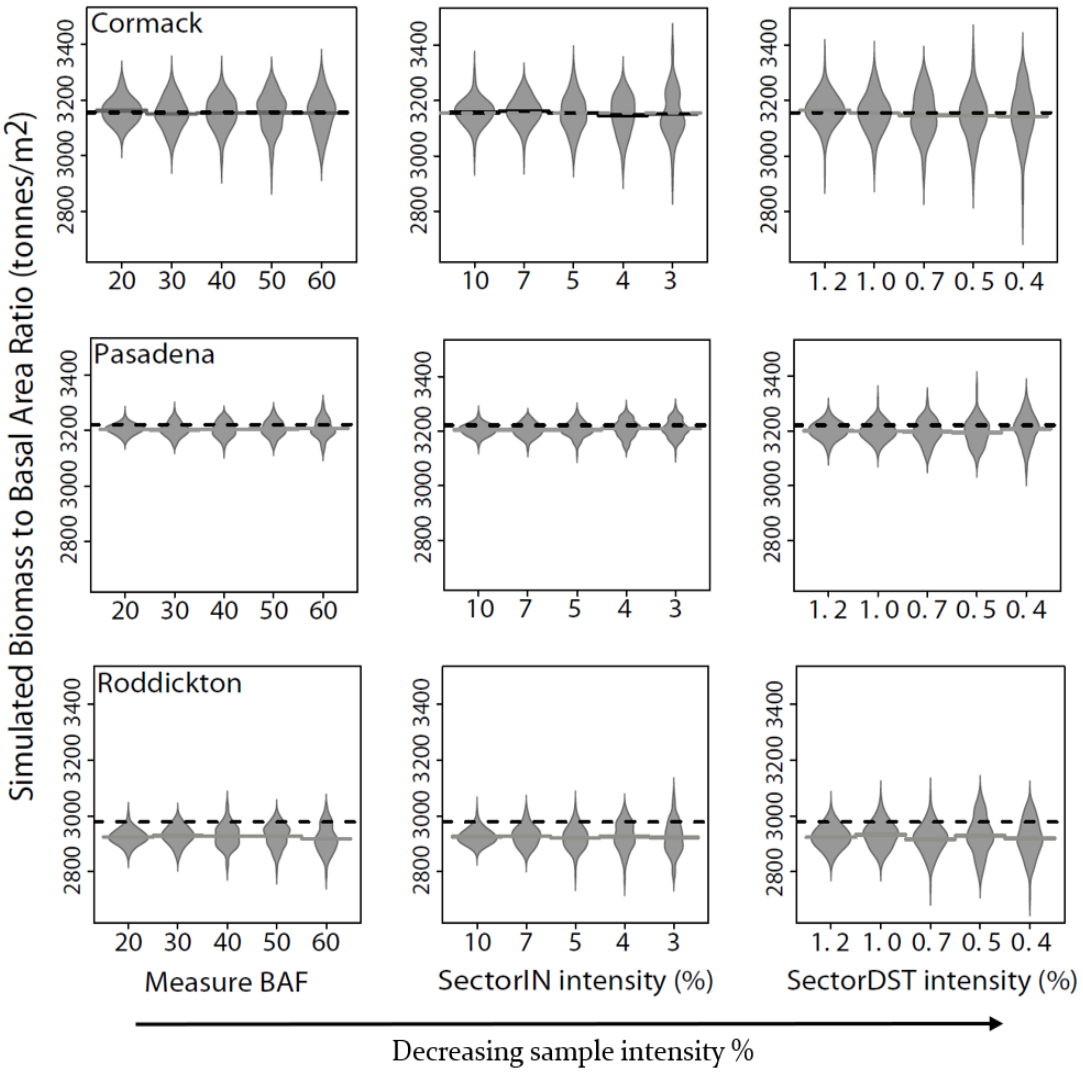

Figure 3. 2 Distribution of BBARs by study site, measure-tree subsample selection method and measure-tree subsample intensity for the Newfoundland (NL) spacing trials. Horizontal black bars are the overall mean BBARs generated from each simulation method under different measure intensities. Dashed black line is the "true" population BBAR. (For Measure BAF, intensity is expressed in terms of metric basal area factors, m^2ha^{-1} per tree tallied, for Sectors intensity is expressed in term of percent of full circle)

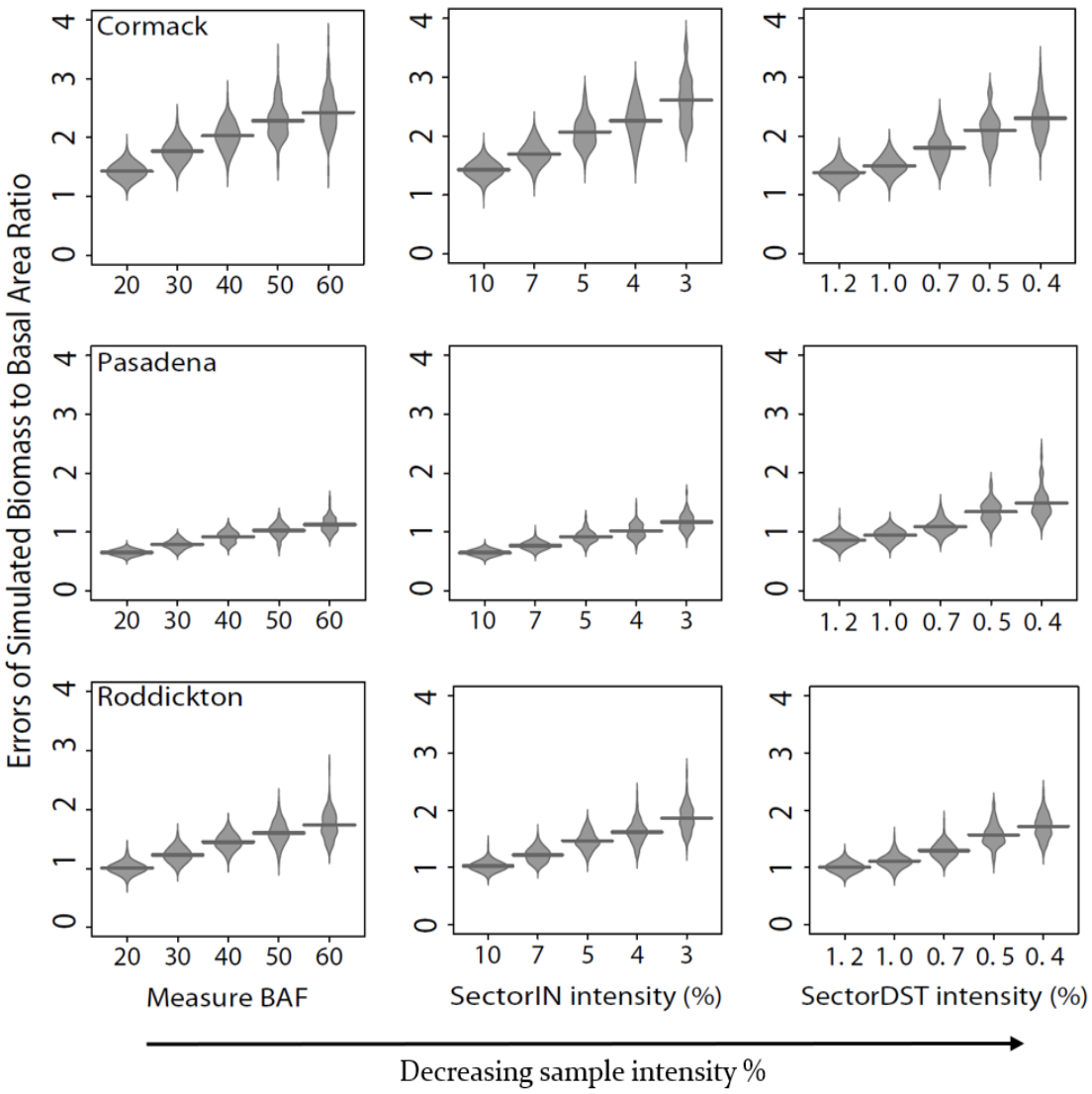

Figure 3. 3 Distribution of BBAR errors by study site, measure-tree subsample selection method and measure-tree subsample intensity for the Newfoundland (NL) spacing trials. Dark grey bars stand for the mean errors generated from each method under different measure intensities. (For Measure BAF, intensity is expressed in terms of metric basal area factors, m^2ha^{-1} per tree tallied, for Sectors intensity is expressed in term of percent of full circle)

Table 3. 3 Comparisons of sample means based on minimum detectable, non-negligible differences (MDND) and Spearman's rank correlation coefficients (γ) by study site, measure-tree selection method, and measure-tree sample intensity for the western Newfoundland spacing trials (MDNDs are expressed in tonnes/ha with percent of standard deviation of differences in parentheses, and represents the minimum percent difference required to reject the null hypothesis of the equivalence test: there IS a significant difference)

Study Site	Sample Intensity[1]	Measure-Tree Selection Method					
		big BAF vs SectorIN		big BAF vs SectorDST		SectorIn vs SectorDST	
		MDND	γ	MDND	γ	MDND	γ
Cormack	1	0.65 (24)	0.83	0.64 (20)	0.70	0.83 (26)	0.77
	2	0.94 (31)	0.72	0.88 (21)	0.57	0.89 (24)	0.60
	3	0.76 (19)	0.60	1.01 (23)	0.55	1.15 (24)	0.52
	4	0.99 (25)	0.58	1.17 (25)	0.46	0.86 (18)	0.46
	5	0.96 (19)	0.39	1.37 (26)	0.42	1.42 (23)	0.25
Pasadena	1	0.28 (17)	0.91	0.62 (27)	0.83	0.66 (26)	0.80
	2	0.44 (19)	0.81	0.74 (27)	0.81	0.83 (29)	0.79
	3	0.48 (18)	0.73	1.09 (30)	0.63	1.09 (32)	0.71
	4	0.66 (22)	0.68	1.43 (39)	0.59	1.66 (42)	0.50
	5	0.62 (20)	0.64	0.78 (17)	0.57	0.89 (20)	0.52
Roddickton	1	0.34 (21)	0.88	0.43 (19)	0.79	0.50 (22)	0.78
	2	0.49 (21)	0.76	0.59 (22)	0.74	0.75 (25)	0.67
	3	0.80 (28)	0.71	1.14 (33)	0.59	0.84 (23)	0.57
	4	0.60 (18)	0.61	0.78 (19)	0.52	0.88 (20)	0.53
	5	0.86 (24)	0.63	0.76 (18)	0.48	1.06 (20)	0.34

[1]Sample Intensities are defined in Table 3. 1

Big BAF selection is a subsampling protocol (Marshall et al. 2004). The trees selected using the big angle gauge are a subset of the trees counted using the small angle gauge (Iles 2003; Marshall et al. 2004). Similarly, the SectorIN selection method proposed here is a subsample of the count trees (Figure 3. 2); however, the SectorDST method is potentially a mixture of count and non-count trees (Figure 3. 2). Both big BAF and SectorIN selection samples trees with variable probability and the mean ratio (Eq. 4a) and its associated standard error (Eq. 6a) were used. The SectorDST method samples with equal probability; therefore, the ratio of means estimator (Eq. 4b) and its associated standard error (Eq. 6b) was used. Despite the different selection probabilities and associate mean and error estimates, all three selection methods had comparable results (Table 3. 2, Figure 3. 3 & 3. 4).

Sector sampling was originally developed to efficiently sample small, irregular areas (Smith and Iles 2012). Because randomness enters the selection process through the azimuth of the sector plot, sector sampling has several interesting properties: 1) placement of the sampling point (sector vertex) can be subjective provided the randomization of the sector azimuth is independent of sector placement; and 2) because selection probabilities are based on sector angle, there are no boundary overlap issues (Iles and Smith 2006; Smith and Iles 2012). Despite these advantages, sector sampling has seen limited application in the field. Sector sampling does not easily scale to larger areas because of the difficulty in tracing sectors over long distances in the field. The applications developed here are a novel use of sector sampling and could be employed as a useful method of subsampling measure–trees on fixed–area plots.

As Lynch (2006) observed, the change in sample size results in variance changes. Here, sample intensity did not influence the means of either BBAR or the associated biomass per hectare estimates; however, variability was greatly impacted (Table 3. 2, Figure 3. 3 & Figure 3. S1). This is similar to results reported by Yang et al. (2017) and Chen et al. (2019) and is consistent with the sampling theory as proposed by Marshall et al. (2004). As Yang et al. (2017) demonstrated, the big BAF can vary from 10 M to almost 100 M without impacting the overall errors of estimates or required sample sizes for estimating volume. The sector sampling methods developed here were comparable to the big BAF approach showing that sector subsampling is a viable alternative to big BAF sampling (Table 3. 2, Figure 3. 4).

Yang et al. (2017) developed methods for analyzing the cost-error surface based on the Fairfield Smith equation (Lynch 2017). Chen et al. (2019) generalized this approach for estimating carbon content in eastern North America and developed methods to optimize choice of small and big BAF. Given the resulting standard errors and the associated numbers of trees requiring measurement, there is no reason to believe that the relationships for sector subsampling would deviate substantially from the relationships established for big BAF selection; however, this needs further study.

While we applied sector subsampling with horizontal point sampling, it could just as easily be applied using fixed–area plots. However, the use of fixed–area plots would require measurement of all tree diameters on both the sector trees and the plot trees to estimate basal area, which would reduce the efficiency of the approach presented here. Hsu (2019) presented some alternative measures to basal area for ratio estimation using spherical

photos. Hsu's (2019) results show that the strength of the correlation between the two variables and the variation in the denominator variable (i.e., the covariate) drive the efficiency of the sampling strategy. With fixed–area plots, stand average canopy height or stand density might be more cost-effective variables to measure in the field than basal area. Biomass to stand height or biomass to density ratios could be estimated and used in place of the biomass to basal area ratios as used here (Iles (2003) demonstrates this for a number of different stand variables). As Hsu (2019) showed for other metrics, these ratios may be more variable, requiring more sample plots and more measurements within a sample plot. The use of alternative ratios requires more study to evaluate the efficiency of these estimators. The Fairfield Smith equation (Lynch 2017; Yang et al. 2017; Chen et al. 2019) may be an approach for evaluating the cost-error surfaces and developing optimal sample designs for these alternative ratios. As Wang (2019) proposed, spherical images were an effective medium for extracting forest attributes. With no restriction on plot shapes, photo plots selected from spherical images combined with sector subsampling may be a promising approach for estimating forest attributes as well.

Acknowledgements

We are grateful to the Newfoundland and Labrador Department of Fisheries, Forestry and Agriculture for the use of their spacing trial data and allowing us access to acquire images on their study sites. This work was partially funded by a Contribution Agreement with the Government of Newfoundland and Labrador and by the Natural Sciences and Engineering Research Council of Canada, Discovery Grant Program (RGPIN04280), and the New Brunswick Innovation Foundation Research Assistantship Initiative (RAI2017-032). The

corresponding author is grateful for an Accelerated Master's Award from the New Brunswick Department of Postsecondary Education and Labour.

Supplemental Material

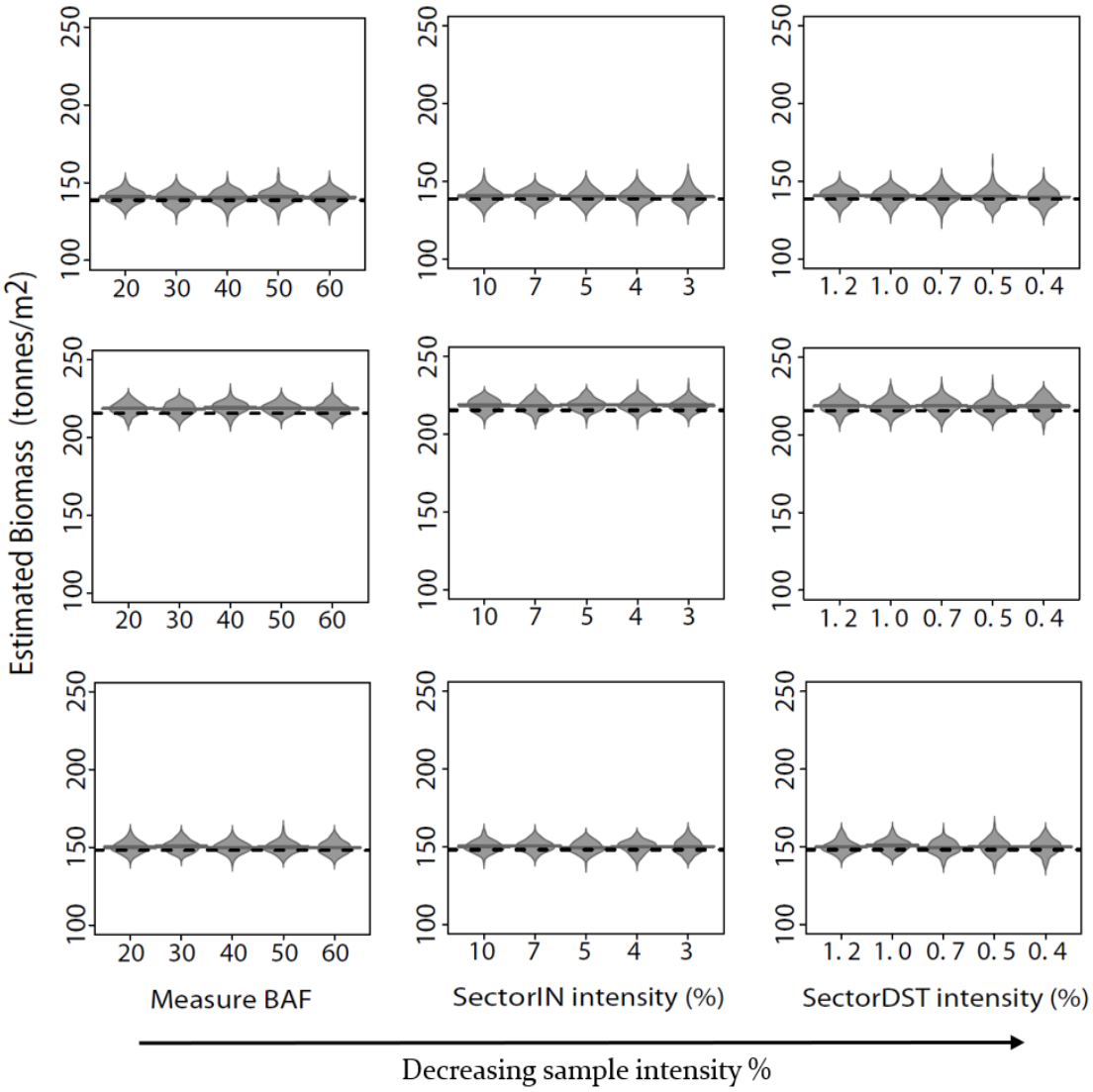

Figure S 1 Distribution of Biomass by study site, measure–tree subsample selection method and measure–tree subsample intensity for the Newfoundland (NL) spacing trials. Horizontal dark grey bars are the overall mean biomass generated from each simulation method under different measure intensities. Dashed black line is the "true" population biomass. (For Measure BAF, intensity is expressed in terms of metric basal area factors, m^2ha^{-1} per tree tallied, for Sectors intensity is expressed in term of percent of full circle)

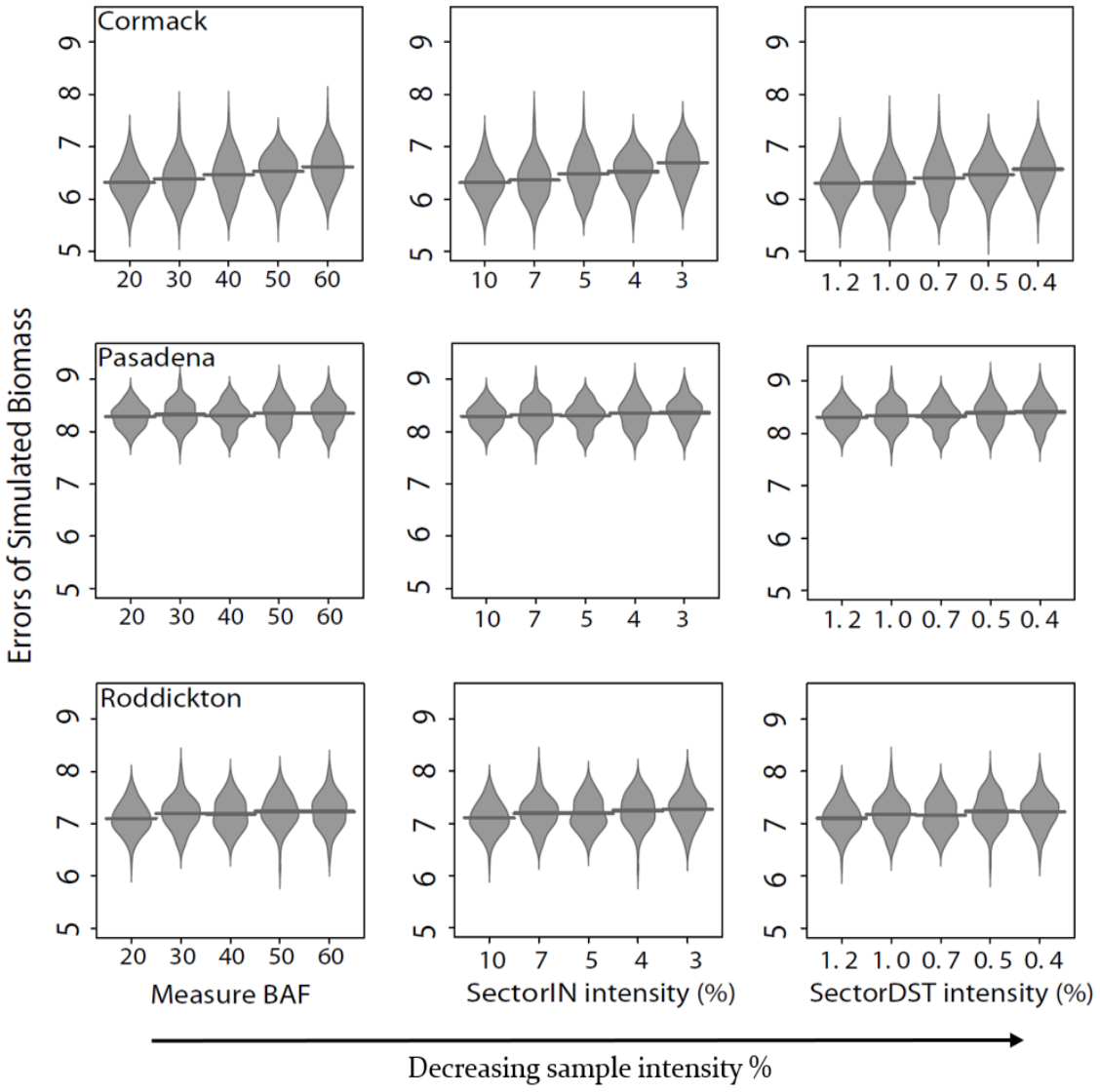

Figure S 2 Distribution of biomass errors by study site, measure–tree subsample selection method and measure–tree subsample intensity for the Newfoundland (NL) spacing trials. Dark grey bars stand for the mean errors generated from each method under different measure intensities. (For Measure BAF, intensity is expressed in terms of metric basal area factors, m^2ha^{-1} per tree tallied, for Sectors intensity is expressed in term of percent of full circle)

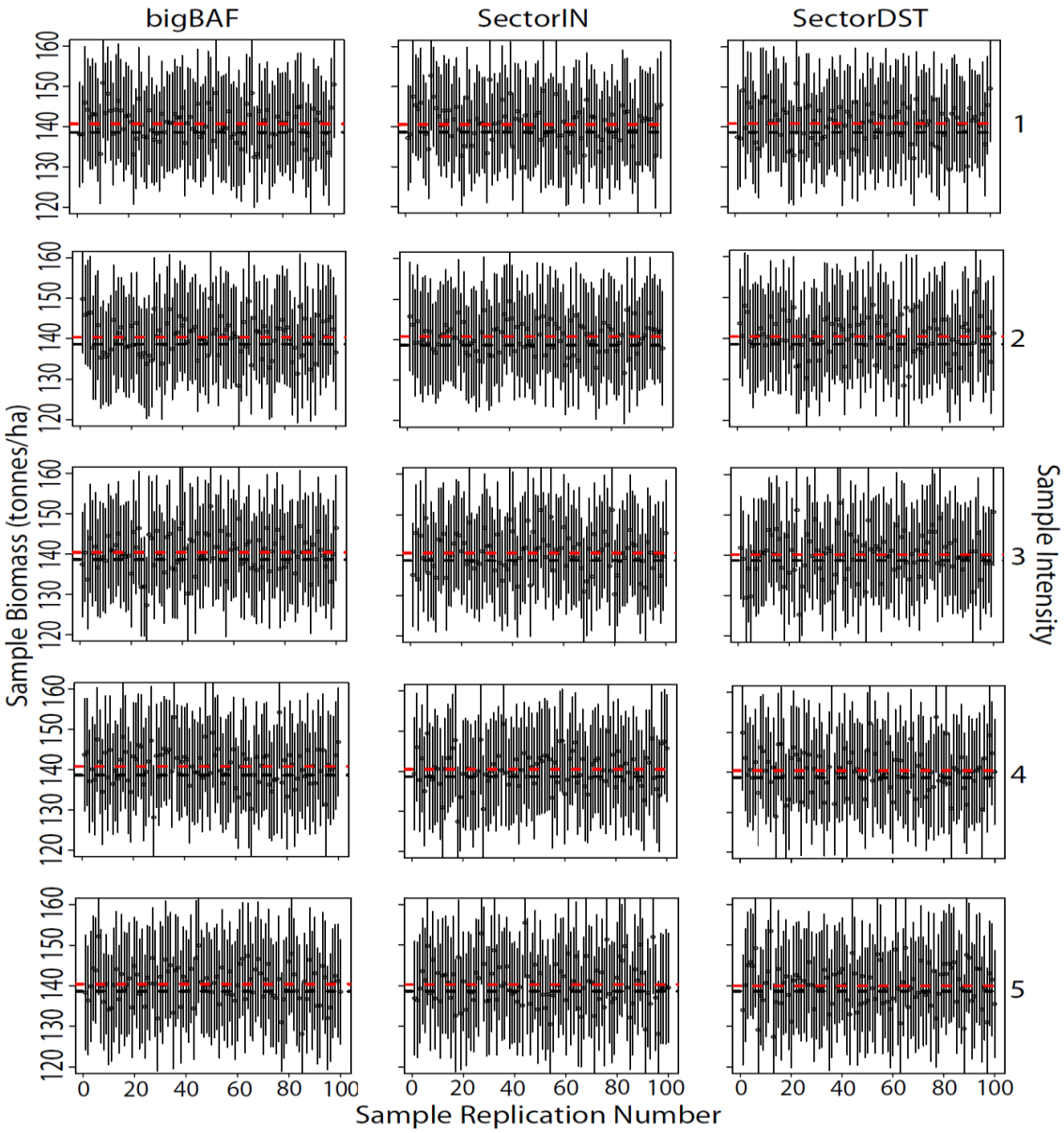

Figure S 3 Distribution of biomass estimates compared with field measurement for simulated plots in Cormack under 3 sample selection methods and different sample intensities, presented with confidence intervals (vertical lines). The dashed black lines stand for the true means of biomass, the dashed red lines stand for simulated means of biomass.

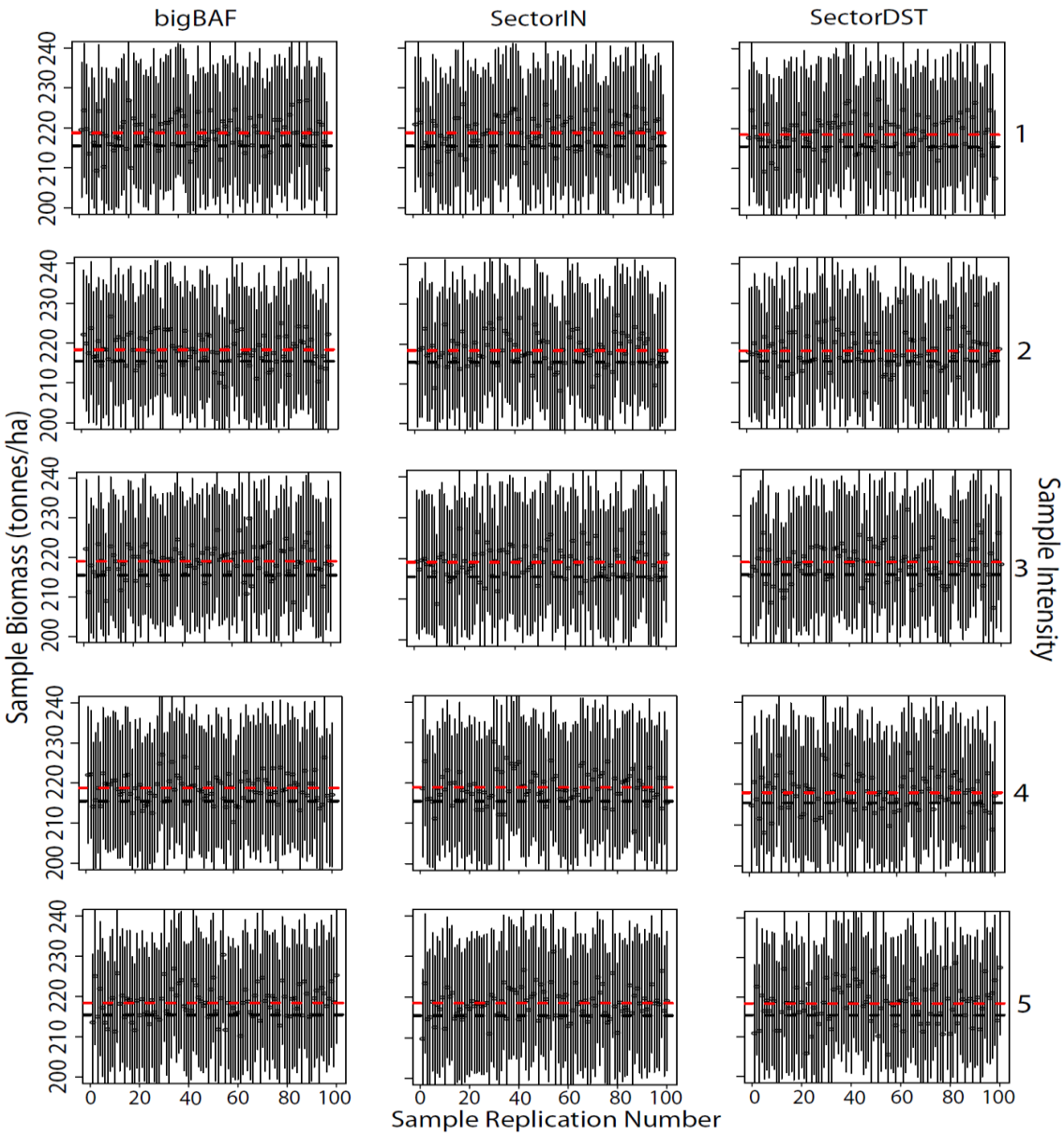

Figure S 4 Distribution of biomass estimates compared with field measurement for simulated plots in Pasadena under 3 sample selection methods and different sample intensities, presented with confidence intervals (vertical lines). The dashed black lines stand for the true means of biomass, the dashed red lines stand for simulated means of biomass.

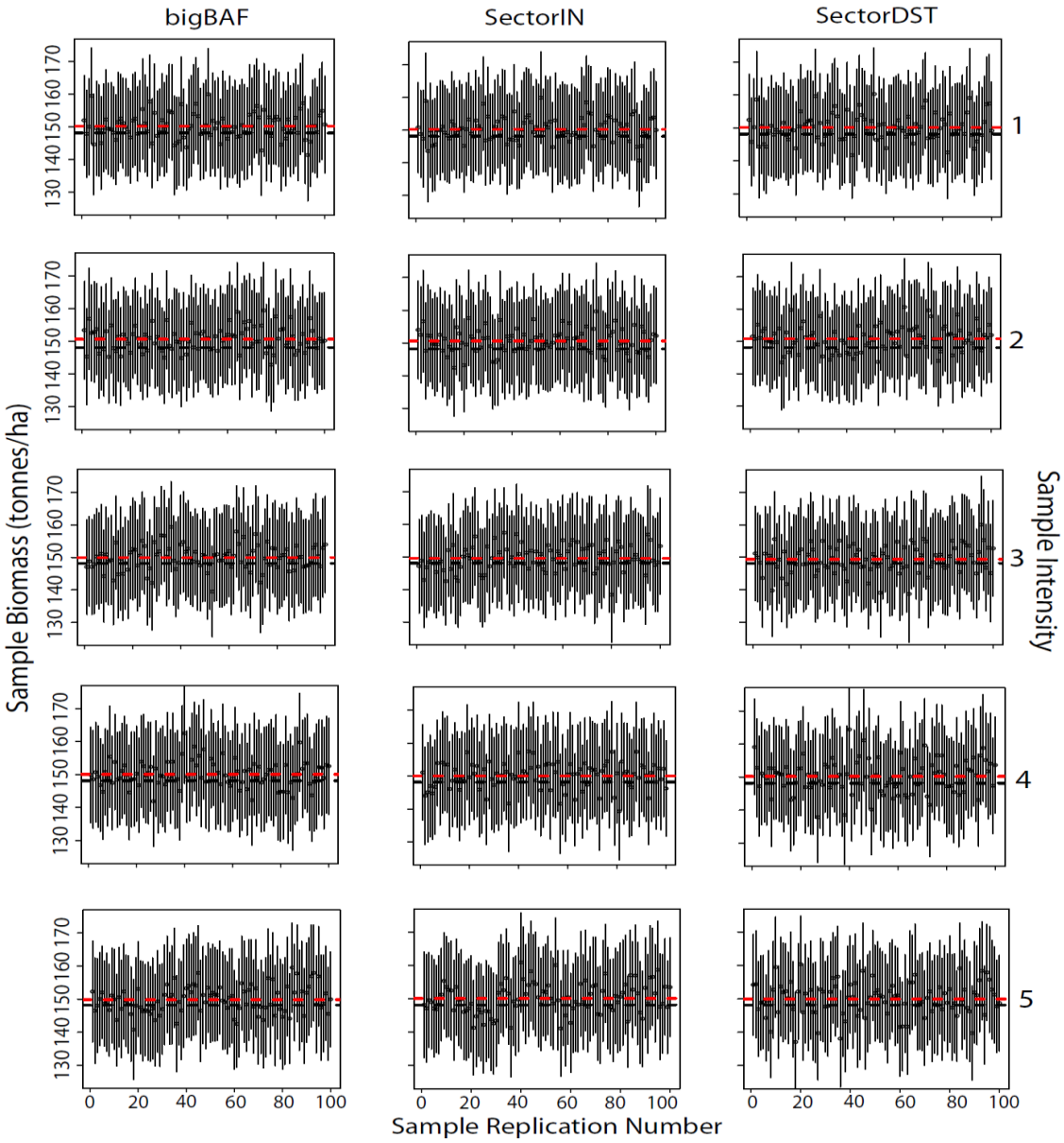

Figure S 5 Distribution of biomass estimates compared with field measurement for simulated plots in Roddickton under 3 sample selection methods and different sample intensities, presented with confidence intervals (vertical lines). The dashed black lines stand for the true means of biomass, the dashed red lines stand for simulated means of biomass.

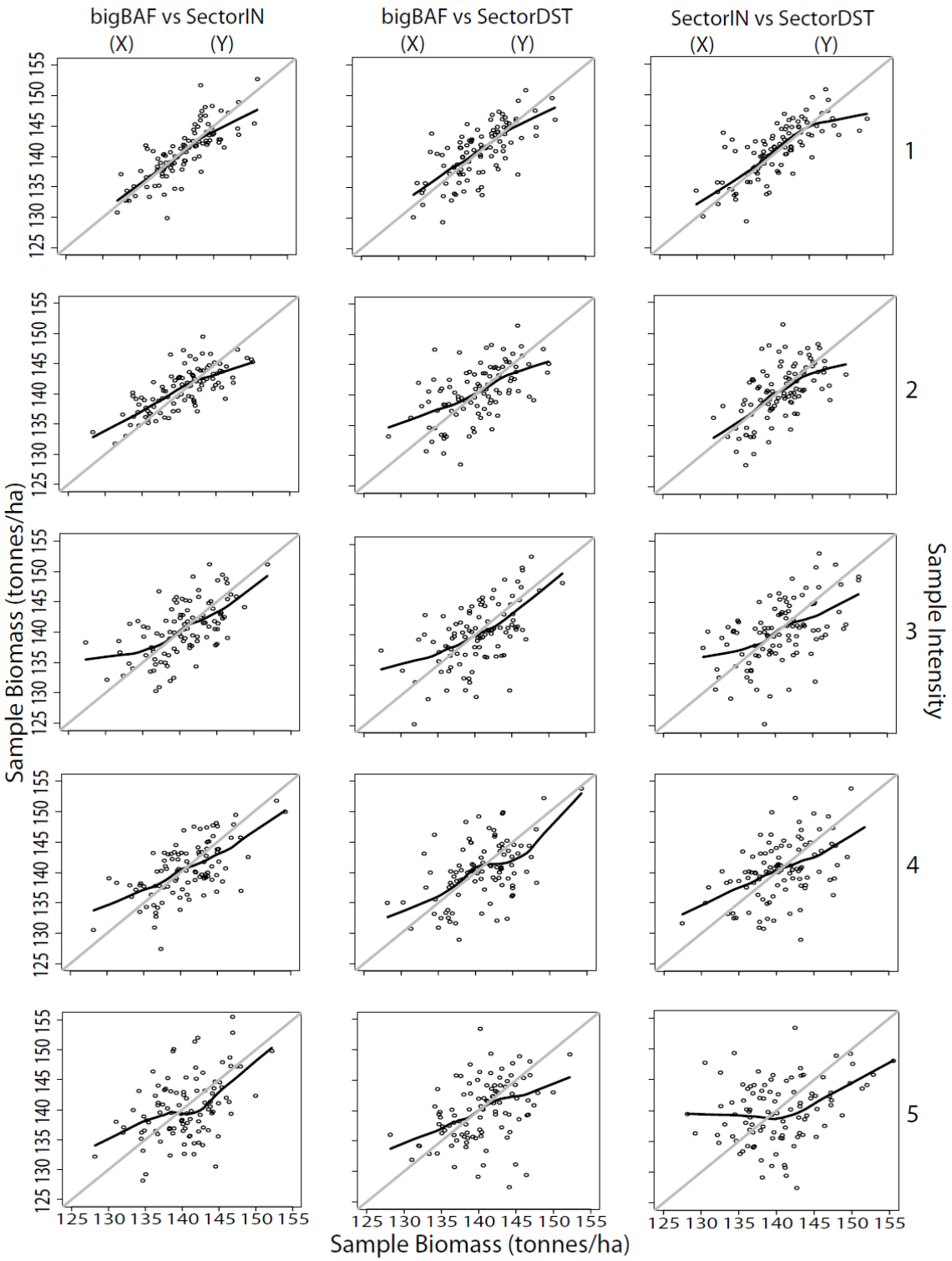

Figure S 6 Comparison of biomass estimates between big BAF, SectorIN and SectorDST under different sample intensities for Cormack. (Sample intensities are defined in Table 1)

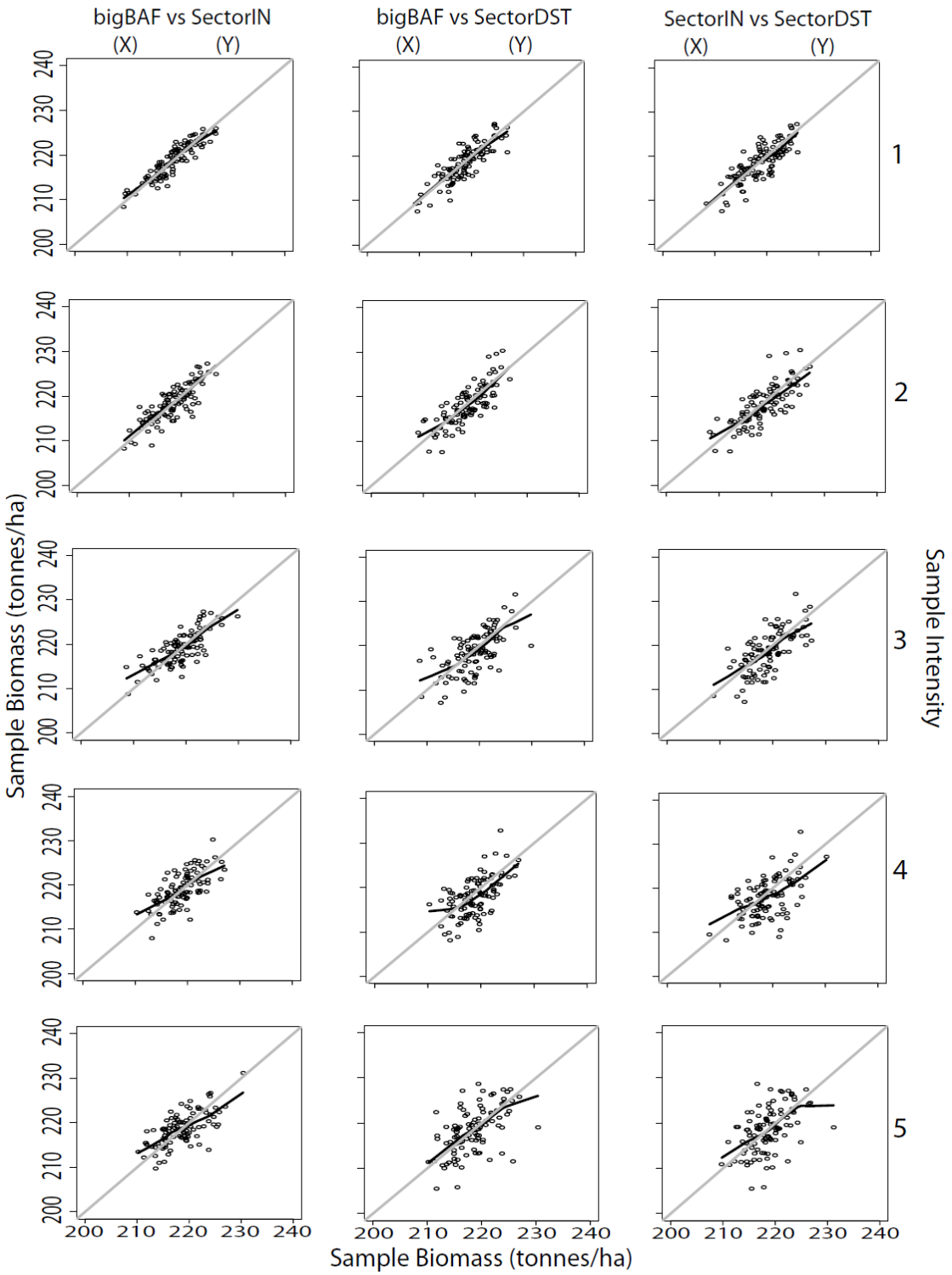

Figure S 7 Comparison of biomass estimates between big BAF, SectorIN and SectorDST under different sample intensities for Pasadena. (Sample intensities are defined in Table 1)

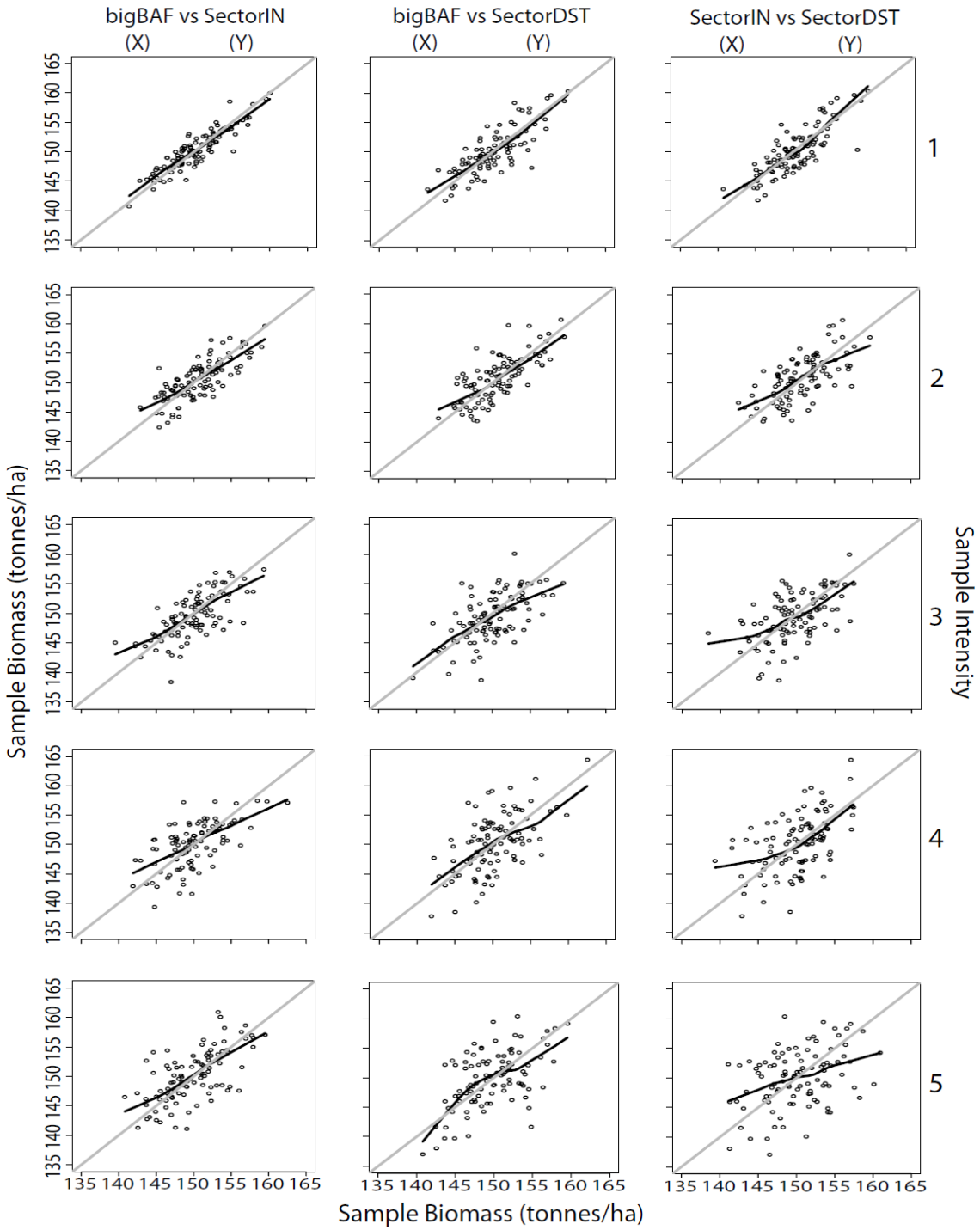

Figure S 8 Comparison of biomass estimates between big BAF, SectorIN and SectorDST under different sample intensities for Roddickton. (Sample intensities are defined in Table 1)

References

Chen, Y., J. A. Kershaw, Y.-H. Hsu, and T.-R. Yang. 2020. Carbon estimation using sampling to correct LiDAR-assisted enhanced forest inventory estimates. The Forestry Chronicle. 96(01):9–19.

Chen, Y., T.-R. Yang, Y.-H. Hsu, J. A. Kershaw, and D. Prest. 2019. Application of big BAF sampling for estimating carbon on small woodlots. For. Ecosyst. 6(1):13.

Corrin, D. 1998. BIG BAF: a very efficient sampling method for cruising timber. John Bell Assoc. 43.

Desmarais, K. M. 2002. Using BigBAF sampling in a New England mixedwood forest. John Bell & Associates Inventory & Cruising Newsletter. 58.

Donnelly, J. G., M. B. Lavigne, and R. S. van Nostrand. 1986. Precommercial Thinning Spacing Trials Established Between 1979 and 1985. Newfoundland Forestry Centre, St. John's, Newfoundland.

Ducey, M. J., J. H. Gove, and H. T. Valentine. 2004. A Walkthrough Solution to the Boundary Overlap Problem. Forest Science. 50(4):427–435.

Gove, J. H., T. G. Gregoire, M. J. Ducey, and T. B. Lynch. 2020. A note on the estimation of variance for big BAF sampling. For. Ecosyst. 7(1):62.

Honer, T. 1967. Standard volume tables and merchantable conversion factors for the commercial tree species of central and eastern Canada.

Hsu, Y.-H. 2019. Applications of variable probability sampling using remotely sensed covariates. MSc Forestry Thesis, University of New Brunswick, Fredericton, NB, Canada. Available online at: https://unbscholar.lib.unb.ca/islandora/object/unbscholar%3A9861.

Hsu, Y.-H., Y. Chen, T.-R. Yang, J. A. Kershaw, and M. J. Ducey. 2020. Sample strategies for bias correction of regional LiDAR-assisted forest inventory Estimates on small woodlots. Annals of Forest Science. 77(3):1–12.

Iles, K. 2003. A sampler of inventory topics. Kim Isles & Associates Ltd., Nanimo. British Columbia, Canada.

Iles, K., and N. J. Smith. 2006. A new type of sample plot that is particularly useful for sampling small clusters of objects. Forest Science. 52(2):148–154.

Jenkins, J. C., D. C. Chojnacky, L. S. Heath, and R. A. Birdsey. 2003. National-scale biomass estimators for United States tree species. Forest science. 49(1):12–35.

Kershaw, J. A., M. J. Ducey, T. W. Beers, and Bertram. Husch. 2016. Forest mensuration. Fifth edition. John Wiley & Sons.

Ketterings, Q. M., R. Coe, M. van Noordwijk, and C. A. Palm. 2001. Reducing uncertainty in the use of allometric biomass equations for predicting above-ground tree biomass in mixed secondary forests. Forest Ecology and management. 146(1–3):199–209.

Lambert, M.-C., C.-H. Ung, and F. Raulier. 2005. Canadian national tree aboveground biomass equations. Canadian Journal of Forest Research. 35(8):1996–2018.

Lynch, T. B. 2017. Optimal plot size or point sample factor for a fixed total cost using the Fairfield Smith relation of plot size to variance. Forestry. :foresj;cpw038v1.

Lynch, T. B. 2006. Variance Reduction for Sector Sampling. Forest Science. 52(3):251–261.

Marshall, D. D., K. Iles, and J. F. Bell. 2004. Using a large-angle gauge to select trees for measurement in variable plot sampling. Can. J. For. Res. 34(4):840–845.

R Development Core Team. 2019. R: A Language and Environment for Statistical Computing. The R Foundation for Statistical Computing, c/o Institute for Statistics and Mathematics, 1020 Vienna, Austria. Available online at: https://www.r-project.org/.

Robinson, A. P., and R. E. Froese. 2004. Model validation using equivalence tests. Ecological Modelling. 176(3–4):349–358.

Smith, N. J., and K. Iles. 2012. Sector sampling—synthesis and applications. Forests. 3(1):114–126.

Smith, N. J., K. Iles, and K. Raynor. 2008. Investigation of some sector sampling statistical properties. Forest Science. 54(1):67–76.

Ung, C.-H., P. Bernier, and X.-J. Guo. 2008. Canadian national biomass equations: new parameter estimates that include British Columbia data. Can. J. For. Res. 38(5):1123–1132.

Wang, H. 2019. Estimating forest attributes from spherical images. MSc Forestry Thesis, University of New Brunswick, Fredericton, NB, Canada. Available online at: https://unbscholar.lib.unb.ca/islandora/object/unbscholar%3A10158.

Yang, T.-R., Y.-H. Hsu, J. A. Kershaw, E. McGarrigle, and Dan Kilham. 2017. Big BAF sampling in mixed species forest structures of northeastern North America: influence of count and measure BAF under cost constraints. Forestry: An International Journal of Forest Research. 90(5):649–660.

Yang, T.-R., J. A. Kershaw, A. R. Weiskittel, T. Y. Lam, and E. McGarrigle. 2019. Influence of sample selection method and estimation technique on sample size

requirements for wall-to-wall estimation of volume using airborne LiDAR. Forestry: An International Journal of Forest Research. 92(3):311–323.

Chapter 4 Use of Sector Sampling of 360 Spherical Images for Biomass Estimation

Abstract

Efficient subsampling designs reduce forest inventory costs by focusing sampling efforts on more variable forest attributes. Sector subsampling is an efficient and accurate alternative to big basal area factor (big BAF) sampling to estimate the mean basal area to biomass ratio. In this study, we apply sector subsampling of spherical images to estimate above ground biomass and compare our image-based estimates with field data collected from three early spacing trials on western Newfoundland Island. The results show that sector subsampling of spherical images produced errors of 0.3%-3.4% with only about 60 trees measured across 30 spherical images compared to about 4000 trees measured in the field. Photo-derived basal area was underestimated because of occluded trees; however, we implemented an additional level of subsampling, collecting field-based basal area counts, to correct for bias due to occluded trees. We extended Bruce's formula for standard error estimation to our three-level hierarchical subsampling scheme and showed that Bruce's formula is generalizable to any dimension of hierarchical subsampling. Spherical images are easily and quickly captured in the field using a consumer-grade 360˚ camera and sector subsampling, including all individual tree measurements, were obtained using a custom-developed python software package. The system is an efficient and accurate photo-based alternative to field-based big BAF subsampling.

Introduction

Above-ground biomass (AGB) plays a vital role in global climate change mitigation and ecosystem dynamics (Brown 1997; Mette et al. 2002; Le Toan et al. 2011), and can help in monitoring emissions of CO_2 resulting from land use and land cover changes (Sales et al. 2007). To restore, enhance and manage forest resources and create a sustainable environment (Bartuska 2006), forest attributes must be efficiently monitored (Brown 1999; Pearson et al. 2007; Chen et al. 2019). Direct measurement of biomass requires complete harvest of sample plots and drying and weighing of the different tree components (Kershaw et al. 2016). This process is destructive, time-consuming and costly, and is generally limited to a few research studies rather than used operationally. Accurate and repeatable estimates often are obtained from allometric equations applied to individual tree measurements (e.g., diameter at breast height (DBH) and height (HT)) and expanded to per unit area (Brown 2002; Lu et al. 2016); however, even this process is time-consuming and may result in large errors because relationships between species, forest ages, site conditions and equations must be considered (Telenius and Verwijst 1995; Lu 2006; Yang et al. 2017). Various indirect methods such as regression models (Baskerville 1972; Brown et al. 1989; Usoltsev and Hoffmann 1997; Montès et al. 2000), hemispherical photography (Clark and Murphy 2011) and remote sensing (Armstrong 1993; Lu 2006; Zolkos et al. 2013; Lu et al. 2016) are used for AGB estimation. However, there is no standard for determining the best estimation methods for biomass because various data sources and prediction approaches are frequently applied (Fassnacht et al. 2014), even though they can give widely varying results (e.g. MacLean et al. 2014). The most effective variables, equation forms, and

estimation approaches are not clear (Lu et al. 2016) and have not, to our knowledge, been systematically studied.

Remote sensing is an important tool for landscape level biomass estimation (Lu 2006). Light Detection and Ranging (LiDAR), either airborne (ALS) or terrestrial (TLS), scanning has shown promise for biomass estimation (Goetz et al. 2009; Gleason and Im 2011; Hayashi et al. 2015) and has become an almost ubiquitous tool in forest inventory (Dubayah and Drake 2000; Dassot et al. 2011; Hayashi et al. 2015). ALS has the capability of covering large landscapes and providing high resolution ground and canopy surface models (Gaveau and Hill 2003; Räsänen et al. 2014; Wilkes et al. 2015; Erfanifard et al. 2018), while TLS has the capability of estimating understory vegetation parameters (Hilker et al. 2010; Hopkinson et al. 2013), calibrating ALS estimates with auxiliary variables (Greaves et al. 2017) and providing forest structural information (Ducey and Astrup 2013; Astrup et al. 2014). However, LiDAR is not without its shortcomings. Occlusion of all or parts of some trees is a frequent issue with both ALS and TLS (Hilker et al. 2010; Ducey and Astrup 2013; White et al. 2016) and is a major source of uncertainty in LiDAR-assisted forest inventories (Ayrey et al. 2019). Reliance on model-assisted predictions based on data that are not probabilistic samples is another source of uncertainty (Yang et al. 2019). While ALS data are becoming increasingly freely available, terrestrial scanners remain very expensive and both data sources require field data for calibration, extensive postprocessing, model fitting, and prediction verification. In many respects, LiDAR trades off costs associated with field work with costs associated with equipment and office work.

Close-range digital photogrammetry is a cost-effective alternative to TLS (Stewart et al. 2004; Perng et al. 2018; Lu et al. 2019; Wang 2019). Several researchers have

demonstrated that high-resolution panoramic imagery is an accurate tool for collecting basic tree and forest data (Dick et al. 2010; Fastie 2010; Lu et al. 2019; Wang 2019; Wang et al. 2020). Horizontal point sampling (or angle count sampling (Bitterlich 1984; Iles 2003; Stewart et al. 2004)) is easily implemented on 360˚ panoramic images (Fastie 2010; Dick 2012). The angle required for a given basal area factor is expressed in terms of pixels and a pixel-based "gauge" is moved across the image and trees appearing larger than the gauge are counted as "in" trees (DeCourt 1956; Stewart et al. 2004; Fastie 2010; Dick 2012; Wang et al. 2020). However, occluded (hidden) trees are a problem with photo-based angle count sampling resulting in undercounts of "in" trees and, as a result, photo basal area (PBA) is underestimated (Stewart et al. 2004; Dick 2012; Wang 2019). In addition to PBA estimates, Perng et al (2018) and Lu et al (2019) demonstrated how individual tree diameters and heights can be obtained from stereographic 360˚/180˚ hemispherical images, and Wang (In Press) extended this idea to spherical images.

The newer consumer-grade 360˚ spherical cameras make photo-based angle count sampling even easier because image stitching is done onboard the camera and the two fixed fish-eye lenses minimize alignment errors (Wang 2019; Wang et al. 2020). Dai (In Preparation, Chapter 2) compared biomass estimation models based on PBA derived from spherical images obtained using a Ricoh Theta S 360° camera (Ricoh Imaging Company, LTD 2016) to models based on common TLS metrics. Errors for models based on TLS metrics ranged from 20% – 33% while errors for models derived from PBA estimates ranged from 17% - 21%. Given the low cost, portable size, and field efficiency, the spherical camera offers much promise as a forest inventory tool (Dai et al. In Press; Wang et al. 2020).

Model-derived estimation requires calibration for every new application. Efficient sample-derived estimation may be an effective alternative to model-derived estimation (Yang et al. 2019). Big BAF sampling is a widely used subsampling design that utilizes a small angle gauge to count "in" trees and estimate basal area per ha (BA; m^2ha^{-1}) for each sample point; and a larger angle gauge to select trees to measure (Iles 2003; Marshall et al. 2004; Yang et al. 2017). The ratio of the tree attribute of interest to individual tree BA (XBAR) calculated from the measure-trees and the mean BA are used to calculate the per unit area estimates of the attribute of interest. However, implementing big BAF sampling on spherical photos is challenging, since big BAF sampling tends to select trees that are very close to the sample point. On spherical images, these trees are often very distorted, or it is very difficult to clearly identify the tree tip which make tree height harder to measure accurately (Wang et al. In Press). An effective subsampling protocol for spherical image sampling requires an alternative measure-tree selection process.

Dai et al. (In Press) showed that sector subsampling is a viable alternative measure-tree selection method to big BAF sampling with less than 1% difference in means and nearly equivalent errors for a given measure-tree subsample intensity (i.e., number of trees). Sector sampling (Smith et al. 2008; Smith and Iles 2012) uses sectors of a circle to define sample plots. Originally designed to efficiently sample small or irregular forest areas (Smith et al. 2008; Smith and Iles 2012), Dai et al. (In Press) applied sectors as a means to select subsamples of trees for detailed measurement. As formulated by Dai et al. (In Press), sector subsampling uses a small angle gauge and horizontal point sampling to select count trees to estimate BA and then a randomly oriented sector to select trees to measure. Two variants of sector subsampling were developed. The first method, termed SectorIN, used a

randomly oriented sector to subsample the “in” trees selected using the small gauge. All “in” trees that fell within the sector were sampled as measure trees. The second method, termed SectorDST, used a randomly oriented sector to subsample trees within a predefined distance for measurement. In this case, measure-trees could be both “in” trees and other trees that fall within the predefined sector. Like big BAF sampling, the measure trees are used to estimate the ratio of the tree attribute of interest to tree basal area, and the mean ratio is multiplied by average BA to estimate the per ha average of the attribute of interest. In this paper, we couple photo point sampling (Stewart et al. 2004; Fastie 2010; Dick 2012; Wang et al. 2020) with sector subsampling (Dai et al. In Press) to develop an efficient method for sample-derived estimation of area-based AGB using spherical images. The specific objectives of this study were: 1) apply sector subsample selection to PBA plots obtained from spherical images; 2) develop a hierarchical approach to subsampling from photos that includes correction for occluded trees and 3) generalize Bruce’s formula (Goodman 1960) for multiple subsample levels.

Methods

Study sites

In this study, data from western Newfoundland Island (NL), Canada were used. These data came from three early spacing trials established in the early 1980s by the government of Newfoundland and Labrador in cooperation with the Canadian Forest Service (Donnelly et al. 1986) (Figure 4. 1). Balsam fir (*Abies balsamea* L.) was the dominant species with minor components of black spruce (*Picea mariana* (Mill.) Britton, Sterns & Poggenb.) and white birch (*Betula papyrifera* Marshall). There were 5 spacing treatments: control/no

spacing (S00), 1.2m spacing (S12), 1.8m spacing (S18), 2.4m spacing (S24) and 3.0m spacing (S30). The treatments were arranged in a randomized complete block design with 3 blocks per trial (45 sample units were used in this study). Each treatment was applied to a 0.25 ha area (50m × 50m), and a circular permanent sample plot (PSP) was established near the center of each 0.25 ha area. The PSP size varied such that there were approximately 100 trees per plot at the time of establishment. Only the most recent measurements for each trial were used in this study.

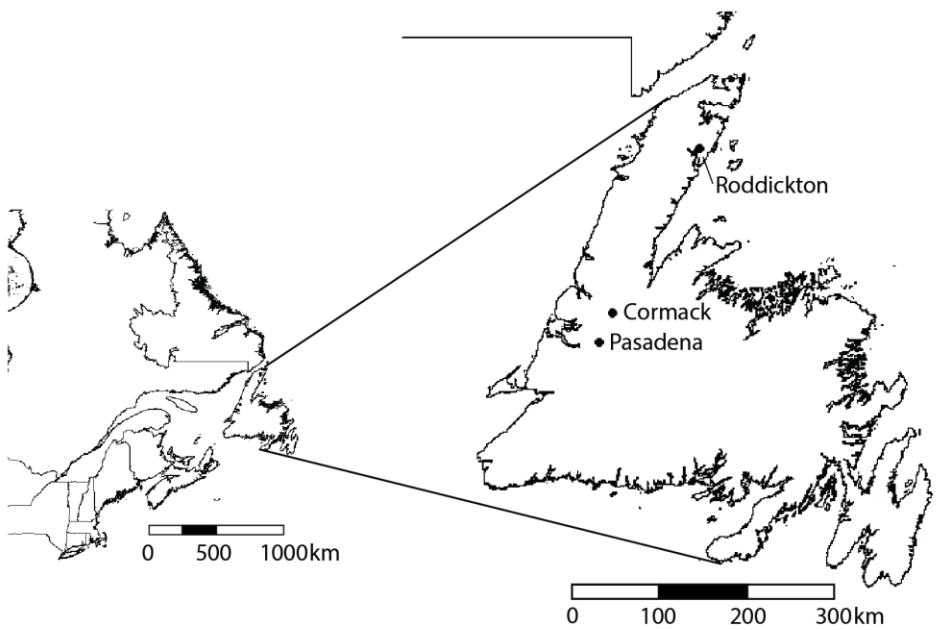

Figure 4. 1 Location of Newfoundland in Atlantic Canada and locations of 3 early spacing trials on Newfoundland Island.

Field Biomass Estimation

Individual tree biomass was estimated using the Canadian National Biomass equations (Lambert et al. 2005). We used Eq. 3 from Table 4. 4 in Lambert et al. (2005) which included both DBH and HT. Total tree biomass (BM_i; kg) was obtained by summing the separate component biomass estimates (wood, bark, branches, and foliage). Field biomass per ha (FBM; tonnes·ha^{-1}) for each spacing PSP was obtained by summing the individual tree biomass estimates multiplied by the plot expansion factor (ExpF) and divided by 1000 kg per tonne:

$$\mathrm{FBM} = \frac{\mathrm{ExpF}}{1000} \times \sum_{i=1}^{n} \mathrm{BM}_i \qquad (1)$$

where n = the number of field measure trees on each PSP.

Sector Subsampling of Spherical Images

A Ricoh Theta S 360° camera (Ricoh Imaging Company, LTD 2016) was used to obtain spherical images of the NL spacing trial PSPs. We obtained images in 3 locations on each PSP. The images were obtained at half the plot radius of each PSP at azimuths of 0˚ (360˚), 120˚, and 240˚. At each image acquisition location, spherical images were obtained at heights of 1.6m and 2.6m using a tripod-stabilized height pole (Wang et al. In Press)

In Dai et al. (In Press), sector subsampling intensity was defined in terms of the angular percentage of the 360˚s azimuth subsampled (Figure 4. 2a). The software developed by Wang et al. (In Press) was modified to randomly select a sector of a specified intensity by randomly generating an azimuth and superimposing parallel vertical lines on the cylindrically projected images based on sector intensity (Figure 4. 2b) with the inclusion

region centered on the randomly generated azimuth (in cylindrical projections, fixed horizontal angles are of fixed image width, thus the vertical parallel lines project the specified sector angle onto the cylindrical image; Figure 4. 2b).

In our first simulation experiment, a modified SectorDST sampling method (Dai et al. In Press) was implemented on each photo pair at each image acquisition location within each PSP (3 locations per PSP were used in this study) across the three spacing trials to select measure-trees to determine the biomass to individual tree basal area ratio (BBAR; $kg \cdot m^2$). Photo basal area (PBA, m^2ha^{-1}) was estimated from the spherical images (1.6m height of the tree) using the software developed by Wang et al. (2020) and a 2 M BAF (i.e., each count tree represents 2 m^2ha^{-1} of basal area). Mean PBA for each PSP was estimated using:

$$\overline{\mathrm{PBA}} = \frac{\sum_{i=1}^{p} \mathrm{PBA_i}}{p} = \frac{\sum_{i=1}^{p} \mathrm{BAF} \times \mathrm{Count_i}}{p} \qquad (2)$$

where p = the number of image acquisition locations (3 in the study).

The SectorDST selection method, as developed in Dai et al. (In Press), selects measure-trees within a randomly oriented sector within a predetermined distance from the sample point (Figure 4. 2a). For the spherical images, tree occlusion is an issue, so instead of selecting all trees within a given distance, we chose all trees within a sector that were clearly visible (Figure 4. 2b). All visible trees were measured on the spherical image pairs using the stereographic methods described by Wang et al. (In Press) as implemented in the modified software.

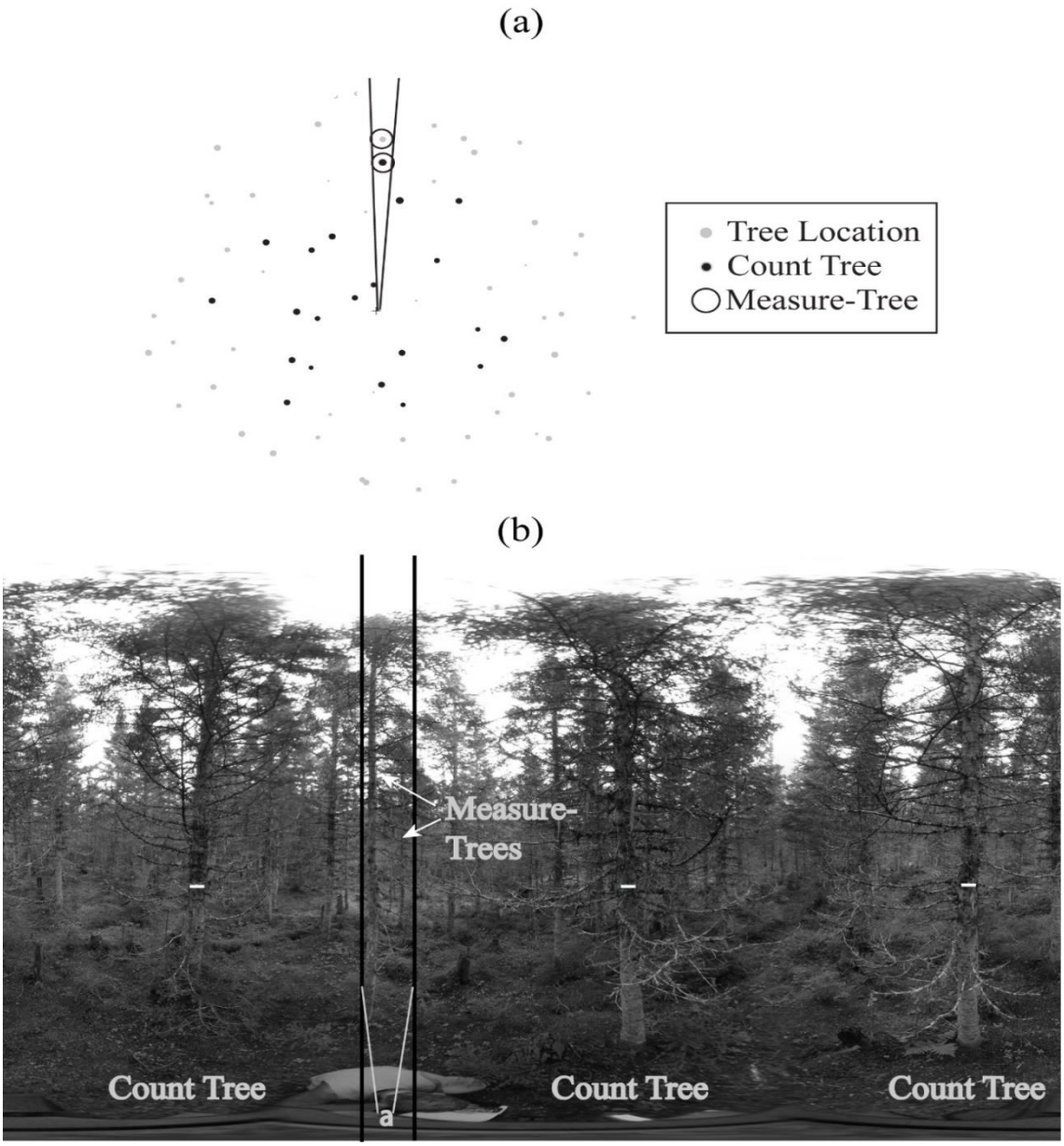

Figure 4. 2 SectorDST subsampling as viewed: (a) from a map perspective of a photo sample plot; and (b) as viewed from a cylindrically projected spherical image. (BAF count trees are identified by horizontal white bars; measure trees are those trees within the two vertical black lines defined by sector angle "a")

Tree basal area and tree biomass were calculated using the same methods described above for the field estimates (assuming all trees were balsam fir for biomass estimation) and mean BBAR ($\overline{\mathrm{BBAR}}$) was calculated using a ratio of means approach (Dai et al. In Press):

$$\overline{\mathrm{BBAR}} = \frac{\sum_{i=1}^{m} \mathrm{BM_i}}{\sum_{i=1}^{m} \mathrm{BA_i}} = \frac{\sum_{i=1}^{m} \mathrm{BM_i}}{\sum_{i=1}^{m} 0.00007854 \times (\mathrm{DBH_i})^2} \quad (3)$$

where m = the number of measure trees. Mean photo biomass per ha (PBM, tonnes·ha^{-1}) was then estimated using:

$$\overline{\mathrm{PBM}} = \frac{\overline{\mathrm{BBAR}} \times \overline{\mathrm{PBA}}}{1000} \quad (4)$$

Percent standard error for $\overline{\mathrm{PBM}}$ was estimated using Bruce's formula (Goodman 1960; Marshall et al. 2004):

$$\%\mathrm{se}(\overline{\mathrm{PBM}}) = \sqrt{\%\mathrm{se}(\overline{\mathrm{PBA}})^2 + \%\mathrm{se}(\overline{\mathrm{BBAR}})^2} \quad (5)$$

where %se() = the standard error as a percent of the mean. Although Bruce's formula assumes independence of the error components, simulations show that it performs well in comparison with more complicated formulations (Gove et al. 2020). For $\%\mathrm{se}(\overline{\mathrm{PBA}})$, we used the formula for standard error (se) under simple random sampling (Zar 1999):

$$\mathrm{se} = \sqrt{\frac{\sum \mathrm{BA}^2 - (\sum \mathrm{BA})^2/\mathrm{k}}{\mathrm{k}(\mathrm{k}-1)}} \quad (6)$$

where k = the number of sample plots. For $\%\mathrm{se}(\overline{\mathrm{BBAR}})$, we used the formulation provided in Kershaw et al. (2016 p. 348):

$$\%\mathrm{se}(\overline{\mathrm{BBAR}}) = \sqrt{\left(\frac{\overline{\mathrm{BBAR}}^2}{\mathrm{m}(\mathrm{m}-1)}\right)\left(\frac{\sum \mathrm{PBM}^2}{\overline{\mathrm{PBM}}^2} + \frac{\sum \mathrm{BA}^2}{\overline{\mathrm{BA}}^2} - \frac{2\sum \mathrm{PBM}\cdot\mathrm{BA}}{\overline{\mathrm{PBM}}\cdot\overline{\mathrm{BA}}}\right)} \quad (7)$$

where PBM and $\overline{\mathrm{PBM}}$ were the individual measure-tree biomass estimates and mean measure-tree biomass estimates; BA and $\overline{\mathrm{BA}}$ were the individual measure-tree stem basal areas (estimated from DBH measures triangulated from the 1.6m and 2.6m images) and

mean measure-tree stem basal area; and $\overline{\mathrm{BBAR}}$ was the mean biomass to basal area ratio of the measure-trees from eq. 3.

The SectorDST sampling procedure was implemented on each spherical image pair at each image acquisition point on each spacing PSP on each replicate across the three spacing trials (3 trials×5 treatments×3 blocks×3 locations = 135 image acquisition point). All analyses were conducted in the R Statistical Language (R Development Core Team 2019).

Occluded Tree Correction

One sampling issue with using PBA is tree occlusion (Dick 2012). On photo plots, it is not possible to move from the sample point to check for occluded (hidden) trees. Occluded trees result in under–counting of "in" trees and negative biases in BA estimates. To explore the potential of using a subsample of in-field tree counts to correct for PBA bias, we implemented a simulation study using the spherical image results from the previous section and a subsmaple of field basal area (FBA) counts. We explored field BA: photo BA correction (field to photo basal area ratio, FPBAR) by randomly selecting 5, 10, 15, or 20 plots to obtain FBA measures. A second ratio of means estimator was obtained to correct PBA using the subsampled field BAs:

$$\overline{\mathrm{FPBAR}} = \frac{\sum_{i=1}^{j} \mathrm{FBA_i}}{\sum_{i=1}^{j} \mathrm{PBA_i}} \tag{8}$$

where, $\overline{\mathrm{FPBAR}}$ was the mean of field BA to PBA ratio, j = the number of field plots used for correcting PBA (5, 10, 15, 20 in this study). and the corrected biomass estimate ($\overline{\mathrm{CBM}}$) became:

$$\overline{\mathrm{CBM}} = \overline{\mathrm{FPBAR}} \cdot \overline{\mathrm{PBA}} \cdot \overline{\mathrm{BBAR}} \tag{9}$$

We further propose to extend Bruce's formula to include this third source of sampling error:

$$\%\mathrm{se}(\overline{\mathrm{CBM}}) = \sqrt{\%\mathrm{se}(\overline{\mathrm{FPBAR}})^2 + \%\mathrm{se}(\overline{\mathrm{BBAR}})^2 + \%\mathrm{se}(\overline{\mathrm{PBA}})^2} \qquad (10)$$

where $\%\mathrm{se}(\overline{\mathrm{FPBAR}})$ was estimated using eq. 4. Derivation of eq. 10 is given in the Appendix. To assess the validity of this extension, we used coverage based on nominal 95% confidence intervals and the correlations between the sources of errors. All simulations were repeated 100 times for estimation comparisons, and 1000 times for assessing coverage of nominal confidence intervals.

Results

Using a sector intensity of 2% (7.2˚ of the full 360º), 163 photo measure-trees were selected across the 135 image acquisition points (3 points per PSP) over the 45 spacing trial PSPs. BBAR averaged 3214 $kg{\cdot}m^{-2}$ with a standard error of 30.7 $kg{\cdot}m^{-2}$. PBA averaged 34.3 m^2ha^{-1} with a standard error of 1.8 m^2ha^{-1}. The resulting mean biomass was 110.3 $kg{\cdot}ha^{-1}$ with a standard error of 5.4 $kg{\cdot}ha^{-1}$ (Table 4. 1). PBM was underestimated relative to FBM on all but two of the 45 spacing trial plots (Figure 4. 3).

While underestimation of biomass was evident in the sector subsampling, the lowess smoothing line (Cleveland 1981) indicated a relatively strong linear relationship that could be corrected using ratio estimation (Figure 4. 3). Based on 100 repeated simulation samples using 1 image acquisition point per spacing PSP and a random subsample of field basal area to correct photo basal area, the underestimation associated with PBA was efficiently corrected (Figure 4. 3; Table 4. 1). As few as 5 field plots were sufficient to correct the $\overline{\mathrm{PBM}}$ underestimation that resulted from occluded trees in the PBA estimates (Table 4. 1).

With 10 field samples, standard errors (Table 4. 1) were comparable to those obtained using the regression estimates of $\overline{\mathrm{BM}}$ developed in Dai (In Preparation Chapter 2), and with 20 subsamples, the standard errors were nearly equivalent to those obtained for the complete field data from the 45 spacing plots with all trees measured for HT and DBH (Table 4. 1). The 45 plots across the 3 spacing trials had 4181 trees measured with a standard error of 7.3 tonnes·ha^{-1}. In our simulations presented in Figure 4. 3 and Table 4. 1, there were on average 54 trees subsampled across the 45 randomly sampled spacing trial plots with an average standard error of 10.3 tonnes·ha^{-1}.

The addition of subsampling field PSPs for BA estimation and ratio correction added another source of error associated with our estimate of biomass. As expressed in eq. 10, we proposed to expand Bruce's formula by adding a third component to the error formulation. Bruce's method relies on independence of the component errors (Goodman 1960). As shown in Figure 4. 4, correlations between the error components were quite low. The highest correlation was 0.16 (r^2 = .03) for $\%\mathrm{se}(\overline{\mathrm{PBA}})$ versus $\%\mathrm{se}(\overline{\mathrm{FPBAR}})$while the other two correlations were less than 0.10 (Figure 4. 4). We expanded our number of simulations to 1000 and assessed coverage (number of 95% confidence intervals containing the true mean) by field sample size. For 5 field BA samples, coverage was 93.7%, for 10 field BA samples, 98.6%, for 15 field BA samples, 99.5%, and for 20 field BA samples, 99.9% (Table 2).

Table 4. 1 Means, standard errors of biomass (tonnes·ha^{-1}) under field measured, TLS predictions, PBA predictions, corrected/uncorrected sector predictions and corrected ratios (range in bracket) under 5, 10, 15, 20 sample sizes in sector subsampling for Newfoundland (NL) spacing trials. (The corrected ratios were determined by the ratio of plot BA divided by PBA under different samples sizes)

Source	Correction Ratio		Biomass Estimate	
Sample Size	Mean	Standard	Mean	Standard
Field Measured			148.9	7.3
TLS Prediction			148.8	17.2
PBA Prediction			149.3	19.9
Sector				
Subsampling				
Uncorrected			102.9	5.4
5	1.44	0.29	148.5	30.1
	{0.93, 2.35}		{95.5, 241.7}	
10	1.42	0.19	146.4	19.7
	{1.03, 1.86}		{105.8, 191.4}	
15	1.40	0.13	144	13.2
	{1.06, 1.66}		{108.8, 171.2}	
20	1.4	0.1	143.9	10.3
	{1.18, 1.60}		{121.9, 163.5}	

Table 4. 2 Comparison of standard error for simulated PBA (m^2), BBARs ($kg \cdot m^{-2}$), field to photo BA ratio, simulated biomass ($tonnes \cdot ha^{-1}$) across 5, 10, 15, 20 field sample sizes for the western Newfoundland (NL) spacing trials. Biomass ($tonnes \cdot ha^{-1}$), coverage (number of 95% confidence intervals containing the true mean) and correspond correlations were also presented by field sample sizes.

Factor	Field Sample Size			
	5	10	15	20
sePBA	7.08	7.08	7.03	7.07
seBBAR	1.97	1.96	1.95	1.99
seFPBArat	20.19	14.39	12.19	10.56
seBM	21.66	16.24	14.25	12.90
BM	157	156	155	155
Coverage	94.70	98.50	99.50	99.90
cor(PBA vs FPBAratio)	0.16	0.23	0.30	0.46
cor(PBA vs BBAR)	0.00	0.05	0.04	0.08
cor(BBAR vs FPBAratio)	0.05	0.01	0.04	0.05

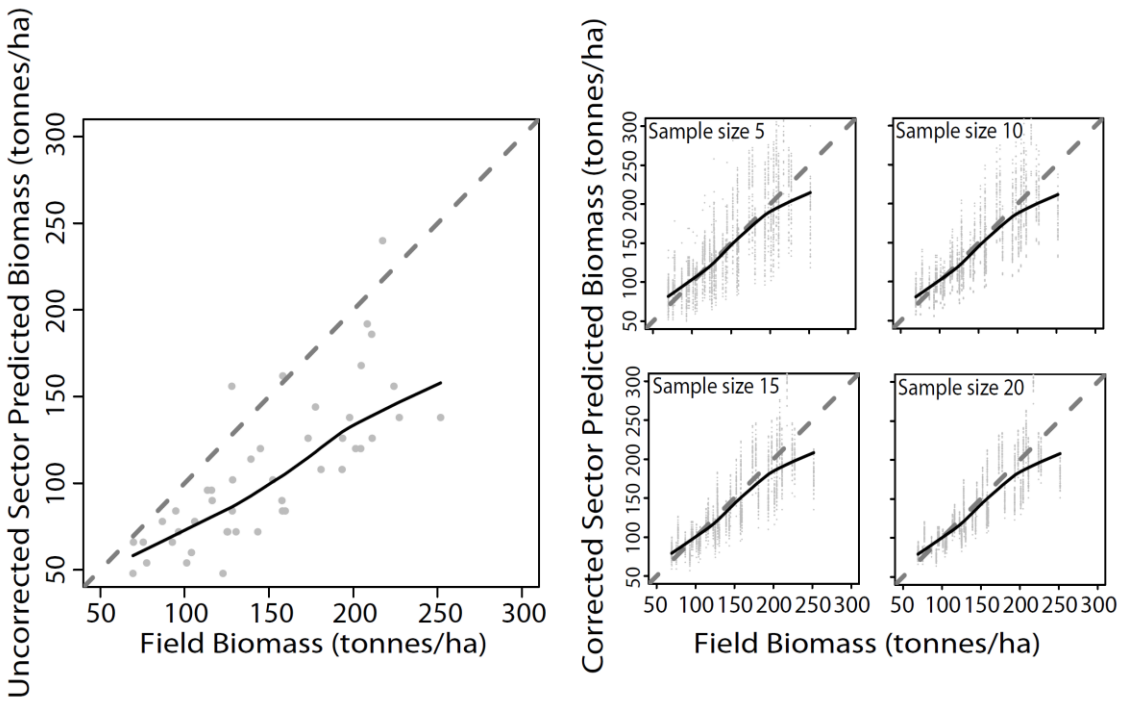

Figure 4. 3 Comparison between corrected/uncorrected sector prediction with field measured biomass under 4 different sample sizes 5, 10, 15, 20 for Newfoundland (NL) spacing trials.

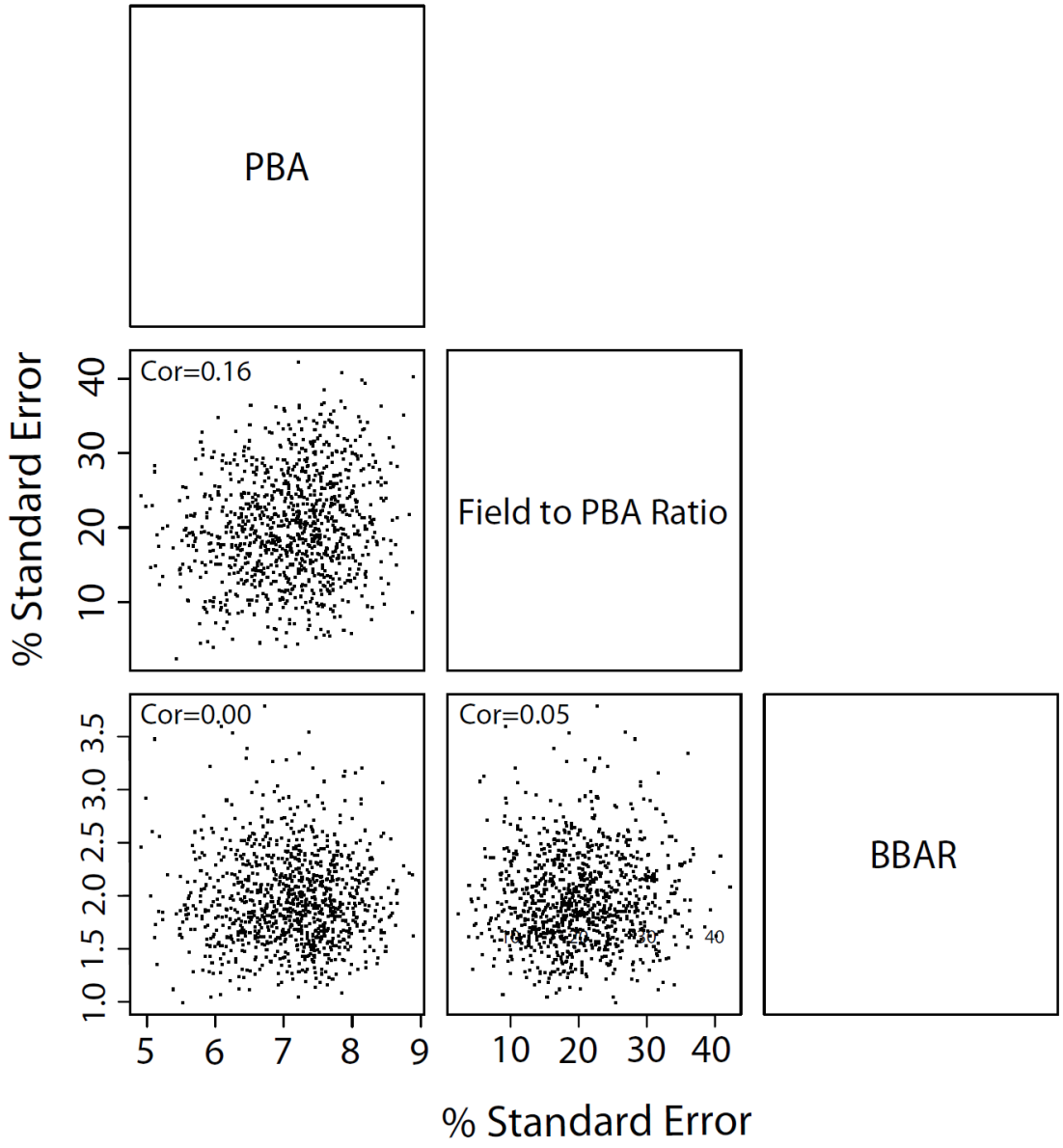

Figure 4. 4 Comparison between standard errors generated from field BA and standard errors from PBA (Chapter 2) and BBAR for Newfoundland (NL) spacing trials. (BBARs were extracted from the software developed by Wang et al. (2020) by using SectorDST sample selection method)

Discussion and Conclusions

While selection of measure-trees did not produce biases, the underestimation of basal area from the spherical images (PBA) resulted in serious underestimation of biomass (Table 4. 1, Figure 4. 3). Occlusion issues with panoramic photo sampling were identified in several previous studies (Fastie 2010; Dick 2012; Lu et al. 2019). In the field, occluded trees can be identified and correctly counted using a number of techniques including moving from plot center to actually measuring distances and DBHs to determine if trees are in or out of the count sample (Kershaw et al. 2016). With panoramic or spherical images, it is not possible to move around and only visible trees can be counted and/or measured. Our use of a third-stage subsample to collect field plots to correct for occluded trees was an effective and efficient sampling procedure to correct PBA to account for occluded trees (Figure 4. 3; Table 4. 1). Based on the resulting correction ratios for field: photo BA (FPBAR, Table 4. 4), about 70% of the "in" trees were identified on the spherical images. This is consistent with the results from Dick (2012) who reported 60% - 90% of trees correctly counted depending on the BAF used and stand density. In this study, we used 3 image acquisition points offset from plot center and averaged across the three photo samples. Wang et al. (2019) found this to be an effective strategy for reducing occlusion bias, but that was not the case here, even though some of the spherical images were in common.

As few as 5 field counts were sufficient to correct the underestimation; however, the resulting standard errors were quite large (Table 4. 1). The percent standard errors associated with FPBAR were, in general, quite large relative to the percent standard errors for the other components (PBA and BBAR versus FPBAR; Table 4. 2). At 10 field samples,

the resulting standard errors were comparable to the standard errors obtained using model assisted approaches (Dai In Preparation). With 20 subsamples, the standard errors were only about double the full field sample data. The full field samples required over 4000 trees be measured for DBH and HT, our procedure only required about 60 trees be measured.

Subsampling with ratio estimation is, in general, a very efficient method for correcting bias, reducing sample sizes, and focusing sampling efforts on the level where variation is greatest (Iles 2003; Yang et al. 2019; Hsu et al. 2020). In this study, we used simple random selection of field subsamples. Yang et al. (2019) showed that simple random sampling was as efficient and in some cases more efficient than variable probability selection methods for LiDAR assisted ratio estimation when sample sizes were small. Hsu et al. (2020) and Yang et al. (2019) showed that list sampling was the most effective variable probability selection approach for ratio estimation. List sampling requires prior knowledge of the covariate for all sample units (Kershaw et al. 2016). Both Hsu et al. (2020) and Yang et al. (2019) showed the sampling with probability proportional to prediction (3P) could also be effectively used. Hsu (2019) developed methods for implementing 3P sampling using spherical images. A variable probability approach most likely would improve the results presented here.

Comparing our estimated standard errors for single replicated simulated samples to the standard deviations of the means across all samples, our extension of Bruce's formula to three dimensions appears reasonable. Coverage, based on 95% confidence intervals, seem to also support this extension. Bruce's formula relies on the independence of errors among the hierarchical components of the sample (Goodman 1960). As shown in Figure 3, the assumptions of independence appear to be met in this case, consistent with the observations

of Gove et al. (2020) and Lynch et al. (2020) that Bruce's formula provides adequate confidence interval coverage in simulations for ordinary big BAF sampling.

To make appropriate management decisions, foresters require accurate and timely data (Kershaw et al. 2016). An efficient sample design can, not only reduce costs and save time, but also provide accurate estimates (Lynch 2017; Yang et al. 2017; Chen et al. 2019). In this study, we applied an alternative subsampling procedure using sectors to select measure-trees and coupled this with a hierarchal sampling scheme that combines spherical image measurements with horizontal point sample counts to estimate biomass in three spacing trials in western Newfoundland. Our results show that this approach is efficient and accurate and can be used to estimate biomass at a much lower costs than more expensive sources such as terrestrial LiDAR.

Appendix

As an estimator of the standard error of $\overline{\mathrm{CBM}}$, we have suggested eq. 10, i.e.

$$\%\mathrm{se}(\overline{\mathrm{CBM}}) = \sqrt{\%\mathrm{se}(\overline{\mathrm{FPBAR}})^2 + \%\mathrm{se}(\overline{\mathrm{BBAR}})^2 + \%\mathrm{se}(\overline{\mathrm{PBA}})^2}$$

This estimator can be viewed as a direct extension of Bruce's method, and derived using the Delta method following the general approach of Gove et al. (2020). Let $\mathbf{x}$ be a vector of random variables x_i, $i = 1 \ldots n$, each having mean θ_i (i.e., a vector of means $\boldsymbol{\theta}$). Then, for any continuous function of $\mathbf{x}$, say $g(\mathbf{x})$, we may write its Taylor series expansion as

$$g(x) = g(\theta) + \sum_{i=1}^{n} (x_i - \theta_i) \frac{\delta g}{\delta x_i} + \sum_{i=1}^{n} \sum_{j=1}^{n} \frac{(x_i - \theta_i)(x_j - \theta_j)}{2!} \cdot \frac{\delta^2 g}{\delta x_i \delta x_j} + \cdots$$

where the partial derivatives are all evaluated at $x = \theta$. The Taylor series continues to third- and higher-order terms that are not shown here, as they will be neglected below. In our case, we have three random variables: $x_1 = \overline{FPBAR}$, $x_2 = \overline{BBAR}$, and $x_3 = \overline{PBA}$, which we use to calculate $g(x) = \overline{BM/ha}$ (Eq. 9). Following Seber (1982) and Gove et al. (2020), we assume all three variables are estimated with negligible bias.

Now, the variance of $g(x)$ is

$$\mathrm{var}\big(g(x)\big) = E\left[\big(g(x) - g(\theta)\big)^2\right]$$

Neglecting the second-order and higher terms in the Taylor series expansion, and rearranging, gives

$$\mathrm{var}\big(g(x)\big) = E\left[\left(\sum_{i=1}^{n}(x_i - \theta_i)\frac{\delta g}{\delta x_i}\right)^2\right]$$

where, as before, the partial derivatives are evaluated at $x = \theta$. Following some substitution and algebraic rearrangement, Gove et al. (2020) show

$$\mathrm{var}\big(g(x)\big) = \sum_{i=1}^{n}\mathrm{var}(x_i)\left(\frac{\delta g}{\delta x_i}\right)^2 + 2\sum_{i<j}\sum \mathrm{cov}\big(x_i, x_j\big)\left(\frac{\delta g}{\delta x_i}\right)\left(\frac{\delta g}{\delta x_j}\right)$$

Note that if we assume the x_i are independent, the covariance terms may be dropped; otherwise, they should be retained to provide a more exact expression for the variance. In practice, we do not know the population values of θ or $\mathrm{var}(x_I)$, so we form a drop-in estimator by substituting the observed values of x and the unbiased estimators $\widehat{\mathrm{var}(x_i)}$. Note further that in our case, where $g(x)$ is a simple product of the random variables,

$$\frac{\delta g}{\delta x_i} = \frac{1}{x_i}\prod_{i=1}^{n} x_i = \frac{g(x)}{x_i}$$

Dropping the covariance terms, and substituting, we obtain

$$\mathrm{var}\big(q(x)\big) = g(x)^2 \sum_{i=1}^{n} \frac{\mathrm{var}(x_i)}{x_i^2}$$

$$\frac{\mathrm{var}\big(g(x)\big)}{g(x)^2} = \sum_{i=1}^{n} \frac{\mathrm{var}(x_i)}{x_i^2}$$

and since

$$\%\mathrm{se}(y) = 100\frac{\sqrt{\mathrm{var}(y)}}{y}$$

it follows immediately that

$$\%\mathrm{se}\big(g(x)\big) = \sqrt{\sum_{i=1}^{n} \%\mathrm{se}(x_i)^2}$$

which can be seen to be the general, *n*-dimensional analog to Bruce's formula. In our case, this last formula is just the standard error estimator presented in eq. 10 for n = 3.

References

Armstrong, R. A. 1993. Remote sensing of submerged vegetation canopies for biomass estimation. International Journal of Remote Sensing. 14(3):621–627.

Astrup, R., M. J. Ducey, A. Granhus, T. Ritter, and N. von Lüpke. 2014. Approaches for estimating stand-level volume using terrestrial laser scanning in a single-scan mode. Can. J. For. Res. 44(6):666–676.

Ayrey, E., D. J. Hayes, S. Fraver, J. A. Kershaw, and A. R. Weiskittel. 2019. Ecologically-Based Metrics for Assessing Structure in Developing Area-Based, Enhanced Forest Inventories from LiDAR. Canadian Journal of Remote Sensing. 45(1):88–112.

Bartuska, A. 2006. Why biomass is important: The role of the USDA forest service in managing and using biomass for energy and other uses. Research & Development, USDA Forest Service. 1–16 p.

Baskerville, G. 1972. Use of logarithmic regression in the estimation of plant biomass. Canadian Journal of Forest Research. 2(1):49–53.

Bitterlich, W. 1984. The relascope idea. Relative measurements in forestry. Commonwealth Agricultural Bureaux.

Brown, S. 1997. Estimating biomass and biomass change of tropical forests: a primer. Food & Agriculture Org.

Brown, S. 1999. Guidelines for inventorying and monitoring carbon offsets in forest-based projects. Winrock International for the World Bank. Arlington, VA, USA.

Brown, S. 2002. Measuring, monitoring, and verification of carbon benefits for forest–based projects Swingland, I.R., E.C. Bettelheim, J. Grace, G.T. Prance, and L.S.

Saunders (eds.). Philosophical Transactions of the Royal Society of London. Series A: Mathematical, Physical and Engineering Sciences. 360(1797):1669–1683.

Brown, S., A. J. Gillespie, and A. E. Lugo. 1989. Biomass estimation methods for tropical forests with applications to forest inventory data. Forest science. 35(4):881–902.

Chen, Y., T.-R. Yang, Y.-H. Hsu, J. A. Kershaw, and D. Prest. 2019. Application of big BAF sampling for estimating carbon on small woodlots. For. Ecosyst. 6(1):13.

Clark, J., and G. Murphy. 2011. Estimating forest biomass components with hemispherical photography for Douglas-fir stands in northwest Oregon. Can. J. For. Res. 41(5):1060–1074.

Cleveland, W. S. 1981. LOWESS: A program for smoothing scatterplots by robust locally weighted regression. American Statistician. 35(1):54.

Dai, X. In Preparation. Novel Methods for Estimating Above Ground Biomass.

Dai, X., H. Wang, M. J. Ducey, and J. A. Kershaw Jr. In Press. Sector Subsampling for Basal Area Ratio Estimation: An Alternative to Big BAF Sampling. Canadian Journal of Forest Research.

Dai, X., T.-R. Yang, and J. A. Kershaw Jr. In Review. Comparison of Biomass Estimation using Spherical Images versus Terrestrial LiDAR Scanning in eastern North America. Forest Ecosystems.

Dassot, M., T. Constant, and M. Fournier. 2011. The use of terrestrial LiDAR technology in forest science: application fields, benefits and challenges. Annals of Forest Science. 68(5):959–974.

DeCourt, N. 1956. Utilisation de la photographie pour mesurer les surfaces terrières (The use of photography for measuring basal area). Rev. For. Fr. 8(7):505–507. 7th ed. Rev. For. Fr. 505–507 p.

Dick, A. R. 2012. Forest inventory using a camera: Concept, field implementation and instrument development.

Dick, A. R., J. A. Kershaw, and D. A. MacLean. 2010. Spatial Tree Mapping Using Photography. Northern Journal of Applied Forestry. 27(2):68–74.

Donnelly, J. G., M. B. Lavigne, and R. S. van Nostrand. 1986. Precommercial Thinning Spacing Trials Established Between 1979 and 1985. Newfoundland Forestry Centre, St. John's, Newfoundland.

Dubayah, R. O., and J. B. Drake. 2000. Lidar remote sensing for forestry. Journal of Forestry. 98(6):44–46.

Ducey, M. J., and R. Astrup. 2013. Adjusting for nondetection in forest inventories derived from terrestrial laser scanning. Canadian Journal of Remote Sensing. 39(5):410–425.

Erfanifard, Y., K. Stereńczak, B. Kraszewski, and A. Kamińska. 2018. Development of a robust canopy height model derived from ALS point clouds for predicting individual crown attributes at the species level. International journal of remote sensing. 39(23):9206–9227.

Fassnacht, F. E., F. Hartig, H. Latifi, C. Berger, J. Hernández, P. Corvalán, and B. Koch. 2014. Importance of sample size, data type and prediction method for remote sensing-based estimations of aboveground forest biomass. Remote Sensing of Environment. 154:102–114.

Fastie, C. L. 2010. Estimating stand basal area from forest panoramas. In Proceedings of the Fine International Conference on Gigapixel Imaging for Science. :1.

Gaveau, D. L., and R. A. Hill. 2003. Quantifying canopy height underestimation by laser pulse penetration in small-footprint airborne laser scanning data. Canadian Journal of Remote Sensing. 29(5):650–657.

Gleason, C. J., and J. Im. 2011. A review of remote sensing of forest biomass and biofuel: options for small-area applications. GIScience & Remote Sensing. 48(2):141–170.

Goetz, S. J., A. Baccini, N. T. Laporte, T. Johns, W. Walker, J. Kellndorfer, R. A. Houghton, and M. Sun. 2009. Mapping and monitoring carbon stocks with satellite observations: a comparison of methods. Carbon balance and management. 4(1):2.

Goodman, L. A. 1960. On the exact variance of products. Journal of the American statistical association. 55(292):708–713.

Gove, J. H., T. G. Gregoire, M. J. Ducey, and T. B. Lynch. 2020. A note on the estimation of variance for big BAF sampling. For. Ecosyst. 7(1):62.

Greaves, H. E., L. A. Vierling, J. U. H. Eitel, N. T. Boelman, T. S. Magney, C. M. Prager, and K. L. Griffin. 2017. Applying terrestrial lidar for evaluation and calibration of airborne lidar-derived shrub biomass estimates in Arctic tundra. Remote Sensing Letters. 8(2):175–184.

Hayashi, R., J. A. Kershaw, and A. Weiskittel. 2015. Evaluation of alternative methods for using LiDAR to predict aboveground biomass in mixed species and structurally complex forests in northeastern North America. MCFNS. 7(2):49–65.

Hilker, T., M. van Leeuwen, N. C. Coops, M. A. Wulder, G. J. Newnham, D. L. B. Jupp, and D. S. Culvenor. 2010. Comparing canopy metrics derived from terrestrial and airborne laser scanning in a Douglas-fir dominated forest stand. Trees. 24(5):819–832.

Hopkinson, C., J. Lovell, L. Chasmer, D. Jupp, N. Kljun, and E. van Gorsel. 2013. Integrating terrestrial and airborne lidar to calibrate a 3D canopy model of effective leaf area index. Remote Sensing of Environment. 136:301–314.

Hsu, Y.-H. 2019. Applications of variable probability sampling using remotely sensed covariates. MSc Forestry Thesis, University of New Brunswick, Fredericton, NB, Canada. Available online at: https://unbscholar.lib.unb.ca/islandora/object/unbscholar%3A9861.

Hsu, Y.-H., Y. Chen, T.-R. Yang, J. A. Kershaw, and M. J. Ducey. 2020. Sample strategies for bias correction of regional LiDAR-assisted forest inventory Estimates on small woodlots. Annals of Forest Science. 77(3):1–12.

Iles, K. 2003. A sampler of inventory topics. Kim Isles & Associates Ltd., Nanimo. British Columbia, Canada.

Kershaw, J. A., M. J. Ducey, T. W. Beers, and Bertram. Husch. 2016. Forest mensuration. Fifth edition. John Wiley & Sons.

Lambert, M.-C., C.-H. Ung, and F. Raulier. 2005. Canadian national tree aboveground biomass equations. Canadian Journal of Forest Research. 35(8):1996–2018.

Le Toan, T., S. Quegan, M. W. J. Davidson, H. Balzter, P. Paillou, K. Papathanassiou, S. Plummer, et al. 2011. The BIOMASS mission: Mapping global forest biomass to

better understand the terrestrial carbon cycle. Remote Sensing of Environment. 115(11):2850–2860.

Lu, D. 2006. The potential and challenge of remote sensing-based biomass estimation. International Journal of Remote Sensing. 27(7):1297–1328.

Lu, D., Q. Chen, G. Wang, L. Liu, G. Li, and E. Moran. 2016. A survey of remote sensing-based aboveground biomass estimation methods in forest ecosystems. International Journal of Digital Earth. 9(1):63–105.

Lu, M.-K., T. Y. Lam, B.-H. Perng, and H.-T. Lin. 2019. Close-range photogrammetry with spherical panoramas for mapping spatial location and measuring diameters of trees under forest canopies. Can. J. For. Res. 49(8):865–874.

Lynch, T. B. 2017. Optimal plot size or point sample factor for a fixed total cost using the Fairfield Smith relation of plot size to variance. Forestry. :foresj;cpw038v1.

Lynch, T. B., J. H. Gove, T. G. Gregoire, and M. J. Ducey. In Review. An approximate point-based alternative for the estimation of variance under big BAF sampling. Forest Ecosystems.

MacLean, R. G., M. J. Ducey, and C. M. Hoover. 2014. A comparison of carbon stock estimates and projections for the northeastern United States. Forest Science. 60(2):206–213.

Marshall, D. D., K. Iles, and J. F. Bell. 2004. Using a large-angle gauge to select trees for measurement in variable plot sampling. Can. J. For. Res. 34(4):840–845.

Mette, T., K. P. Papathanassiou, I. Hajnsek, and R. Zimmermann. 2002. Forest biomass estimation using polarimetric SAR interferometry. P. 817–819 in IEEE International Geoscience and Remote Sensing Symposium, IEEE, Toronto, Ont.,

Canada. Available online at: http://ieeexplore.ieee.org/document/1025695/; last accessed May 11, 2020.

Montès, N., T. Gauquelin, W. Badri, V. Bertaudière, and E. H. Zaoui. 2000. A non-destructive method for estimating above-ground forest biomass in threatened woodlands. Forest Ecology and Management. 130(1–3):37–46.

Pearson, T. R. H., S. L. Brown, and R. A. Birdsey. 2007. Measurement guidelines for the sequestration of forest carbon. U.S. Department of Agriculture, Forest Service, Northern Research Station, Newtown Square, PA. Available online at: https://www.fs.usda.gov/treesearch/pubs/13292; last accessed January 16, 2020.

Perng, B.-H., T. Y. Lam, and M.-K. Lu. 2018. Stereoscopic imaging with spherical panoramas for measuring tree distance and diameter under forest canopies. Forestry: An International Journal of Forest Research. 91(5):662–673.

R Development Core Team. 2019. R: A Language and Environment for Statistical Computing. The R Foundation for Statistical Computing, c/o Institute for Statistics and Mathematics, 1020 Vienna, Austria. Available online at: https://www.r-project.org/.

Räsänen, A., M. Kuitunen, E. Tomppo, and A. Lensu. 2014. Coupling high-resolution satellite imagery with ALS-based canopy height model and digital elevation model in object-based boreal forest habitat type classification. ISPRS Journal of Photogrammetry and Remote Sensing. 94:169–182.

Ricoh Imaging Company, LTD. 2016. Rioch Theta S 360 video camera. Available online at: http://www.ricoh-imaging.co.jp/english/products/theta_s/; last accessed November 29, 2018.

Sales, M. H., C. M. Souza, P. C. Kyriakidis, D. A. Roberts, and E. Vidal. 2007. Improving spatial distribution estimation of forest biomass with geostatistics: A case study for Rondônia, Brazil. Ecological Modelling. 205(1–2):221–230.

Seber, G. A. F. 1982. The estimation of animal abundance and related parameters.

Smith, N. J., and K. Iles. 2012. Sector sampling—synthesis and applications. Forests. 3(1):114–126.

Smith, N. J., K. Iles, and K. Raynor. 2008. Investigation of some sector sampling statistical properties. Forest Science. 54(1):67–76.

Stewart, B., C. J. Cieszewski, and M. Zasada. 2004. Using a camera as an angle gauge in angle-count sampling. P. 375–380 in Second International Conference on Forest Measurements and Quantitative Methods and Management, Warnell School of Forestry and Natural Resources, University of Georgia, Athens, GA 30602.

Telenius, B., and T. Verwijst. 1995. The influence of allometric variation, vertical biomass distribution and sampling procedure on biomass estimates in commercial short-rotation forests. Bioresource Technology. 51(2–3):247–253.

Usoltsev, V. A., and C. W. Hoffmann. 1997. Combining harvest sample data with inventory data to estimate forest biomass. Scandinavian Journal of Forest Research. 12(3):273–279.

Wang, H. 2019. Estimating forest attributes from spherical images. MSc Forestry Thesis, University of New Brunswick, Fredericton, NB, Canada. Available online at: https://unbscholar.lib.unb.ca/islandora/object/unbscholar%3A10158.

Wang, H., J. A. Kershaw, T.-R. Yang, Y.-H. Hsu, X. Ma, and Y. Chen. 2020. An Integrated System for Estimating Forest Basal Area from Spherical Images. Mathematical and Computational Forestry and Natural-Resource Sciences. 12.

Wang, H., T.-R. Yang, J. Waldy, and J. A. Kershaw Jr. In Press. Estimating Individual Tree Heights and DBHs from Spherical Images. Mathematics and Computational Forestry and Natural Resource Sciences.

White, J. C., N. C. Coops, M. A. Wulder, M. Vastaranta, T. Hilker, and P. Tompalski. 2016. Remote Sensing Technologies for Enhancing Forest Inventories: A Review. Canadian Journal of Remote Sensing. 42(5):619–641.

Wilkes, P., S. D. Jones, L. Suarez, A. Mellor, W. Woodgate, M. Soto-Berelov, A. Haywood, and A. K. Skidmore. 2015. Mapping forest canopy height across large areas by upscaling ALS estimates with freely available satellite data. Remote sensing. 7(9):12563–12587.

Yang, T.-R., Y.-H. Hsu, J. A. Kershaw, E. McGarrigle, and Dan Kilham. 2017. Big BAF sampling in mixed species forest structures of northeastern North America: influence of count and measure BAF under cost constraints. Forestry: An International Journal of Forest Research. 90(5):649–660.

Yang, T.-R., J. A. Kershaw, A. R. Weiskittel, T. Y. Lam, and E. McGarrigle. 2019. Influence of sample selection method and estimation technique on sample size requirements for wall-to-wall estimation of volume using airborne LiDAR. Forestry: An International Journal of Forest Research. 92(3):311–323.

Zar, J. 1999. Pearson Chi-square. Biostatistical Analysis, 4th ed., Upper Saddle River, NJ. Prentice-Hall. :25–30.

Zolkos, S., S. Goetz, and R. Dubayah. 2013. A meta-analysis of terrestrial aboveground biomass estimation using lidar remote sensing. Remote Sensing of Environment. 128:289–298.

Chapter 5 Summary

5.1 Summary and Comparison of Methods Applied in this Thesis for Biomass Estimation

Biomass is an important factor in monitoring global climate change mitigation and ecosystem dynamics (Brown 1997; Mette et al. 2002; Le Toan et al. 2011). Therefore, efficient methods to estimate area-based biomass are required (Bartuska 2006; Chen et al. 2019). This thesis compared two technologies (Terrestrial Laser Scanning and Spherical 360˚ cameras) to develop regression-based models to estimate biomass, and then developed a novel subsampling protocol to estimate biomass directly from spherical images.

In the first study (Chapter 2), we compared biomass estimation via nonlinear regression models using metrics derived from Terrestrial Light Detection and Ranging scanning (TLS) to models using metrics derived from images obtained from a consumer-grade 360° spherical camera. The errors from the models (Table 2.4; Table 2.5) developed using photo metrics (photo basal area obtained at various heights above ground) were generally smaller (17% - 21%) than errors associated with models developed from LiDAR metrics (20% – 33%). While the approach was somewhat simple, neither more complicated regression models nor the use of voxelization of TLS point clouds produced any models better than the ones obtained from photo metrics.

LiDAR is commonly used for biomass estimation (Goetz et al. 2009; Gleason and Im 2011; Hayashi et al. 2015) in forest inventories. However, a combination of opportunistic sampling, sparse sample plots, and a reliance on machine learning techniques often produce errors in area-based estimates that are beyond the requirements of many monetized carbon

markets (Chen et al. 2020). Sampling to correct techniques like those developed by Hsu et al. (2020) and Chen et al. (2020) for airborne LiDAR scans and the associated enhanced forest inventories have potential to produce biomass and carbon estimates with accuracies sufficient and repeatable for monetized carbon markets; however, these techniques are not currently recognized as valid methods in existing carbon offset protocols.

Table 5. 1 Comparison of costs, accuracy and field logistics of the 3 approaches for estimating biomass used in this study.

	TLS	360 ° Spherical Camera	Photo Sector
Accuracy of estimate	Lower	Moderate	Higher
Equipment cost	Higher	Lower	Lower
	($100, 000 purchase/ $8000 monthly rental)	($400 for permanent use, plus $100 height pole set up cost)	($400 for permanent use, plus $100 height pole set up cost)
Weight of equipment	12kg	0.2kg	0.2kg
Field data collecting time	More (51min x 45 plots, 38.25h)	Less (6min x 45 plots, 13.5h)	4-5h
Labor	$3,315	$1,170	$800
Total cost	$11,855	$1,700	$800
	(average errors of 20% - 33%)	(average errors of 17% - 21%)	(average errors of 10% - 20%)
Field tree measurement	Around $10, 000	Around $10, 000	None
	($2.46 per tree, 4,100+ trees)	($2.46 per tree, 4,100+ trees)	
Post-processing time	Longer (5 hrs/plot, $6500)	Moderate (24min/plot, $520)	Shorter (10min/plot, $220)
Data analysis and processing time	more	moderate	less
Space of data storage	larger	small	smaller

In our study (Chapter 2) we used a terrestrial LiDAR scanner (TLS) to obtain high-density point clouds. To minimize tree occlusion, three TLS scans per plot were obtained (Chapter 2); we also obtained spherical images at each scanner location. Each TLS scan took about 5 minutes to set up and 12 minutes to scan; therefore, each plot in our study required 51

minutes (the 45 plots in this study required 38.25 hours of scanning). In comparison, the 360° spherical photos required about 2 minutes of set up time and about 4 minutes to acquire images at different heights above ground; therefore, each plot in our study required about 18 minutes (the 45 plots in this study required 13.5 hours of image acquisition time) (Table 5.1). Assuming field crew (3 people) costs of $650 Canadian/day and 7.5 hrs per day (Yang et al. 2017), TLS scanning costed $3,315, while spherical image acquisition costed $1,170 (Table 5.1). The TLS used in this study costs well over $100,000 Canadian and to rent it costed $8,000 Canadian for a month (approximately $53.33/work hour) (Table 5.1). On the other hand, our tripod – height pole set up costed approximately $500 Canadian and the spherical camera costed $400 for permanent use (Table 5.1). Assuming a conservative life expectancy of 250 work days, this spherical camera set up costs about $0.48/hour. Equipment usage, therefore, costed $2040 for TLS (assuming rental rates) and $6.50 for spherical camera and tripod – height pole. Total field costs for TLS were $5,355 versus $1,176.50 for spherical images (Table 5.1). Both data sources required post-field processing and model building. The three TLS scans at each sample point had to be co-registered, ground normalized, and metrics extracted. These processes could take up to 5 hours per plot on a high-end workstation. Post processing of spherical images only required photo basal area counts (Wang et al. 2020) which only take about 2 minutes per photo (2 minutes/image × 4 images/sample point × 3 sample points/plot = 24 minutes/plot) and can be carried out with much less computational requirements. Assuming that post-processing could be carried out by a single person working at a daily rate of 1/3rd the cost of a field crew day, TLS postprocessing costed another $6,500, while spherical image processing costed another $520. Discounting computational costs and model building costs, TLS

results costed a total of $11,855 with average errors of 20% - 30%, while spherical image results costed about $1,700 with average errors of 17% - 22% (Table 2.4; Table 2.5; Table 5.1).

The models built in Chapter 2 were based on permanent sample plots where all plot trees were measured for diameter and height. The costs described above do not include the costs of acquiring field data. Assuming diameter and height measurements cost about $2.46 per tree (Yang et al. 2017) with a little over 4,100 trees measured in this study, there is another $10,000 added to the costs of TLS and spherical image acquisition and processing. While less expensive field designs could have been obtained, experience with airborne LiDAR inventory models suggest that LiDAR-derived models are not very portable spatially or across LiDAR flights (Hayashi et al. 2015). While laser scanning technology and postprocessing are continuing to improve (Gollob et al. 2019), the equipment remains expensive and the measurement accuracies are still not wholly acceptable. Because of this, in Chapters 3 and 4 we sought to develop subsampling strategies based on spherical image processing that could reduce costs and maintain or improve accuracies.

BigBAF sampling is a well-established subsampling approach that efficiently selects subsamples of measure-trees (Desmarais 2002; Iles 2003; Marshall et al. 2004; Yang et al. 2017; Chen et al. 2019). BigBAF sampling uses a large BAF angle gauge to select trees for detailed measurement and the estimation of the biomass to basal area ratios (Iles 2003; Marshall et al. 2004; Yang et al. 2017; Chen et al. 2019). Larger BAFs have smaller inclusion zones, thus, trees need to be relatively closer to the sampling point. On cylindrical projections of spherical photos (as used in this study), trees close to the image acquisition point are often distorted vertically, making height measurement challenging. In Chapters 3

and 4, we explored the use of sector sampling (Iles and Smith 2006; Smith and Iles 2012) as an alternative subsampling scheme based on a randomly selected sectors radiating from the sample point.

In Chapter 3, we compared bigBAF sampling to two variants of sector we designed using simulated mapped plots derived from the NL spacing trial data and sample simulation. The first variant, which we call "SectorIn" sampling, uses a randomly oriented sector to select measure-trees as a subset in trees determined "in" using a small BAF angle guage (Figure 3.2B). The second variant uses a randomly oriented sector and selects measure-trees as all trees within the sector and a fixed, predetermined distance – regardless of whether they were "in" on the small BAF angle gauge. Our results show that the sector subsample selection methods generate as accurate of results as big BAF sampling based on similar number of measure-trees. Differences in means were less than 0.2% for BBARs with nearly equivalent errors across 3 spacing trials and 5 sample intensities(Table 3. 2). The sample intensity did not impact biomass estimation in our study, which is consistent with the results reported by Yang et al. (2017) , Chen et al. (2019) and Marshall et al. (2004).

In Chapter 4, we applied SectorDST subsampling to spherical photos (Figure 4. 2). Again, using sample simulation, we showed that measure-tree sample sizes of about 53 trees resulted in sampling errors of about 15%, which was slightly better than the sampling error across all 45 PSPs (approximately 7%, Table 4.1). However, the mean biomass per ha was underestimated because of underestimation of photo BA/ha due to tree occlusion. To address this issue, we implemented another level of double sampling to select field angle count samples to estimate the ratio of field BA to photo BA correction. As few as 10 field counts were sufficient to correct the biases and resulted in errors equivalent to those obtain

in Chapter 2 (about 19%, Figure 2.5) with the regression models, and 20 field counts resulted in errors of 10%, just slightly higher than the errors observed across the 45 field PSPs. In this application, all tree measurements (diameters and heights) were made on the photos. Field work was limited to photo acquisition and counting "in" trees on the selected field points. Costs for implementing photo sector sampling would be the same as those listed above for the regression models, with an additional $110 for angle count subsampling in the field and another $108 for photo-based tree measurement. Photo-based sector subsampling is both a statistically efficient and cost saving approach for area-based aboveground biomass estimation.

5.2 Future Developments and Work

The study sites used in this thesis came from western Newfoundland and were part of an early spacing trial in balsam fir. The forests were predominantly single-species, single cohort stands, and, all but control plots, had uniform spacing and diameter distributions. Given that all plots were the same age, heights also did not vary much. This probably greatly contributed to the overall excellent performance of our photo-based methods. Even though Wang et al. (2020) showed that stand structure had little influence on overall photo BA estimation, it is still expected that as stand complexity increases, implementation of photo-based estimation of BA and tree measurements might become more difficult. Wang et al. (In Press) did find that there was increased variation in tree size distributions based on photo measurements from these same plots compared to photo-measured trees in an open urban setting. Finally, we only tested field to photo BA correction using simple

random sampling. Yang et al. (2019), Chen et al. (2020), and Hsu et al. (2020) showed that variable probability selection with ratio estimation is more efficient than random sampling. Future work on this topic would include:

1) Testing the process in more complicated forest stand structures;
2) Implementing a forest-wide operational scale demonstration of the technique;
3) Test techniques in forest structures with taller trees;
4) Compare variable probability selection of field points for photo BA correction to random and systematic selection;
5) Develop in-field image processing capabilities and biomass estimation to implement and test one-field-visit 3P sampling;
6) Test the newer, higher resolution spherical cameras;

and

7) Compare the photo-based measurements derived in this study to measurements derived from photo point clouds and structure from motion.

These further studies would confirm the general applicability of the methods developed in this study. These methods could easily be applied to estimate almost any area-based tree quantity. While laser scanning has great potential, its costs, exchange of office time for field time, and limited accuracies makes it a technology that has limited operational applications. The methods developed here represent low cost and accurate alternatives.

References

Bartuska, A. 2006. Why biomass is important: The role of the USDA forest service in managing and using biomass for energy and other uses. Research & Development, USDA Forest Service. 1–16 p.

Brown, S. 1997. Estimating biomass and biomass change of tropical forests: a primer. Food & Agriculture Org.

Chen, Y., J. A. Kershaw, Y.-H. Hsu, and T.-R. Yang. 2020. Carbon estimation using sampling to correct LiDAR-assisted enhanced forest inventory estimates. The Forestry Chronicle. 96(01):9–19.

Chen, Y., T.-R. Yang, Y.-H. Hsu, J. A. Kershaw, and D. Prest. 2019. Application of big BAF sampling for estimating carbon on small woodlots. For. Ecosyst. 6(1):13.

Dai, X. In Preparation. Novel Methods for Estimating Above Ground Biomass.

Desmarais, K. M. 2002. Using BigBAF sampling in a New England mixedwood forest. John Bell & Associates Inventory & Cruising Newsletter. 58.

Gleason, C. J., and J. Im. 2011. A review of remote sensing of forest biomass and biofuel: options for small-area applications. GIScience & Remote Sensing. 48(2):141–170.

Goetz, S. J., A. Baccini, N. T. Laporte, T. Johns, W. Walker, J. Kellndorfer, R. A. Houghton, and M. Sun. 2009. Mapping and monitoring carbon stocks with satellite observations: a comparison of methods. Carbon balance and management. 4(1):2.

Gollob, C., T. Ritter, C. Wassermann, and A. Nothdurft. 2019. Influence of Scanner Position and Plot Size on the Accuracy of Tree Detection and Diameter

Estimation Using Terrestrial Laser Scanning on Forest Inventory Plots. Remote Sensing. 11(13):1602.

Hayashi, R., J. A. Kershaw, and A. Weiskittel. 2015. Evaluation of alternative methods for using LiDAR to predict aboveground biomass in mixed species and structurally complex forests in northeastern North America. MCFNS. 7(2):49–65.

Hsu, Y.-H., Y. Chen, T.-R. Yang, J. A. Kershaw, and M. J. Ducey. 2020. Sample strategies for bias correction of regional LiDAR-assisted forest inventory Estimates on small woodlots. Annals of Forest Science. 77(3):1–12.

Iles, K. 2003. A sampler of inventory topics. Kim Isles & Associates Ltd., Nanimo. British Columbia, Canada.

Iles, K., and N. J. Smith. 2006. A new type of sample plot that is particularly useful for sampling small clusters of objects. Forest Science. 52(2):148–154.

Le Toan, T., S. Quegan, M. W. J. Davidson, H. Balzter, P. Paillou, K. Papathanassiou, S. Plummer, et al. 2011. The BIOMASS mission: Mapping global forest biomass to better understand the terrestrial carbon cycle. Remote Sensing of Environment. 115(11):2850–2860.

Marshall, D. D., K. Iles, and J. F. Bell. 2004. Using a large-angle gauge to select trees for measurement in variable plot sampling. Can. J. For. Res. 34(4):840–845.

Mette, T., K. P. Papathanassiou, I. Hajnsek, and R. Zimmermann. 2002. Forest biomass estimation using polarimetric SAR interferometry. P. 817–819 in IEEE International Geoscience and Remote Sensing Symposium, IEEE, Toronto, Ont., Canada. Available online at: http://ieeexplore.ieee.org/document/1025695/; last accessed May 11, 2020.

Smith, N. J., and K. Iles. 2012. Sector sampling—synthesis and applications. Forests. 3(1):114–126.

Wang, H., J. A. Kershaw, T.-R. Yang, Y.-H. Hsu, X. Ma, and Y. Chen. 2020. An Integrated System for Estimating Forest Basal Area from Spherical Images. Mathematical and Computational Forestry and Natural-Resource Sciences. 12.

Wang, H., T.-R. Yang, J. Waldy, and J. A. Kershaw Jr. In Press. Estimating Individual Tree Heights and DBHs from Spherical Images. Mathematics and Computational Forestry and Natural Resource Sciences.

Yang, T.-R., Y.-H. Hsu, J. A. Kershaw, E. McGarrigle, and Dan Kilham. 2017. Big BAF sampling in mixed species forest structures of northeastern North America: influence of count and measure BAF under cost constraints. Forestry: An International Journal of Forest Research. 90(5):649–660.

Yang, T.-R., J. A. Kershaw, A. R. Weiskittel, T. Y. Lam, and E. McGarrigle. 2019. Influence of sample selection method and estimation technique on sample size requirements for wall-to-wall estimation of volume using airborne LiDAR. Forestry: An International Journal of Forest Research. 92(3):311–323.

Curriculum Vitae

Candidate's full name: Xiao Dai

Universities attended (with dates and degrees obtained): Nanjing Forestry University (2014-2018, bachelor)

Publications: 1. "Sector Subsampling for Basal Area Ratio Estimation: An Alternative to Big BAF Sampling" (Canadian Journal of Forest Research, In Review)

2. "Use of Sector Sampling of 360 Spherical Images for Biomass Estimation" (Forestry, In Review)

Conference Presentations:

1. 2019 Graduate Research Conference, Comparisons of Biomass Estimation Approaches from Spherical Images and Terrestrial LiDAR. Wu Centre Lobby, University of New Brunswick (March 21st, 2019)
2. Western Mensurationists 2019 Meeting, Comparisons of Biomass Estimation Approaches Using Spherical Images and Terrestrial LiDAR. Kamloops-BC, Canada (Jun 23rd, 2019)
3. 2019 Graduate Seminar, Comparison of Biomass Estimations Using Spherical Images versus Terrestrial LiDAR Scans in eastern North America. Room 203 – Forestry and Geology, University of New Brunswick (December 9th, 2019)
4. 2020 Graduate Seminar Poster Presentation, Sector subsampling as an alternative to bigBAF sampling (Dec 8th, 2020)
5. Western Mensurationists 2020 Virtual Annual Meeting, Use of Sector Sampling as an Alternative Subsampling Design for Estimating Biomass from Spherical Images. Online Host: University of Idaho (June 14th-16th, 2020)